

Simulating the gamma-ray emission from galaxy clusters: a universal cosmic ray spectrum and spatial distribution

Anders Pinzke^{1,2*} and Christoph Pfrommer^{3*}

¹*Department of Physics, Stockholm University, AlbaNova University Center, SE - 106 91 Stockholm, Sweden*

²*The Oskar Klein Centre for Cosmoparticle Physics, Department of Physics, Stockholm University, AlbaNova University Center, SE - 106 91 Stockholm, Sweden*

³*Canadian Institute for Theoretical Astrophysics, University of Toronto, 60 St. George Street, Toronto, Ontario, M5S 3H8, Canada*

2 November 2018

ABSTRACT

Entering a new era of high-energy γ -ray experiments, there is an exciting quest for the first detection of γ -ray emission from clusters of galaxies. To complement these observational efforts, we use high-resolution simulations of a broad sample of galaxy clusters, and follow self-consistent cosmic ray (CR) physics using an improved spectral description. We study CR proton spectra as well as the different contributions of the pion decay and inverse Compton emission to the total flux and present spectral index maps. We find a universal spectrum of the CR component in clusters with surprisingly little scatter across our cluster sample. When CR diffusion is neglected, the spatial CR distribution also shows approximate universality; it depends however on the cluster mass. This enables us to derive a semi-analytic model for both, the distribution of CRs as well as the pion-decay γ -ray emission and the secondary radio emission that results from hadronic CR interactions with ambient gas protons. In addition, we provide an analytic framework for the inverse Compton emission that is produced by shock-accelerated CR electrons and valid in the full γ -ray energy range. Combining the complete sample of the brightest X-ray clusters observed by ROSAT with our γ -ray scaling relations, we identify the brightest clusters for the γ -ray space telescope Fermi and current imaging air Čerenkov telescopes (MAGIC, HESS, VERITAS). We reproduce the result in Pfrommer (2008), but provide somewhat more conservative predictions for the fluxes in the energy regimes of Fermi and imaging air Čerenkov telescopes when accounting for the bias of ‘artificial galaxies’ in cosmological simulations. We find that it will be challenging to detect cluster γ -ray emission with Fermi after the second year but this mission has the potential of constraining interesting values of the shock acceleration efficiency after several years of surveying. Comparing the predicted emission from our semi-analytic model to that obtained by means of our scaling relations, we find that the γ -ray scaling relations underpredict, by up to an order of magnitude, the flux from cool core clusters.

Key words: magnetic fields, cosmic rays, radiation mechanisms: non-thermal, elementary particles, galaxies: cluster: general, Galaxy: fundamental parameters

1 INTRODUCTION

1.1 General background

In the cold dark matter (CDM) universe, large scale structure grows hierarchically through merging and accretion of smaller systems into larger ones, and clusters are the latest and most massive objects that had time to virialise. This process leads to collisionless shocks propagating through the intra-cluster medium (ICM), accelerating both protons and electrons to highly relativistic energies (Drury 1983; Blandford & Eichler 1987; Sarazin 1999). High resolution X-ray observations by the *Chandra* and *XMM-Newton* satellites

confirmed this picture, with most clusters displaying evidence for significant substructures, shocks, and contact discontinuities (e.g., Rosati et al. 2002; Voit 2005; Markevitch & Vikhlinin 2007). In addition, observations of radio halos and radio relics demonstrate the presence of synchrotron emitting electrons with energies reaching ~ 10 GeV in more than 50 clusters (Feretti 2003; Ferrari et al. 2008), although their precise origin in radio halos is still unclear. Similar populations of electrons may radiate γ -rays efficiently via inverse Compton (IC) upscattering of the cosmic microwave background photons giving rise to a fraction of the diffuse γ -ray background observed by EGRET (Loeb & Waxman 2000; Totani & Kitayama 2000; Miniati 2002, 2003; Inoue & Nagashima 2005). Although there is no clear observational evidence yet for a relativistic proton population in clusters of galaxies, these objects

* e-mail: apinzke@fysik.su.se (AP); pfrommer@cita.utoronto.ca (CP)

are expected to contain significant populations of relativistic protons originating from different sources, such as structure formation shocks, radio galaxies, and supernovae driven galactic winds. The ICM gas should provide ample target matter for inelastic collisions of relativistic protons leading to γ -rays (Völk et al. 1996; Enßlin et al. 1997; Miniati 2003; Pfrommer & Enßlin 2003, 2004; Pfrommer et al. 2008; Pfrommer 2008; Kushnir & Waxman 2009) as well as secondary electron injection (Dennison 1980; Vestrand 1982; Blasi & Colafrancesco 1999; Dolag & Enßlin 2000; Miniati et al. 2001b; Pfrommer & Enßlin 2004; Pfrommer et al. 2008; Kushnir & Waxman 2009; Kushnir et al. 2009). These hadronic collision processes should illuminate the presence of these elusive particles through pion production and successive decay into the following channels:

$$\begin{aligned}\pi^\pm &\rightarrow \mu^\pm + \nu_\mu/\bar{\nu}_\mu \rightarrow e^\pm + \nu_e/\bar{\nu}_e + \nu_\mu + \bar{\nu}_\mu \\ \pi^0 &\rightarrow 2\gamma\end{aligned}$$

This reaction can only unveil those cosmic ray protons (CRs) which have a total energy that exceeds the kinematic threshold of the reaction of $E_{\text{thr}} = 1.22$ GeV. The magnetic fields play another crucial role by confining non-thermal protons within the cluster volume for longer than a Hubble time, i.e. any protons injected into the ICM accumulates throughout the cluster's history (Völk et al. 1996; Enßlin et al. 1997; Berezhinsky et al. 1997). Hence, CRs can diffuse away from the production site, establishing a smooth distribution throughout the entire ICM which serves as efficient energy reservoir for these non-gravitational processes (Blasi & Colafrancesco 1999; Dolag & Enßlin 2000; Miniati et al. 2001a).

There is only little known theoretically about the spectral shape of the CR population in the ICM. It is an interesting question whether it correlates with injection processes or is significantly modified by transport and re-acceleration processes of CRs through interactions with magneto-hydrodynamic (MHD) waves. The most important processes shaping the CR spectrum as a function of cluster radius are (1) acceleration by structure formation shock waves (Quilis et al. 1998; Miniati et al. 2000; Pfrommer et al. 2006), MHD turbulence, supernova driven galactic winds (Acciari et al. 2009), or active galactic nuclei (AGN), (2) adiabatic and non-adiabatic transport processes, in particular anisotropic diffusion, and (3) loss processes such as CR thermalization by Coulomb interactions with ambient electrons and catastrophic losses by hadronic interactions. The spectral distribution of CRs that are accelerated at structure formation shocks should be largely described by a power-law with a spectral index of the one-dimensional distribution given by

$$\alpha_{\text{inj}} = \frac{r_c + 2}{r_c - 1}, \quad (1)$$

where r_c is the shock compression factor. Strong (high Mach number) shocks that inject a hard CR population occur either at high redshift during the formation of the proto-clusters or today at the boundary where matter collapses from voids onto filaments or super-cluster regions. In contrast, merger shocks show weak to intermediate strength with typical Mach numbers in the range of $\mathcal{M} \approx 2 \dots 4$ (Ryu et al. 2003; Pfrommer et al. 2006; Skillman et al. 2008). AGNs or supernova remnants are expected to inject CRs with rather flat spectra, $\alpha_{\text{inj}} \approx 2.2 - 2.4$ (Völk et al. 1996; Schlickeiser 2002; Enßlin 2003), but it is not clear whether they are able to build up a homogeneous population of significant strength.

The CRs offer a unique window to probe the process of struc-

ture formation due to its long cooling times. While the thermal plasma quickly dissipates and erases the information about its past history, the CR distribution keeps the fossil record of violent structure formation which manifests itself through the spectrum that is shaped by acceleration and transport processes. The cluster γ -ray emission is crucial in this respect as it potentially provides the unique and unambiguous evidence of a CR population in clusters through observing the pion bump in the γ -ray spectrum. This knowledge enables determining the CR pressure and whether secondary electrons could contribute to the radio halo emission. In the γ -ray regime, there are two main observables, the morphological appearance of the emission and the spectrum as a function of position relative to the cluster center. The morphology of the pion induced γ -ray emission should follow that seen in thermal X-rays albeit with a slightly larger extent (Pfrommer et al. 2008). The primary electrons that are accelerated directly at the structure formation shocks should be visible as an irregular shaped IC morphology, most pronounced in the cluster periphery (Miniati 2003; Pfrommer et al. 2008).

1.2 The γ -ray spectrum of a galaxy cluster

How do the spectral electron and proton distributions map onto the γ -ray spectrum? We show the CR spectrum within the virial radius of a simulated Coma-like galaxy cluster in the upper part of Fig. 1. It is shaped by diffusive shock acceleration at structure formation shocks, adiabatic transport and the relevant CR loss processes¹. Three distinct features are visible in the spectrum: a cutoff close to the proton rest mass at $m_p c^2 \approx 1$ GeV, a concave shape for proton energies above $m_p c^2$ and a steepening due to diffusive losses at energies $E_p \gtrsim 10^{16} \text{ eV} \times [\kappa_0 / (10^{29} \text{ cm}^2 \text{ s}^{-1})]^{-3}$, where κ_0 is the value of the diffusion coefficient at 1 GeV. The dotted lines represents different values of the diffusion coefficient which is varied by a factor two from its fiducial value. The low energy cutoff is due to a balance of Coulomb and hadronic losses at energies around a GeV (Jubelgas et al. 2008). As shown in the present paper and in an upcoming work by Pinzke & Pfrommer (in prep.), the concave curvature is a unique shape² that is caused by the cosmic Mach number distribution in combination with adiabatic transport processes. These features are mapped onto the pion decay γ -ray emission spectra as a consequence of hadronic CR interactions.

This can be seen in the lower part of Fig. 1, where the arrows indicate the spectral mapping from the CR spectrum to the photon spectrum. In a hadronic interaction, CRs produce pions that decay into photons with an energy that is on average smaller by a factor eight compare to the original CR energy (see Section 2.2). At CR energies that are larger than the hadronic reaction threshold, the CR power-law behavior is linearly mapped onto the *pion decay induced γ -ray spectrum* (solid blue). This emission component clearly dominates the total photon spectrum and therefore shapes the total emission characteristics in the central parts of the cluster,

¹ The physics will be thoroughly developed in this work but we will review the main characteristics here for introduction.

² A CR distribution with uniform spectral index was also hinted at by Miniati et al. (2001a) and Miniati (2002), where the dominating strong shocks caused a constant spectral index of about $\alpha \approx 2$. Their underlying Mach number distribution, however, is in conflict with that obtained by independent other works (Ryu et al. 2003; Pfrommer et al. 2007; Skillman et al. 2008) and the spectral shape that we find (see Section 8.1 for more details).

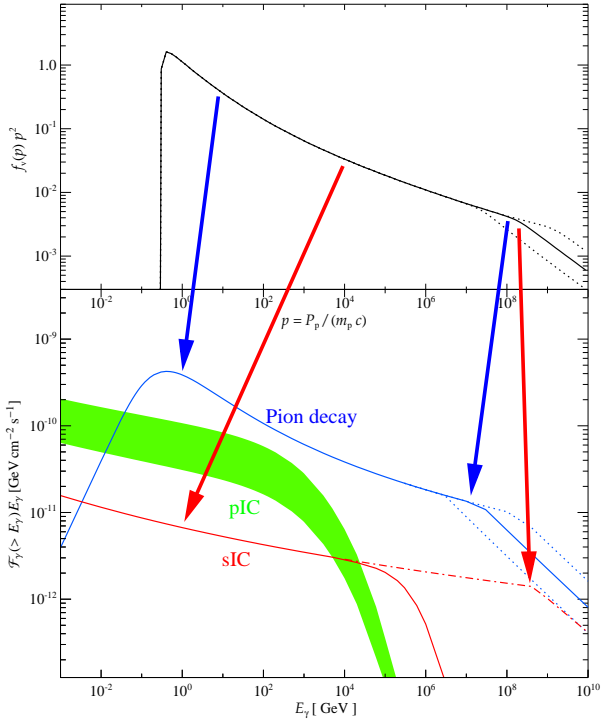


Figure 1. *Upper Panel:* CR spectral distribution within the virial radius of a Coma-like cluster. It shows three distinct features: a cutoff around GeV energies, a concave shape, and a steepening at high energies due to diffusive losses. *Lower Panel:* we show the intrinsic γ -ray number flux weighted by the photon energy that does not take into account photon propagation effects. The arrows indicate the spectral mapping from the CR spectrum to the photon spectrum. The pion decay flux is denoted in blue color, the secondary inverse Compton (sIC) in red, and the primary inverse Compton (pIC) emission in green. Due to the large uncertainty in the diffusion coefficient κ , we demonstrate how varying κ by a factor of two changes the corresponding γ -ray spectrum at high energies (dotted lines). The green band shows how the pIC emission changes if we vary the maximum electron injection efficiency from 0.05 (top) to 0.01 (bottom).

where the densities are high. Note that this spectrum is an intrinsic spectrum emitted at the cluster position and converted to a flux while assuming a distance of 100 Mpc without taking into account photon propagation effects. Depending on the cluster redshift, the finite mean free path of high-energy γ -rays to e^+e^- -pair production on infra red (IR) and optical photons limits the observable part of the spectrum to energies $E_\gamma \lesssim 10$ TeV for clusters with redshifts $z \sim 0.03$, and smaller energies for higher redshift objects (Franceschini et al. 2008).

Secondary CR electrons and positrons up-scatter cosmic microwave background (CMB) photons through the IC process into the γ -ray regime, the so-called *secondary inverse Compton emission* (sIC). This emission component originates from the flat high-energy part of the CR spectrum and produces a rather flat sIC spectrum up to the Klein-Nishina (KN) regime. At large electron energies, we enter the KN regime of IC scattering where the electron recoil effect has to be taken into account. It implies less efficient energy transfer in such an elastic scattering event compared to the Thomson regime and leads to a dramatic steepening of the sIC spectrum at γ -ray energies around 100 TeV (solid red line).

The dash-dotted red line shows the hypothetical sIC spectrum in the absence of the KN effect (which is never realized in Nature). However, it clearly shows that the diffusive CR break is not observable in the sIC component for large clusters (while it can move to energies below the KN break for small enough clusters, causing a faster steepening there). The spectrum shown in green color represents the energy weighted photon spectrum resulting from the IC process due to electrons accelerated at structure formation and merger shocks, the *primary inverse Compton emission* (pIC). The exponential cutoff is due to synchrotron and IC losses which lead to a maximum energy of the shock-accelerated electrons. The green pIC band shows the effect of the maximum electron injection efficiency, where we use an optimistic value of $\zeta_{e,\max} = 0.05$ (see e.g. Keshet et al. 2003) in the top and a value of $\zeta_{e,\max} = 0.01$ at the bottom. This more realistic value is suggested to be the theoretically allowed upper limit for the injection efficiency that is consistent with the non-thermal radiation of young supernova remnants (Zirakashvili & Aharonian 2010).

This work studies the spectral and morphological emission characteristics of the different CR populations in the γ -ray regime. We concentrate on observationally motivated high-energy γ -ray bands. (1) The energy regime accessible to the *Fermi γ -ray space telescope* with a particular focus on $E_\gamma = 100$ MeV and (2) the energy regime accessible to imaging air Čerenkov telescopes (IACTs) assuming a lower energy limit of 100 GeV. In Section 2 we describe the setup of our simulations, explain our methodology and relevant radiative processes considered in this work. In Section 3, we study emission profiles and maps, as well as spectral index maps. We then present the CR spectrum and spatial distribution and show its universality across our simulated cluster sample in Section 4. This allows us to derive a semi-analytic framework for the cluster γ -ray emission in Section 5 which we demonstrate on the Perseus and Coma galaxy clusters. Furthermore, we study the mass-to-luminosity scaling relations (Section 6) and predict the γ -ray flux from a large sample of galaxy clusters for the GeV and TeV energy regimes in Section 7. We compare our work to previous papers in this field and point out limitations of our approach in Section 8. We conclude our findings in Section 9. Throughout this work we use a Hubble constant of $H_0 = 70 \text{ km s}^{-1} \text{ Mpc}^{-1}$, which is a compromise between the value found by the Hubble key project ($H_0 = 72$, Freedman et al. 2001) and from that one inferred from baryonic acoustic oscillation measurements ($H_0 = 68$, Percival et al. 2009).

2 SETUP AND FORMALISM

We follow the CR proton pressure dynamically in our simulations while taking into account all relevant CR injection and loss terms in the ICM, except for a possible proton production from AGN and supernova remnants. In contrast, we model the CR electron population in a post-processing step because it does not modify the hydrodynamics owing to its negligible pressure contribution. We use a novel CR formalism that allows us to study the spectral properties of the CR population more accurately.

2.1 Adopted cosmology and cluster sample

The simulations were performed in a Λ CDM universe using the cosmological parameters: $\Omega_m = \Omega_{\text{DM}} + \Omega_b = 0.3$, $\Omega_b = 0.039$, $\Omega_\Lambda = 0.7$, $h = 0.7$, $n_s = 1$, and $\sigma_8 = 0.9$. Here, Ω_m denotes the total matter density in units of the critical density for

geometrical closure today, $\rho_{\text{crit}} = 3H_0^2/(8\pi G)$. Ω_b , Ω_{DM} and Ω_Λ denote the densities of baryons, dark matter, and the cosmological constant at the present day. The Hubble constant at the present day is parametrized as $H_0 = 100 h \text{ km s}^{-1} \text{ Mpc}^{-1}$, while n_s denotes the spectral index of the primordial power-spectrum, and σ_8 is the *rms* linear mass fluctuation within a sphere of radius $8 h^{-1} \text{ Mpc}$ extrapolated to $z = 0$.

Our simulations were carried out with an updated and extended version of the distributed-memory parallel TreeSPH code GADGET-2 (Springel 2005; Springel et al. 2001). Gravitational forces were computed using a combination of particle-mesh and tree algorithms. Hydrodynamic forces are computed with a variant of the smoothed particle hydrodynamics (SPH) algorithm that conserves energy and entropy where appropriate, i.e. outside of shocked regions (Springel & Hernquist 2002). Our simulations follow the radiative cooling of the gas, star formation, supernova feedback, and a photo-ionizing background (details can be found in Pfrommer et al. 2007).

The clusters have originally been selected from a low-resolution dark-matter-only simulation (Yoshida et al. 2001). Using the ‘zoomed initial conditions’ technique (Katz & White 1993), the clusters have been re-simulated with higher mass and force resolution by adding short-wavelength modes within the Lagrangian regions in the initial conditions that will evolve later-on into the structures of interest. We analyzed the clusters with a halo-finder based on spherical overdensity followed by a merger tree analysis in order to get the mass accretion history of the main progenitor. The spherical overdensity definition of the virial mass of the cluster is given by the material lying within a sphere centered on a local density maximum, whose radial extend R_Δ is defined by the enclosed threshold density condition $M(< R_\Delta)/(4\pi R_\Delta^3/3) = \rho_{\text{thres}}$. We chose the threshold density $\rho_{\text{thres}}(z) = \Delta \rho_{\text{crit}}(z)$ to be a constant multiple $\Delta = 200$ of the critical density of the universe $\rho_{\text{crit}}(z) = 3H(z)^2/(8\pi G)$. In the remaining of the paper, we use the terminology R_{vir} instead of R_{200} . Our sample of simulated galaxy clusters consists of 14 clusters that span a mass range from $8 \times 10^{13} M_\odot$ to $3 \times 10^{15} M_\odot$ where the dynamical stages range from relaxed cool core clusters to violent merging clusters (cf. Table 1). Each individual cluster is resolved by 8×10^4 to 4×10^6 particles, depending on its final mass. The SPH densities were computed from the closest 48 neighbors, with a minimum smoothing length (h_{smi}) set to half the softening length. The Plummer equivalent softening length is 7 kpc in physical units after $z = 5$, implying a minimum gas resolution of approximately $1.1 \times 10^{10} M_\odot$ (see also Pfrommer et al. 2007).

2.2 Modeling of CR protons and induced radiative processes

Our simulations follow cosmic ray physics in a self-consistent way (Pfrommer et al. 2006; Enßlin et al. 2007; Jubelgas et al. 2008). We model the adiabatic CR transport process such as compression and rarefaction, and a number of physical source and sink terms which modify the cosmic ray pressure of each CR population separately. The most important source considered³ for acceleration is diffusive shock acceleration at cosmological structure formation shocks, while the primary sinks are thermalization by Coulomb interactions, and catastrophic losses by hadronization. Collisionless structure formation shocks are able to accelerate ions and elec-

³ For simplicity, in this paper we do not take into account CRs injected into the inter-stellar medium from supernova remnants (see Aleksić et al. (2010) for a discussion of this topic).

Table 1. Cluster sample.

Cluster	sim.'s	dyn. state ⁽¹⁾	$M_{\text{vir}}^{(2)}$ [M_\odot]	$R_{\text{vir}}^{(2)}$ [Mpc]	$kT_{\text{vir}}^{(3)}$ [keV]
1	g8a	CC	2.6×10^{15}	2.9	13.1
2	g1a	CC	1.9×10^{15}	2.5	10.6
3	g72a	PostM	1.6×10^{15}	2.4	9.4
4	g51	CC	1.5×10^{15}	2.4	9.4
5	g1b	M	5.2×10^{14}	1.7	4.7
6	g72b	M	2.2×10^{14}	1.2	2.4
7	g1c	M	2.0×10^{14}	1.2	2.3
8	g8b	M	1.5×10^{14}	1.1	1.9
9	g1d	M	1.3×10^{14}	1.0	1.7
10	g676	CC	1.3×10^{14}	1.0	1.7
11	g914	CC	1.2×10^{14}	1.0	1.6
12	g1e	M	9.1×10^{13}	0.93	1.3
13	g8c	M	8.5×10^{13}	0.91	1.3
14	g8d	PreM	7.8×10^{13}	0.88	1.2

Notes:

(1) The dynamical state has been classified through a combined criterion invoking a merger tree study and the visual inspection of the X-ray brightness maps. The labels for the clusters are M–merger, PostM–post merger (slightly elongated X-ray contours, weak cool core (CC) region developing), PreM–pre-merger (sub-cluster already within the virial radius), CC–cool core cluster with extended cooling region (smooth X-ray profile). (2) The virial mass and radius are related by $M_\Delta(z) = \frac{4}{3}\pi \Delta \rho_{\text{crit}}(z) R_\Delta^3$, where $\Delta = 200$ denotes a multiple of the critical overdensity $\rho_{\text{crit}}(z) = 3H(z)^2/(8\pi G)$. (3) The virial temperature is defined by $kT_{\text{vir}} = GM_{\text{vir}} \mu m_p / (2R_{\text{vir}})$, where μ denotes the mean molecular weight.

trons in the high-energy tail of their Maxwellian distribution functions through diffusive shock acceleration (for reviews see Drury 1983; Blandford & Eichler 1987; Malkov & O’C Drury 2001). In the test particle picture, this process injects a CR distribution with a power-law in momentum and a slope that depends on the instantaneous sonic Mach number of the shock. The overall normalization of the injected CR distribution depends on the adopted sub-resolution model of diffusive shock acceleration (e.g., Enßlin et al. 2007); in particular it depends on the maximum acceleration efficiency $\zeta_{\text{max,p}} = \varepsilon_{\text{CR,max}}/\varepsilon_{\text{diss}}$ which is the maximum ratio of CR energy density that can be injected relative to the total dissipated energy density at the shock. We assume that in the saturated regime of shock acceleration, 50 percent of the dissipated energy at strong shocks is injected into cosmic ray protons. While there are indications from supernova remnant observations of one rim region (Helder et al. 2009) as well as theoretical studies (Kang & Jones 2005) that support such high efficiencies, to date it is not clear whether these efficiencies apply in an average sense to strong collisionless shocks or whether they are realized for structure formation shocks at higher redshifts. This high efficiency rapidly decreases for weaker shocks (decreasing Mach number) and eventually smoothly approaches zero for sonic waves (Enßlin et al. 2007). Our paper aims at providing a quantitative prediction of the γ -ray flux and hence the associated CR flux that we expect in a cluster depending on our adopted acceleration model. Non-detection of our predicted emission will limit the CR acceleration efficiency and help in answering these profound plasma astrophysics questions about particle acceleration efficiencies.

We significantly revised the CR methodology and allow for multiple non-thermal cosmic ray populations of every fluid element (Pinzke & Pfrommer, in prep.). Each CR population $f_i(p, \mathbf{R})$ is a

power-law in particle momentum⁴,

$$f_i(p, \mathbf{R}) = C_i(\mathbf{R}) p^{-\alpha_i} \theta(p - q_i), \quad (2)$$

characterized by a fixed slope α_i , a low-momentum cutoff q_i , and an amplitude $C_i(\mathbf{R})$ that is a function of the position of each SPH particle through the variable \mathbf{R} . For this paper we have chosen five CR populations with the spectral index distribution $\alpha = (2.1, 2.3, 2.5, 2.7, 2.9)$ for each fluid element (a convergence study on the number of CR populations is presented in the appendix A2). This approach allows a more accurate spectral description⁵ as the superposition of power-law spectra enables a concave curvature of the composite spectrum in logarithmic representation. Physically, more complicated spectral features such as bumps can arise from the finite lifetime and length scale of the process of diffusive shock acceleration or incomplete confinement of CRs to the acceleration region. These effects imprint an upper cutoff to the CR population locally that might vary spatially and which translates into a convex curvature in projection. Additionally, interactions of pre-existing CRs with MHD waves can yield to more complex spectral features. Future work will be dedicated to study these topics.

In addition to the spectral features mentioned above, we model in the post-processing the effect of high-energy CR protons that are no longer confined to a galaxy cluster as these are able to diffuse into the ambient warm-hot intergalactic medium (WHIM). In this paper we define WHIM to be the region within $R_{\text{vir}} < R < 3 R_{\text{vir}}$, which is a subset of the entire WHIM (Davé et al. 2001). Assuming particle scattering off magnetic irregularities with the Kolmogorov spectrum, we obtain the characteristic scaling of the diffusion coefficient $\kappa \approx \kappa_0 (E/E_0)^{1/3}$, where we normalize κ at $E_0 = 1$ GeV. One can estimate the characteristic proton energy $E_{p, \text{break}}$ at which the spectrum steepens (Völk et al. 1996; Berezhinsky et al. 1997),

$$\begin{aligned} E_{p, \text{break}} &\approx \frac{E_0 R^6}{(6 \kappa_0 \tau)^3} \\ &\approx 10^8 \text{ GeV} \left(\frac{R}{3 \text{ Mpc}} \right)^6 \left(\frac{\kappa_0}{10^{29} \text{ cm}^2 \text{ s}^{-1}} \right)^{-3} \left(\frac{\tau}{T_{\text{Hubble}}} \right)^{-3}. \end{aligned} \quad (3)$$

For the remainder, we adopt a value of the diffusivity that is scaled to $R = 2 R_{\text{vir}}$ for each cluster, as this volume is expected to fall within the virialised part of the cluster past the accretion shock region (Pfrommer et al. 2007; Molnar et al. 2009) and traps CRs in a cluster for time scales longer than a Hubble time. This choice also has the property that the diffusion break is at energies $E_p > 100$ GeV; hence it does not interfere with the pion decay as well as secondary IC emission in the energy regime accessible to IACTs as we will show in the following. The momentum of a photon that results from pion decay is given by

$$P_\gamma \approx \frac{K_p P_p}{2 \xi} \approx \frac{P_p}{8}. \quad (4)$$

This approximate relation is derived using the inelasticity $K_p \approx 1/2$ and multiplicity $\xi \approx 2$ for the $p + p \rightarrow \pi^0$ channel together with the two photons in the final state. Secondary electrons that are injected in hadronic CR interactions Compton up-scatter CMB photons. A break in the parent CR spectrum would imprint itself in

the sIC spectrum if there are no other effects that modify the spectrum at lower energies. Compared to the pion decay emission, this break manifests at slightly higher energies (for parameters adopted in Fig. 1). The momentum of the electrons P_e depends on the proton momentum P_p through the relation given by hadronic physics

$$P_e \approx \frac{K_p P_p}{4 \xi} \approx \frac{P_p}{16}. \quad (5)$$

Here we used the $p + p \rightarrow \pi^\pm$ channel together with the four particles in the final state of the charged pion decay ($e^\pm, \nu_e/\bar{\nu}_e, \nu_\mu, \bar{\nu}_\mu$). Combining the classical inverse Compton formulae from CR electrons with energies $E_e > 1$ GeV

$$E_{\text{IC}} = \frac{4}{3} E_{\text{CMB}} \left(\frac{E_e}{m_e c^2} \right)^2, \quad (6)$$

with the energy relation in equation (5) we obtain a break in the sIC spectrum. This steepening of the CR spectrum take place at high photon energies $E_{\text{sIC, break}} \approx 10^{17}$ eV where we choose CMB photons with the energy $E_{\text{CMB}} = h\nu_{\text{CMB}} \approx 0.66$ meV as source for the inverse Compton emission using Wien's displacement law. It turns out that these energies are deeply in the Klein-Nishina regime. This means that in the rest frame of the energetic electron, the Lorentz boosted photon energy is comparable to or larger than the electron rest mass, $E_{\text{IC}} = \gamma_e h\nu_{\text{init}} \sim m_e c^2$, so that the scattering event becomes elastic. This implies a less efficient energy transfer to the photon and manifests itself in a break in the resulting IC spectrum. While the number flux scales as $\mathcal{F} \sim E_{\text{IC}}^{-(\alpha_e-1)/2}$ in the Thomson-limit for $E_{\text{IC}} \ll 30$ TeV, it steepens significantly to $\mathcal{F} \sim E_{\text{IC}}^{-\alpha_e} \log(E_{\text{IC}})$ in the extreme KN-limit for $E_{\text{IC}} \gg 30$ TeV, where α_e is the spectral index of the (cooled) CR electron distribution (Blumenthal & Gould 1970).

2.3 Magnetic fields

High energy CR electrons with $\gamma_e > 200$ loose their energy by means of IC scattering off CMB photons as well as through interactions with cluster magnetic fields which results in synchrotron emission. The relative importance of these two emission mechanisms depends on the *rms* magnetic field strength, B , relative to the equivalent field strength of the CMB, $B_{\text{CMB}} = 3.24 (1+z)^2 \mu\text{G}$, where z denotes the redshift. In the peripheral cluster regions, where $B \ll B_{\text{CMB}}$, the CR electrons loose virtually all their energy by means of IC emission. In the central cluster regions, in particular in the dense centers of cool cores, the magnetic energy density is probably comparable or even larger than the energy density of the CMB (Vogt & Enßlin 2005), $\epsilon_{\text{ph}} = B_{\text{CMB}}^2/(8\pi)$. Hence in these regions, the radio synchrotron emission carries away a fraction of the CR electrons' energy losses; an effect that reduces the level of IC emission. We model the strength and morphology of the magnetic fields in the post-processing (Pfrommer et al. 2008) and scale the magnetic energy density field ϵ_B by the thermal energy density ϵ_{th} through the relation

$$\epsilon_B = \epsilon_{B_0} \left(\frac{\epsilon_{\text{th}}}{\epsilon_{\text{th}_0}} \right)^{2\alpha_B}, \quad (7)$$

where $\epsilon_{B_0} = B_0^2/(8\pi)$ and ϵ_{th_0} denote the core values. If not mentioned otherwise, we use the magnetic decline $\alpha_B = 0.5$ and the central magnetic field $B_0 = 10 \mu\text{G}$ throughout this paper. The central thermal energy density $\epsilon_{\text{th}_0} = 3P_{\text{th}_0}/2$, is calculated by fitting

⁴ The true CR particle momentum is denoted by P_p , but we loosely refer to $p = P_p/(m_p c)$ as the particle momentum.

⁵ The total CR proton spectrum is a sum of the spectra of the individual SPH particles within a certain volume, and since our sample contains a large number of SPH particles with varying normalization, the CRp spectral index is a statistically well defined continuous quantity.

the modified β -model

$$P(R) = P_{\text{th}_0} \left[1 + \left(\frac{R}{R_{\text{core}}} \right) \right]^{-\beta} \quad (8)$$

to the radial pressure $P(R)$. The parametrization in equation (7) is motivated by both cosmological MHD SPH simulations (Dolag et al. 1999) and radiative adaptive mesh refinement MHD simulations (Dubois & Teyssier 2008). Rather than applying a densities scaling as those simulations suggest, we use a scaling with thermal gas energy density which is not affected by the over-cooled centers in radiative simulations that do not take into account AGN feedback.

2.4 CR electron acceleration and inverse Compton emission

2.4.1 Modeling diffusive shock acceleration

Collisionless cluster shocks are able to accelerate ions and electrons through diffusive shock acceleration (for reviews see Drury 1983; Blandford & Eichler 1987; Malkov & O’C Drury 2001). Neglecting non-linear shock acceleration and cosmic ray modified shock structure, the process of diffusive shock acceleration uniquely determines the spectrum of the freshly injected relativistic electron population in the post-shock region that cools and finally diminishes as a result of loss processes. The γ -ray inverse Compton emitting electron population cools on such a short time scale $\tau_{\text{sync}} < 10^8$ yrs (compared to the long dynamical time scale $\tau_{\text{dyn}} \sim 2$ Gyr) that we can describe this by instantaneous cooling.⁶ In this approximation, there is no steady-state electron population and we would have to convert the energy from the electrons to inverse Compton and synchrotron radiation. Instead, we introduce a virtual electron population that lives in the SPH-broadened shock volume only; this is defined to be the volume where energy dissipation takes place. Within this volume, which is co-moving with the shock, we can use the steady-state solution for the distribution function of relativistic electrons and we assume no relativistic electrons in the post-shock volume, where no energy dissipation occurs. Thus, the cooled CR electron equilibrium spectrum can be derived from balancing the shock injection with the IC/synchrotron cooling: above a GeV it is given by

$$f_e(p_e) = C_e p_e^{-\alpha_e}, \quad C_e \propto \frac{\rho}{\varepsilon_B + \varepsilon_{\text{ph}}} \quad (9)$$

Here, we introduced the dimensionless electron momentum $p_e = P_e/(m_e c)$, where P_e is the electron momentum, $\alpha_e = \alpha_{\text{inj}} + 1$ is the spectral index of the equilibrium electron spectrum, ρ is the gas density, ε_B is the magnetic energy density, and ε_{ph} denotes the photon energy density, taken to be that of CMB photons. The primary CRE distribution in equation (9) is calculated in the post-processing with a spectrum reflecting the current Mach number of the shock (without the assumption of spectral bins). Superposing the individual spectra of a large number of SPH particles, each with a spectrum reflecting the accelerating shock, produces a well defined total spectrum with a running index in general. A more detailed discussion of this simplified approach can be found in Pfrommer et al. (2008).

Once the radiative cooling time due IC and synchrotron emission becomes comparable to the diffusive acceleration time

⁶ Assuming a magnetic field of a few μG and an electron density $n_e = 10^{-3} \text{ cm}^{-3}$, for further discussion see e.g. appendix in Pfrommer et al. (2008)

scale, the injection spectrum experiences a high-energy cutoff (Webb G.M. 1984). The electrons start to pile-up at this critical energy; the super-exponential term describing the maximum energy of electrons reached in this process, however, effectively cancels this pile-up feature which results in a prolonged power-law up to the electron cutoff momentum $p_e \sim p_{\text{max}}$ (Zirakashvili & Aharonian 2007). We account for this effect by using the following parametrization of the shock injected electron spectrum,

$$f_e(x, p_e) = C_e p_e^{-\alpha_{\text{inj}}} [1 + j(x, p_e)]^{\delta_e} \exp \left[\frac{-p_e^2}{p_{\text{max}}^2(x)} \right], \quad (10)$$

where x is the distance from the shock surface, $j(x, p_e)$ and δ_e describe the characteristic momentum and shape of the pile-up region. The continuous losses cause the cutoff to move to lower energies as the electrons are transported advectively with the flow downstream. Integration over the post-shock volume causes the cutoffs to add up to a new power-law that is steeper by unity compared to the injection power-law (equation 9). Hence, the shock-integrated distribution function – as defined in equation (B13) and displayed in Fig. B1 – shows three regimes: (1) at low energies (but large enough in order not to be affected by Coulomb losses) the original injected power-law spectrum, (2) followed by the cooled power-law that is steeper by unity, $\alpha_e = \alpha_{\text{inj}} + 1$, and (3) an ultimate cutoff that is determined from the magnetic field strength and the properties of the diffusion of the electron in the shock (we refer the reader to Section B2 for a detailed discussion). Note that only the last two regimes are important for γ -ray IC emission.

The fact that we observe X-ray synchrotron emission at shocks of young supernova remnants (Vink et al. 2006; Slane et al. 1999) necessarily requires the existence of high-energy CR electrons with $E_e \simeq 25$ TeV. The non-thermal synchrotron emission generated by CR electrons with energies $E_e > \text{GeV}$ is given by

$$h \nu_{\text{synch}} = \frac{3eBh}{2\pi m_e c} \gamma^2, \quad (11)$$

where $\gamma \sim 5 \times 10^7$ ($E_e \sim 25$ TeV) and magnetic fields of order $100 \mu\text{G}$ are required to reach X-ray energies of order 10 keV. To keep the highly relativistic electrons from being advected downstream requires efficient diffusion so that they can diffuse back upstream crossing the shock front again. We therefore use the most effective diffusion, referred to as Bohm diffusion limit, as the electron propagation model at the shock. Balancing Bohm diffusion with synchrotron/IC cooling of electrons enables us to derive a maximum energy of the accelerated CR electrons at the position of the shock surface (derived in appendix, see also Webb G.M. 1984; Enßlin et al. 1998)

$$E_{\text{max}} = \left[B e u^2 m_e c \tau_{\text{loss}} \frac{r_c - 1}{r_c (r_c + 1)} \right]^{0.5}, \quad (12)$$

where diffusion parallel to the magnetic field has been assumed. Here u denotes the flow velocity in the inertial frame of the shock ($u = v_s$), and the electron loss time scale due to synchrotron and inverse-Compton losses reads

$$\tau_{\text{loss}}^{-1} = \frac{\dot{E}}{E} = \frac{4\sigma_T \gamma}{3m_e c} (\varepsilon_B + \varepsilon_{\text{ph}}), \quad (13)$$

where σ_T is the Thompson cross-section. r_c denotes the shock compression and is given by

$$r_c = \frac{(\gamma_{\text{th}} + 1) \mathcal{M}^2}{(\gamma_{\text{th}} - 1) \mathcal{M}^2 + 2}, \quad (14)$$

Table 2. Electron energy cutoff in different regions of a typical cluster.

Cluster variables ⁽¹⁾	$< 0.03 R_{\text{vir}}$	$0.3 R_{\text{vir}}$	R_{vir}	WHIM
h_{sml} [kpc]	< 30	60	120	240
$n [10^{-3} \times \text{particles cm}^{-3}]$	4	0.4	0.04	0.004
r_c	1.3	2.3	3.0	3.7
\mathcal{M}	1.2	2	3	6
T [keV]	15	9	5	0.2
c_{sound} [km s ⁻¹]	2400	3100	3500	1400
B [μG]	10	2.5	0.6	0.04
E_{max} [TeV]	50	100	65	6.5

Notes:

(1) Other constants used: mean molecular weight $\mu = 0.588 m_p$.

where \mathcal{M} denotes the sonic Mach number. Inserting typical numbers for different cluster regions show that the electron cutoff energy, E_{max} , only varies within a factor two inside R_{vir} (Table 2). The equivalent cutoff energy in the IC spectrum can easily be derived from equation (6), yielding $E_{\text{IC,cut}} \approx 10 \text{ TeV} \times (E_{\text{max}}/50 \text{ TeV})^2$.

2.4.2 IC emission

Following Rybicki & Lightman (1979), we calculate the inverse Compton emission from electrons that up-scatter CMB photons. It should be noted that we neglect the inverse Compton emission induced by starlight and dust, which might contribute significantly in the inner 10 kpc of the cluster. The inverse Compton source density λ_{IC} in units of produced photons per unit time interval and volume for a simple power-law spectrum of CRes (equation 9) scales as

$$\lambda_{\text{IC}} \propto C_e \varepsilon_{\text{ph}} E_{\text{IC}}^{-\alpha_v}, \quad (15)$$

where $\alpha_v = (\alpha_e - 1)/2$. When we account for the competition between radiative cooling and diffusive acceleration of electrons in the shock region, the shape of λ_{IC} in the high-energy regime changes. Using the cooled electron distribution of equation (B13), we construct an effective integrated source function for primary inverse Compton emission (see Section B3 for a self-consistent and extensive description),

$$\lambda_{\text{pIC}} = \tilde{\lambda}_0(\zeta_{e,\text{max}}, C_e) f_{\text{IC}}(\alpha_e) f_{\text{KN}}(E_{\text{IC}}, \alpha_e) \left(\frac{E_{\text{IC}}}{kT_{\text{CMB}}} \right)^{-\frac{\alpha_e-1}{2}} \times \left(1 + 0.84 \sqrt{\frac{E_{\text{IC}}}{E_{\text{IC,cut}}}} \right)^{\delta_{\text{IC}}(E_{\text{IC}}, \alpha_e)} \exp\left(-\sqrt{\frac{4.07 E_{\text{IC}}}{E_{\text{IC,cut}}}} \right), \quad (16)$$

where Bohm diffusion has been assumed. The normalization constants $\tilde{\lambda}_0(\zeta_{e,\text{max}}, C_e)$ and $f_{\text{IC}}(\alpha_e)$ are derived in equations (B20) and (B19), respectively. The KN suppression of the IC spectrum is captured by $f_{\text{KN}}(E_{\text{IC}}, \alpha_e)$ (equation B22), and the shape of the transition region from the Thompson to the KN regime is given by $\delta_{\text{IC}}(E_{\text{IC}}, \alpha_e)$ (equation B24). Following recent work that carefully models the non-thermal radiation of young supernova remnants (Zirakashvili & Aharonian 2010), we typically adopt a maximum electron injection efficiency of $\zeta_{e,\text{max}} = 0.01$. We note that this value seems to be at the upper envelope of theoretically allowed values that match the supernova data.

2.5 Multiphase structure of the ICM

The ICM is a multiphase medium consisting of a hot phase which attained its entropy through structure formation shock waves dissipating gravitational energy associated with hierarchical clustering into thermal energy. The dense, cold phase consists of the true interstellar medium (ISM) within galaxies and at the cluster center as well as the ram-pressure stripped ISM that has not yet dissociated into the ICM (Dolag et al. 2009). All of these phases contribute to the γ -ray emission from a cluster. Physically, the stripped ISM should dissociate after a time scale that depends on many unknowns such as details of magnetic draping of ICM fields (Dursi & Pfrommer 2008; Pfrommer & Dursi 2009) on galaxies or the viscosity of the ICM. In SPH simulations, this dissociation process is suppressed or happens only incompletely in our simulations leaving compact galactic-sized point sources that potentially biases the total γ -ray luminosity high. On the other hand, once these stripped compact point sources dissociate, the CRs diffuse out in the bulk of the ICM, and produce γ -rays by interacting with protons of the hot dilute phase. This flux, however, is negligible since

$$L_{\text{diff.-CRs}} \propto \int dV n_{\text{diff.-CRs}} n_{\text{icm}} \propto \int dV n_{\text{ism-CRs}} n_{\text{ism}} \left(\frac{n_{\text{icm}}}{n_{\text{ism}}} \right)^2 \sim L_{\text{icm-CRs}} \left(\frac{n_{\text{icm}}}{n_{\text{ism}}} \right)^2, \quad \text{where } \frac{n_{\text{icm}}}{n_{\text{ism}}} \sim 10^{-3}. \quad (17)$$

Here n_{icm} (n_{ism}) denotes the gas number density in the ICM (ISM), $n_{\text{ism-CRs}}$ the CR number density in the ISM, and $n_{\text{diff.-CRs}}$ the CR number density of the CRs that diffused out of their dense ISM environment into the ambient ICM that is in pressure equilibrium with the ISM. In the second step of equation (17) we accounted for the adiabatic expansion that these CRs would experience as they diffused out. In the last step we assumed $L_{\text{ism-CRs}} \sim L_{\text{icm-CRs}}$, i.e. that the CR luminosity of all compact galactic sources in a cluster is of the same order as the CR luminosity in the diffuse ICM; a property that is at least approximately true in our simulations as we will show later on. Leaving all gaseous point sources would definitively be too optimistic, removing all of them would be too conservative since cluster spiral galaxies should contribute to the total γ -ray emission (which defines our so-called *optimistic* and *conservative* models). Hence, we perform our analysis with both limiting cases, bracketing the realistic case. The effect from the gaseous point sources is largest in low mass clusters, where they constitute a few percent of the total ICM mass. For high-mass clusters this fraction is lower, and constitutes only about one percent. In practice, we cut multiphase particles with an electron fraction $x_e < 1.153$ and a gas density above the star forming threshold $2.8 \times 10^{-25} \text{ g cm}^{-3}$. If nothing else is stated, we use our conservative model without galaxies throughout the paper.

3 CHARACTERISTICS OF γ -RAY EMISSION

From surface brightness S_γ maps that are obtained by line-of-sight integration of the source functions, we study the γ -ray emission to characterize the morphology of clusters. Additionally, we use emission profiles to compare pIC, sIC, and pion decay induced emission for different clusters.

3.1 Morphology of γ -ray emission

The left side of Fig. 2 shows the morphology of the γ -ray emission above 100 GeV that results from hadronic CR interactions with am-

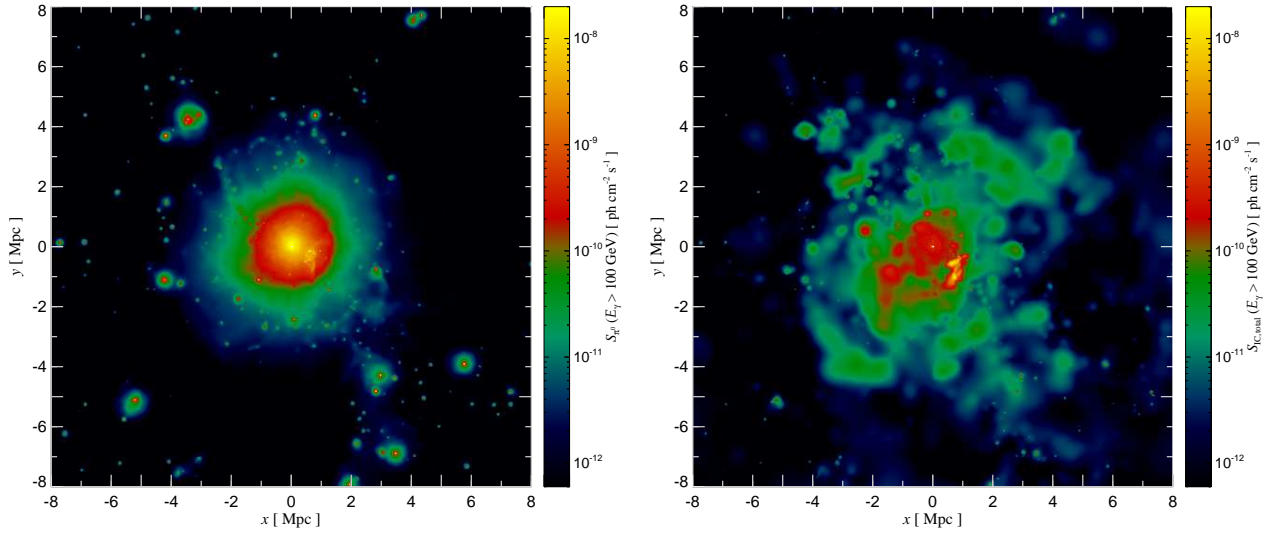


Figure 2. The γ -ray emission above 100 GeV of our Coma-like cluster g72a is shown. We show the pion decay γ -ray emission that originates from hadronic CR interactions with ambient gas protons on the left. On the right, we plot the inverse Compton emission from both, primary and secondary CR electrons. Comparing the different γ -ray emission components, we note that the pion decay has a very regular morphology and clearly dominates the cluster region. In contrast, the emission from primary electrons shows an irregular morphology that traces the structure formation shock waves and dominates in the virial periphery and the warm-hot intergalactic medium.

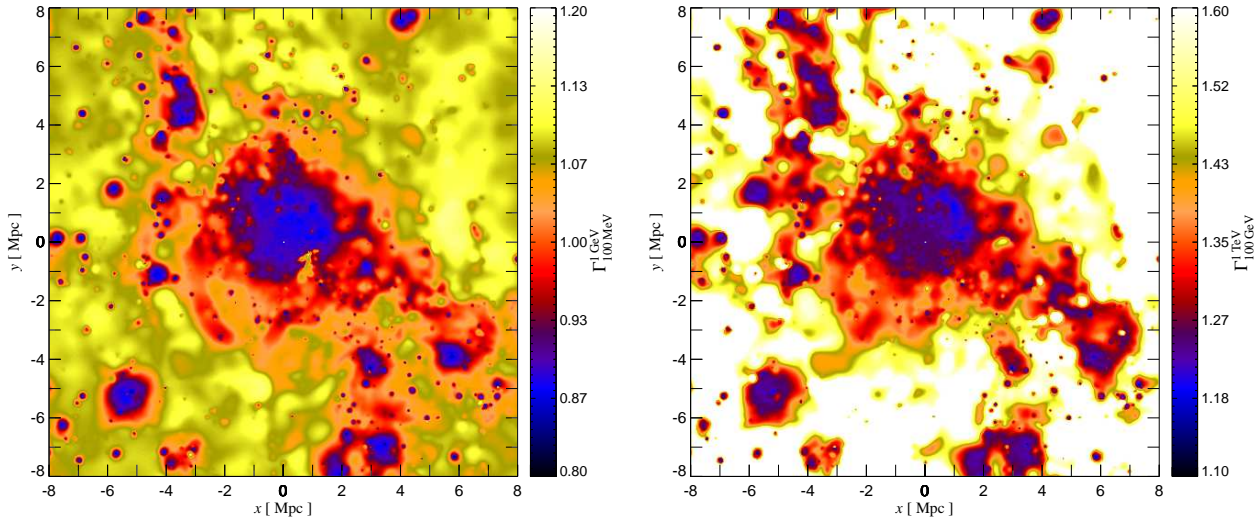


Figure 3. Projected energy dependent photon index for the galaxy cluster g72a. On the left, we show the photon index between 100 MeV – 1 GeV and on the right, the photon index between 100 GeV – 1 TeV. Note that the central part (where pion decay dominates) shows little variations which reflects the spectral regularity of the CR distribution. At the periphery and beyond, there are larger fluctuations due to the inhomogeneity of the pIC emission.

ambient gas protons. The right side shows the primary and secondary IC emission for the post-merger cluster g72a. The comparison of the two panels shows that the central parts are dominated by the pion induced γ -ray emission. It has a very regular morphology that traces the gas distribution. There is a transition to the pIC emission as the dominant emission mechanism outside the cluster in the WHIM at a level depending on the dynamical state of the cluster. The pIC emission is very inhomogeneous which can be easily understood since it derives from primary CR electrons that are directly accelerated at structure formation shocks. Structure formation is not a steady process, it rather occurs intermittently. The morphology of the γ -ray emission above 100 MeV for g72a was investigated

in Pfrommer et al. (2008). It shows a very similar morphology, indicating a similar power-law CR spectrum.

The projected energy dependent photon index is a well defined continuous quantity as it is defined through

$$\Gamma \equiv -\frac{d \log S_\gamma}{d \log E_\gamma} \quad \rightarrow \quad \Gamma_{E_1}^{E_2}(\mathbf{R}_\perp) = -\frac{\log \left[\frac{S_\gamma(E_1, \mathbf{R}_\perp)}{S_\gamma(E_2, \mathbf{R}_\perp)} \right]}{\log \left(\frac{E_1}{E_2} \right)}, \quad (18)$$

where $S_\gamma(E_\gamma, \mathbf{R}_\perp)$ is the surface brightness of γ -rays with energies $> E_\gamma$ at the projected radius \mathbf{R}_\perp . Using S_γ maps, such as the ones in Fig. 2, we can extract the photon index $\Gamma_{E_1}^{E_2}$ between the energies E_1 to E_2 . Close to the pion bump (see Fig. 1) at $m_{\pi^0}/2 \approx 68.5$ MeV

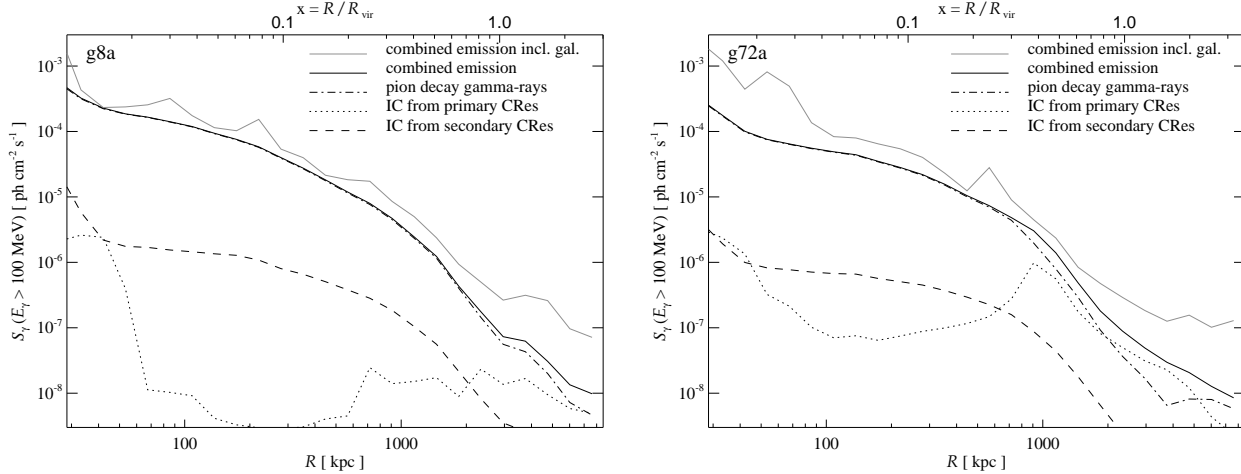


Figure 4. Azimuthally averaged profiles of the γ -ray emission components above 100 MeV for two different clusters: large cool core (CC) g8a (left panel) and large merger g72a (right panel). Shown are the dominating pion decay induced emission (dash-dotted lines), the IC emission of primary CR electrons accelerated directly at structure formation shocks (dotted lines), the secondary IC electrons resulting from CRp-p interactions (dashed lines) and the sum of all emission components (thick line). We cut the galaxy emission from our individual emission components in both panels and additionally show the total emission including galaxies (grey solid line).

(energy of a photon originating from a decaying π^0 at the threshold of the hadronic p-p reaction) the photon spectrum has a convex shape. This is characterized by a flatter photon index compared to the asymptotic limit, $E_\gamma \gg m_{\pi^0}c^2$. Calculating $\Gamma_{E_1}^{E_2}$ at two discrete energies results in a slightly steeper value for $\Gamma_{E_1}^{E_2}$ than its continuous counterpart Γ at E_1 .

Since we are interested in comparing the morphology of clusters to spectra, we calculate the projected photon index for g72a (see Fig. 3). We compare $\Gamma_{E_1}^{E_2}$ for an energy regime accessible to the *Fermi space telescope* of 100 MeV – 1 GeV (left panel) to 100 GeV – 1 TeV accessible for IACTs (right panel). In the *Fermi regime*, we find a median value of $\Gamma_{100\text{MeV}}^{1\text{GeV}} \approx 0.9$ in the central regions of the cluster and a value $\Gamma_{100\text{MeV}}^{1\text{GeV}} \approx 1.1$ in the periphery. The reason is that the total emission in the central regions of the cluster is dominated by the pion decay emission at 100 MeV with a lower spectral index than pIC due to the pion bump. In the periphery and the WHIM, where the pIC contributes substantially to the total emission, intermediate shocks with $\mathcal{M} \sim 4$ are typical (Pfrommer et al. 2006). Using the spectral index of the electron equilibrium spectrum, $\alpha_e = \alpha_{\text{inj}} + 1$, where $\alpha_{\text{inj}} \approx 2.2$ for $\mathcal{M} \approx 4$ and $S_{\text{IC}} \sim E_{\text{IC}}^{-(\alpha_e-1)/2} \approx E_{\text{IC}}^{-1.1}$, results in the observed steepening of $\Gamma_{100\text{MeV}}^{1\text{GeV}}$ in the periphery.

We now turn to the energy region important for IACTs with the photon index $\Gamma_{100\text{GeV}}^{1\text{TeV}}$. In the central regions the photon index traces the proton spectral index $\Gamma_{100\text{GeV}}^{1\text{TeV}} = \alpha - 1 \sim 1.25$ since this spatial region is dominated by the asymptotic regime of the pion emission. Moving towards the periphery, the photon index steepens to $\Gamma_{100\text{GeV}}^{1\text{TeV}} > 1.4$, despite the presence of strong external shocks as well as accretion shocks that efficiently accelerate electrons on these large scales. The reason for this steepening is the exponential cutoff in the pIC emission. Increasing the energy or the distance from the cluster results in an even steeper photon index.

3.2 Emission profiles

The profiles of different non-thermal γ -ray emission processes without galaxies are shown in Fig. 4 for, a large CC cluster (g8a, left) and large post-merging cluster (g72a, right). The *secondary*

IC emission traces the dominating *pion decay emission* because to zeroth order, both components depend on $n_{\text{gas}}n_{\text{CR}}$, where n_{gas} is the gas number density and n_{CR} the CR number density. This would be exactly true if the magnetic field was smaller than $B_{\text{CMB}} \approx 3\mu\text{G}$. In this case, the CRE population would exclusively cool by means of IC emission. Since we assume the central magnetic field to be larger than B_{CMB} , a fraction of the CRE energy is radiated through synchrotron emission into the radio, causing a larger discrepancy of the sIC emission compared to the pion emission in the center.

In contrast to the centrally peaked secondary emission components, the average *primary IC emission* shows a rather flat surface brightness profile which can be nicely seen in our cool core cluster g8a. This is because we see the strong accretion shocks that efficiently accelerate CRes (in terms of the injected energy density) in projection. There are noticeable exceptions in the centers of both clusters: accreting small sub-clumps dissipate their gravitational energy through weak shocks in the larger core regions of clusters. However, once these weak shock waves encounter the (over-cooled) centers of our simulated clusters they transform into strong (high Mach number) shock waves. These inject a hard population of primary CR electrons which causes the centrally peaked and bright pIC emission. We also observe an excess pIC emission at a radius of ~ 1 Mpc in g72a. This can be traced back to a prominent merger shock wave with a Mach number up to $\mathcal{M} \approx 3.5$ that accelerates primary CRes (see also Fig. 2).

The *total emission* flattens out in the cluster exterior close to R_{vir} because of two reasons: (1) there the pIC emission contributes significantly to the total emission because of strong merger shocks as well as accretion shocks, and (2) subhalos in the periphery that have not yet merged with the larger halo contribute to the pion decay induced emission. In this regime, the halo-halo correlation term starts to dominate the average density profile of a cluster with its characteristic flattening (Hayashi & White 2008). This naturally translates to the pion emission profile that tightly correlates with the gas density distribution.

The *ratio between pion decay and sIC emission* can be estimated analytically by calorimetric considerations. To this end we compare the CR energy spectrum, $E^2 f(E)$, at the respective CR energies which give rise to γ -ray emission at some specific pho-

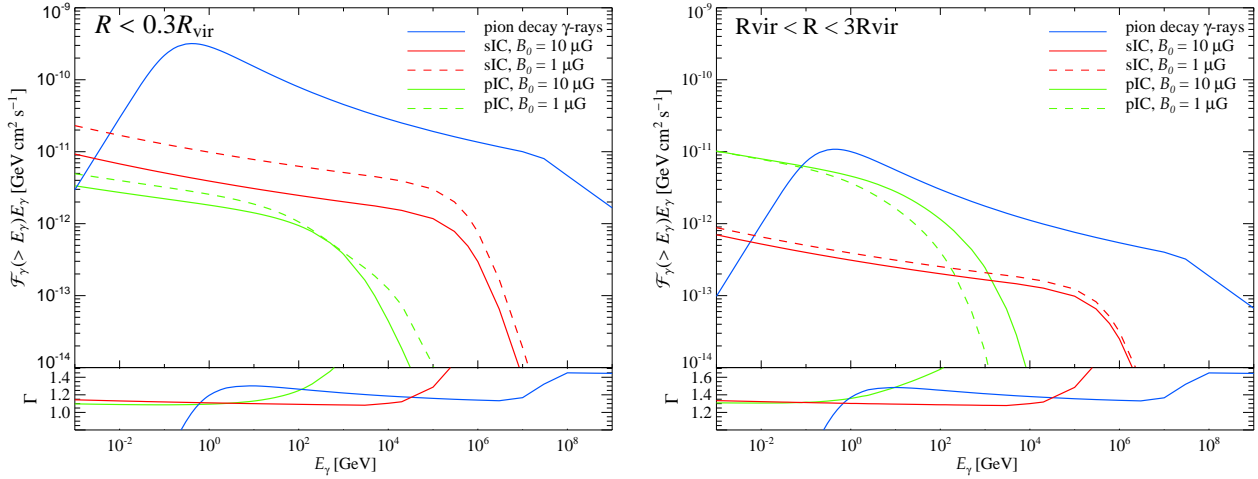


Figure 5. The γ -ray number flux weighted by photon energy of our Coma-like cluster g72a: core region (left panel) and WHIM region (right panel). The pion decay flux is shown in blue color, the secondary IC in red, and the primary IC emission in green. The solid IC lines assume a central magnetic field strength of $B_0 = 10 \mu\text{G}$ while the dashed lines assume $B_0 = 1 \mu\text{G}$. The lower panels show the photon spectral index Γ for each emission component, where the colors are the same as in the upper panel. Note that in the core region ($R < 0.3 R_{\text{vir}}$) the pion decay induced flux dominates the emission. In the WHIM region ($R_{\text{vir}} < R < 3 R_{\text{vir}}$) the pion decay and sIC emission components are much smaller compared to the central part. Contrary, the pIC component is boosted in the WHIM due to accretion shocks onto our simulated cluster. Nevertheless, its emission falls slightly short of the pion decay.

ton energy, say $E_\gamma = 1 \text{ GeV}$. Additionally we have to include a factor, f_B , that accounts for the possibility that the CRe do not only emit IC γ -rays but also radio synchrotron radiation. Using the hadronic branching ratios for the production of pions, $R_{\pi^0} \simeq 1/3$ and $R_{\pi^\pm} \simeq 2/3$, as well as the multiplicities for the decay products in the respective decay channels, $\xi_{\pi^0 \rightarrow \gamma} \simeq 2$ and $\xi_{\pi^\pm \rightarrow e^\pm} \simeq 1/4$, we obtain

$$\frac{E_{p,\pi^0}^2 s_{\pi^0}}{E_{p,\text{sIC}}^2 s_{\text{sIC}}} \Big|_{1 \text{ GeV}} \simeq \frac{R_{\pi^0} \xi_{\pi^0 \rightarrow \gamma}}{R_{\pi^\pm} \xi_{\pi^\pm \rightarrow e^\pm}} \left(\frac{E_{p,\pi^0}}{E_{p,\text{sIC}}} \right)^{-\alpha_{\pi^0}^{\text{sIC}} + 2} f_B \simeq 30 f_B. \quad (19)$$

Here $\alpha_{\pi^0}^{\text{sIC}} \simeq 2.3$ is the CR proton spectral index between the CR energy $E_{p,\pi^0} = 8.0 \text{ GeV}$ that give rise to pion decay flux at 1 GeV and the CR energy $E_{p,\text{sIC}} = 8.0 \text{ TeV}$ that gives rise to sIC flux at 1 GeV. The γ -ray source function for pion decay and sIC ((Pfrommer & EnBlin 2004)) is denoted by s_{π^0} and s_{sIC} , respectively. Finally, the factor $f_B = (B/B_{\text{CMB}})^2 + 1 \simeq 1$, for magnetic fields much smaller than the CMB equivalent magnetic field, otherwise $f_B > 1$. In the region close to $0.3 R_{\text{vir}}$, the magnetic field is about $2.4 \mu\text{G}$ in our model (Table 2), which implies an emission ratio of about 50. For smaller photon energies than 1 GeV, the pion decay γ -ray emission falls below the asymptotic power-law due to the characteristic pion bump. This effect implies a lower ratio of about 40 (instead of the expected ratio of about 100) for the emission above 100 MeV in Fig. 4.

We also show the *total surface brightness profile with galaxies* in Fig. 4 (grey line). The resulting profile shows a boosted emission by about a factor two compared to the one where we exclude galaxies from the surface brightness. The entire population of these galaxies takes up only a negligible volume so that the volume weighted CR pressure is almost the same in either case, when taking these galaxies into account or not. We note that this bias needs to be addressed when deriving average CR pressure contributions from the cluster's γ -ray emission (Aleksić et al. 2010). Especially in the inner parts, the profile is very inhomogeneous. Since galaxies follow an approximate Poisson distribution and since the inner radial bins of the profile sample only few galaxies, we naturally obtain a larger Poissonian scatter across the inner radial bins.

3.3 Emission spectra from the cluster core and WHIM

The central parts of clusters are characterized by high gas and CR densities, and magnetic fields – at least compared to average values of the ICM. Even though the cluster core region only makes up a fraction of the total volume of the ICM, the high densities result in a significant γ -ray flux contribution to the total flux from the cluster. In contrast to the cluster center, the WHIM is characterized by on average low gas and CR densities, and magnetic fields. The low densities cause a smaller total γ -ray flux from this region compared to the cluster core regions. However, the WHIM of the super-cluster region contains a large number of galaxies and groups that are accreted onto the cluster. This generates more shocks compared to the cluster core region. The cluster characteristics in the two regions give rise to different normalizations of the individual γ -ray emission components, but with a similar shape. The shape of the emission components from the different regions agrees with that of the entire cluster as shown in Fig. 1. The emission can be summarized as follows. The π^0 -decay is characterized by the so-called pion bump followed by a concave curvature and a diffusive break. The pIC emission component shows a power-law followed by an exponential cutoff while the sIC component has a power-law with similar index that is however followed by the Klein-Nishina break.

In Fig. 5 we show the γ -ray number flux weighted by photon energy from different regions of our Coma-like cluster g72a that we place at the distance of 100 Mpc. The left figure shows the γ -ray number flux within the core region ($R < 0.3 R_{\text{vir}}$), where the π^0 -decay dominates over the sIC component that itself is subdominant to the pIC component. The surface brightness profile of the π^0 -decay is sufficiently flat in the core region so that the γ -ray flux is dominated by the outer scale around $R \sim 0.3 R_{\text{vir}}$ where most of the volume is. Hence the π^0 -decay flux is largely insensitive to numerical inaccuracies of our modeling of the physics at the very center of the cluster. Both the pIC and sIC emission components have a larger γ -ray flux in our models with weak central magnetic fields ($B_0 = 1 \mu\text{G}$, $f_B \simeq 1$) compared to our models with strong central magnetic fields ($B_0 = 10 \mu\text{G}$, $f_B \simeq 2$). The sIC emission with

$B_0 = 10 \mu\text{G}$ is characterized by $B \simeq B_{\text{CMB}}$ on scales around the core radius which is the region that dominates the flux. Relative to the pion decay emission, the sIC is suppressed by a factor of ~ 60 which can be understood by considering hadronic decay physics and the fact that the CR energy spectrum, $E^2 f(E)$, is decreasing as a function of proton energy (see equation 19). Even though the pIC emission component is sub-dominant, it shows a rather flat spectral index. This implies only a few strong shocks that are responsible for the electron acceleration. These merging shock waves are traversing the cooling core region in the cluster center. We caution the reader that the over-cooling of the cluster centers in our simulations possibly overestimates the true shock strengths and numbers which also results in an artificially enhanced pIC emission. At high energies, the electron cooling time is smaller than the time scale for diffusive shock acceleration which causes an exponential cutoff in the electron spectrum which is passed on to the pIC spectrum. The energy scale of the cutoff $E_{\text{IC,cut}}$ (combining equations 6 and 12) scales with the magnetic field which causes the low magnetic field model to turn down faster than the large magnetic field model. Note that the second cutoff in the figure for the small central magnetic fields is caused by a small fraction of the particles that have unusually high electron energy cutoff. The lower panel shows the photon spectral index defined in equation (18), where $\Gamma \simeq 1.3$ for the π^0 -decay emission after the pion bump that slowly flattens out with energy. For both the pIC and sIC emission the photon spectral index $\Gamma \simeq 1.1$ above the MeV regime up to at about 100 GeV. The reason for the flat spectra is that the pIC emission is generated by a few strong shocks in the center, while the sIC emission is caused by protons in the flat high energy part of CR spectrum.

Now we turn to the γ -ray spectra in the WHIM which are shown in the right panel of Fig. 5 for our g72a cluster. Here we define the WHIM by the emission in the region $R_{\text{vir}} < R < 3R_{\text{vir}}$ as seen in 2D projection of the cluster. We see that the pion decay and sIC are suppressed by a factor that is larger than 10 compared to the flux within the core region since the emission correlates with the CR- and gas densities. The suppression of γ -ray flux emitted by the intergalactic medium is expected to be much greater due to the large density decrease. The presence of small groups in the super-cluster region with densities that are much larger than the average density in the WHIM partially counteracts the flux suppression. Contrary to the pion decay and sIC component, the pIC emission is boosted by a factor of a few compared to the center because of the larger spatial region in the WHIM that contains a greater number of shocks. This leads to *comparable flux from the pIC and pion decay emission above the energy of the pion bump in the super-cluster region*. Note however, that this flux is still sub-dominant compared to the pion decay flux emitted by the cluster core region. The different central magnetic fields do not play any significant role in the power-law regime in the WHIM since $B \ll B_{\text{CMB}}$, which implies that the CRs mainly cool through IC emission. However, note that the pIC cutoff is shifted towards lower energies for these smaller magnetic fields since $E_{\text{IC,max}} \propto B/(B^2 + B_{\text{CMB}}^2) \propto B/B_{\text{CMB}}^2$ (as derived by combining equations 6 and B15). In the lower panel we show that the photon spectral index is steeper in the WHIM for all three emission components compared to the core region. The photon index is about 1.3 for both pIC and sIC below 10 GeV and about 1.4 for the pion decay above the energy of the pion bump. The reason for the steeper pIC is because most of the energy that is injected into primary electrons comes from multiple intermediate-strength shocks (accretion shocks), while in the cluster center the pIC emission is build up from a few strong shocks in the over-cooled center (merger shocks). The steeper sIC and pion decay photon indices are caused

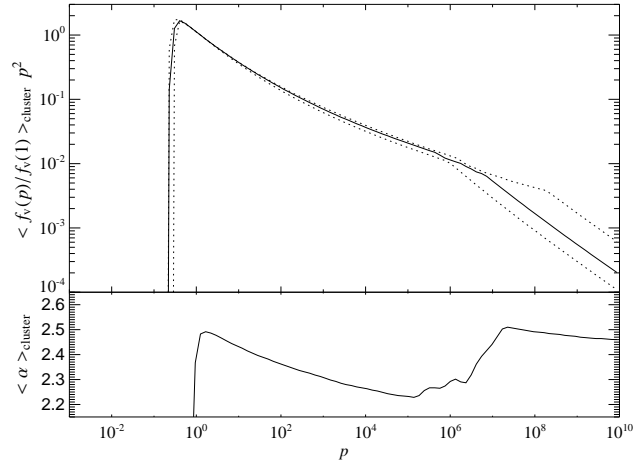


Figure 6. Spectral universality across our cluster sample: we show the median CR proton spectrum (solid line) as a function of dimensionless CR momentum $p = P_p/m_p c$ for our sample of 14 galaxy clusters in Table 1 together with the 68 percentiles (dotted lines). The CR spectrum of every cluster, $f_v(p)$, has been obtained by volume weighting the individual spectra of our SPH particles and normalizing them at $p = 1$. Note the small variance between different clusters below the diffusive break, which indicates a universal CR spectrum for galaxy clusters. The large scatter in the $p = 10^6 - 10^8$ momentum regime is a consequence of the strong radial dependence of the diffusive break. The lower panel shows the CR spectral index $\alpha = -d \log f / (d \log p)$ of the cluster sample.

by the slightly steeper CR spectrum present in the WHIM of the g72a cluster (cf. Fig. 7).

4 THE CR PROTON DISTRIBUTION

In this section we investigate the CR proton spectrum that we obtain from our simulations and discuss the relevant physics that gives rise to it. We explore the variance of the spectrum across our cluster sample and within individual clusters and show that it obeys a universal spectral shape. In addition, we study the spatial profile of the CRs within a cluster as well as across our cluster sample and find it to be approximately universal. This universal behavior enables us to construct a semi-analytic CR spectrum and to compute the γ -ray spectrum as well as other secondary decay spectra (electrons, neutrinos) semi-analytically.

4.1 A universal CR spectrum

In Fig. 6 we show the median CR spectrum of all 14 galaxy clusters as well as the associated spectral index alpha. The CR spectrum of every cluster, $f_v(p)$, has been obtained by volume weighting the individual spectra of our SPH particles which have been normalized at the dimensionless proton momentum $p = P_p/m_p c = 1$. Before discussing the spectral shape we note that it shows a remarkably small variance across our cluster sample which indicates a universal CR spectrum for galaxy clusters. There are three important features in the spectra.

(i) The spectrum shows a *low-momentum cutoff* due to efficient Coulomb cooling at these low momenta with $p \lesssim 1$: the CR energy is transferred into the thermal energy reservoir through individual electron scatterings in the Coulomb field of the

CR particle (Gould 1972). The Coulomb time scale of a mono-energetic CR population is very short, $\tau_{\text{Coul}} = E_{\text{CR}}/\dot{E}_{\text{CR,Coul}} \approx 0.03 \text{ Gyr} \times (p/0.1)^3 (n_e/10^{-3} \text{ cm}^{-3})^{-1}$, where we show a momentum scaling that is valid only for the relevant non-relativistic regime. The Coulomb time scale for a power-law population of CRs can be significantly longer, $\tau_{\text{Coul}} = \varepsilon_{\text{CR}}(C, q, \alpha)/\dot{\varepsilon}_{\text{CR}}(C, q, \alpha)_{\text{Coul}} \approx 1 \text{ Gyr} \times (n_e/10^{-3} \text{ cm}^{-3})^{-1}$, where we assumed a low-momentum cutoff $q = 0.1$ and $\alpha = 2.5$ (Enßlin et al. 2007). This, however, is still short compared to the dynamical time scale $\tau_{\text{dyn}} \sim 2 \text{ Gyr} \times (n_e/10^{-3} \text{ cm}^{-3})^{-1/2}$. Hence, we expect the formation of an equilibrium cutoff of our CR spectrum around $q \approx 0.1 \dots 1$ for the typical number densities $n_e \sim (10^{-3} \dots 10^{-2}) \text{ cm}^{-3}$ that we encounter at the cluster cores. Note that in the presence of cooling processes only, the equilibrium cutoff q is determined from the competition between Coulomb cooling and hadronic losses and converges around $q = 1.685$ if the cooling time is sufficiently short (see Jubelgas et al. (2008) for a detailed discussion). The reason for that is that Coulomb cooling shifts the cutoff to higher momenta, as the CRs with low momenta are transferred to the thermal reservoir. At high momenta, the cooling time due to hadronic interactions is shorter than the Coulomb cooling time. Hadronic cooling effectively removes the CRs with high energy and moves the cutoff towards lower momenta.

(ii) In the momentum range between $p \approx 1 - 10^6$, the spectrum has a *concave shape* in double-logarithmic representation, i.e. it is a decreasing function with energy in the GeV/TeV energy regime. This is quantified by the momentum dependent spectral index (shown in the lower panel of Fig. 6) which ranges from $\alpha \sim 2.5$ at energies above a GeV to $\alpha \sim 2.2$ around 100 TeV. This spectral shape is a consequence of the cosmological Mach number distribution that is mapped onto the CR spectrum (Pfrommer et al. 2006). This mapping depends on the shock acceleration efficiency as a function of shock strength as well as on the property of the transport of CRs into galaxy clusters. Nevertheless, we can easily understand the qualitative features: the typical shocks responsible for CR acceleration are stronger at higher redshift since they encounter the cold unshocked inter-galactic medium.⁷ This implies the build-up of a hard CR population. Since the forming objects have been smaller in a hierarchically growing Universe, their gravity sources smaller accretion velocities which results in smaller shock velocities, v . Hence the energy flux through the shock surfaces, $\dot{E}_{\text{diss}}/R^2 \propto \rho v^3$, that will be dissipated is much smaller than for shocks today. This causes a lower normalization of this hard CR population. With increasing cosmic time, more energy is dissipated in weaker shocks which results in a softer injection spectrum. Despite the lower acceleration efficiency, the normalization of the injected CR population is larger than that of the older flat CR population which yields an overall concave spectral curvature. We will study the details of the CR acceleration and transport that leads to

⁷ Note that after re-ionization, the UV background sets a temperature floor by photo-ionizing the intergalactic medium (IGM) to temperatures of about $T \sim 10^4 \text{ K}$ except for void regions where the densities are too small so that the photo-ionization heating rate is smaller than the expansion rate (Katz et al. 1996). As time progresses, formation shocks dissipate energy and heat the IGM to temperatures of $T \sim (10^5 - 10^7) \text{ K}$ which is even heated further as it is accreted onto clusters. Since the sound-speed is proportional to $T^{0.5}$, we expect a higher sound-speed in (pre-)collapsed objects at low redshifts which results in weaker shocks at later times. This is quantified in the redshift evolution of the Mach number distribution (Ryu et al. 2003; Pfrommer et al. 2006) that also confirms the argument given above.

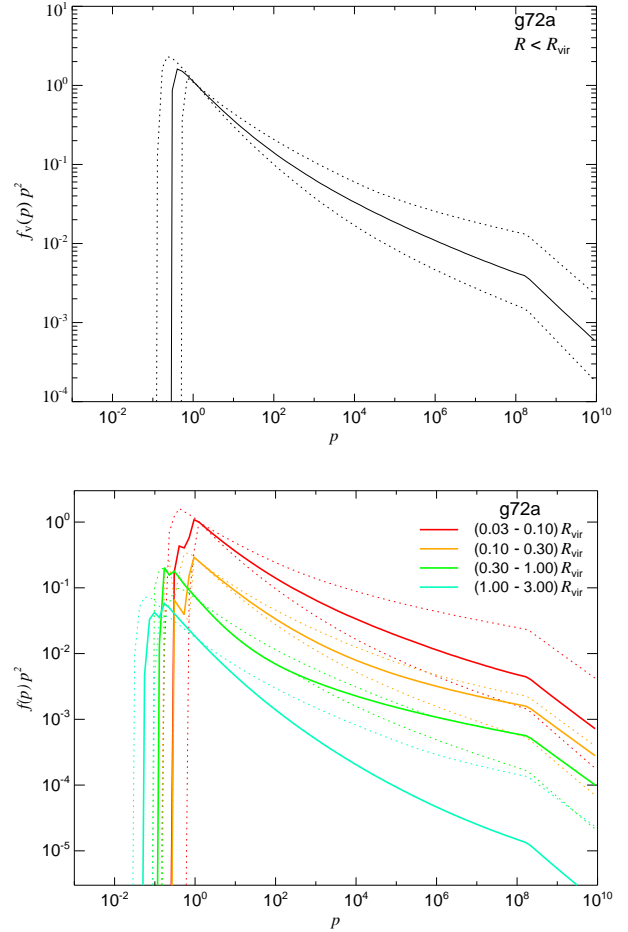


Figure 7. Spectral universality within a cluster – variance and radial dependence: we show the CR proton spectrum of a large merging cluster, g72a, as a function of dimensionless CR momentum $p = P_p/m_p c$. *Top:* median of the volume weighted and normalized CR spectrum $f_v(p)p^2$ (solid) and particle-by-particle variance as indicated by the 68 percentiles (dotted line). *Bottom:* volume weighted CR proton spectrum (median and 68 percentiles) for different radial bins. Those are represented by different colors: core region of the intra-cluster medium in red, the intermediate cluster scales in orange, the periphery of the ICM in green, and the WHIM in blue. The spectrum for the different radial bins has been offset vertically by a constant factor of four, with decreasing amplitude for increasing radius. The shift of the cutoff q to a higher momentum for smaller radius is due to the smaller CR cooling time scales in denser regions. Note that the cosmic ray spectrum inside the virial radius is almost independent of radius. This behavior is not only observed for this cluster, but persistent across our cluster sample.

that particular spectrum in a forthcoming paper (Pinzke & Pfrommer, in prep.).

(iii) There is a *diffusive break* in the spectrum at high momenta where the spectral index steepens by 0.3. The CRs above these energies can diffusively escape from the cluster within a Hubble time. The particular value of the steepening assumes that the CRs scatter off Kolmogorov turbulence. Using twice the virial radius of each cluster, we find that the diffusive break varies between the momenta $p = 10^6 - 10^8$, dependent on the characteristic size of a cluster (equation 3).

We now turn to the question on how universal is our CR spectrum within a cluster. In Fig. 7 we find that the intrinsic scatter of our CR spectra within a cluster is larger than the scatter among

clusters. The reason being that formation shocks are intermittent as mass is accreted in clumps and not continuously. Hence there is a high intrinsic variance of the CR spectrum for similar fluid elements that end up in the same galaxy cluster. However, averaging over all fluid elements that accrete onto a galaxy cluster results in a very similar spectrum since different galaxy cluster experience on average the same formation history.⁸ We note that the spectral variance of g72a is representative for all the CR spectra in our sample.

We study the radial dependence of the CR spectrum for g72a at the bottom of Fig. 7. Inside the cluster, the spectral shape does not strongly depend on the radius. This is a crucial finding as it enables us to *separate the spectral and the spatial part* of the CR distribution. The level of particle-by-particle variance is similar to that of the total cluster spectrum. Also noticeable is the increasing low-momentum cutoff q as we approach the denser cluster center. This is due to enhanced Coulomb losses and to a lesser extent increased adiabatic compression that the CR distribution experienced when it was transported there. Outside the cluster g72a, for radii $R > R_{\text{vir}}$, we observe a considerably steeper CR spectrum at CR energies of $E \gtrsim 1$ TeV compared to the cluster region. We note that this behavior is not universal and we observe a large scatter of the CR spectral indices among our cluster sample at these large radii. This behavior might be caused by the recent dynamical activity of the cluster under consideration but a detailed characterization goes beyond the scope of this work and will be postponed (Pinzke & Pfrommer, in prep.).

4.2 The spatial distribution of CRs

We have shown that the CR spectrum is separable in a spectral and spatial part. To this end, we quantify the spatial part of the CR spectrum by taking the volume weighted CR spectrum in each radial bin i (see Section A1 in the appendix for derivation),

$$f_v(R_i) \equiv \langle f \rangle_v(p=1, R_i) = C_v(R_i) = \tilde{C}_M(R_i) \frac{\rho_v(R_i)}{m_p}. \quad (20)$$

Here we assume $q < 1$, the subscripts M and V denote mass- and volume weighted quantities, respectively, and we introduced the dimensionless normalization of the CR spectrum,

$$\tilde{C}(\mathbf{R}) = m_p \frac{C(\mathbf{R})}{\rho(\mathbf{R})} = m_p (\alpha - 1) q^{\alpha-1} \frac{n_{\text{CR}}(\mathbf{R})}{\rho(\mathbf{R})}, \quad (21)$$

where n_{CR} is the CR number density. We now have to take into account physical effects that shape the profile of \tilde{C} . Those include acceleration of CRs at structure formation shocks, the subsequent adiabatic transport of CRs during the formation of the halos as well as non-adiabatic CR cooling processes; primarily hadronic interactions. At the same time we have to consider the assembly of the thermal plasma and CRs within the framework of structure formation that is dominated by CDM. Hierarchical structure formation predicts a difference in the halo formation time depending on the halo mass, i.e. smaller halos form earlier when the average mass density of the Universe was higher. This leads to more concentrated density profiles for smaller halo masses; an effect that breaks the scale invariance of the dark matter halo profile (Zhao et al. 2009). The central core part is assembled in a regime of fast accretion

⁸ The reason for our increased scatter at higher energies is that we normalize the spectrum of each SPH particle at $p = 1$ where the softest CR populations dominate. Thus, at high energies the variance is mainly driven by the scatter in the hard CR populations, which have been accelerated in strong shocks at higher redshifts.

(Lu et al. 2006). This violent formation epoch should have caused the CRs to be adiabatically compressed. In the further evolution, some cluster have been able to develop a cool core which additionally could have caused the CRs to be adiabatically contracted. On larger scales, the gas distribution follows that of dark matter (at least in the absence of violent merging events that could separate both components for time scales that are of order of the dynamical time). On these scales, the CR number density roughly traces the gas distribution (Pfrommer et al. 2008). Overall, we expect the spatial CR density profile relative to that of the gas density to scale with the cluster mass. If non-adiabatic CR transport processes have a sufficiently weak impact, these considerations would predict flatter \tilde{C} -profiles in larger halos as these halos are less concentrated.

Our goal is to characterize the trend of \tilde{C} -profiles with cluster mass and to test whether we can dissect a universal spatial CR profile. To this end, we adopt a phenomenological profile that allows for enough freedom to capture these features as accurately as possible. Hence, we parametrize $\tilde{C}(\mathbf{R})$ with shape parameters that include a flat central region given by C_{center} , a transition region where the location is denoted by R_{trans} and the steepness by β , and finally a flat outer region denoted by C_{vir} , through the equation

$$\tilde{C}_M(R) = (C_{\text{vir}} - C_{\text{center}}) \left(1 + \left(\frac{R}{R_{\text{trans}}} \right)^{-\beta} \right)^{-1} + C_{\text{center}}. \quad (22)$$

The core regions in our radiative simulations show too much cooling, and we possibly lack of important CR physics such as anisotropic CR diffusion that could smooth out any strong inhomogeneity at the center. Hence we adopt a conservative limit of the central profile value of $C_{\text{center}} = 5 \times 10^{-7}$.

In the top panel of Fig. 8 we show the mean of the \tilde{C}_M profiles from the cluster simulation sample. We subdivide our sample in two different mass intervals: large mass clusters (top red), and small mass clusters (bottom blue), in the mass range $1 \times 10^{15} < M_{\text{vir}}/M_{\odot} < 3 \times 10^{15}$, and $7 \times 10^{13} < M_{\text{vir}}/M_{\odot} < 4 \times 10^{14}$, respectively.⁹ The error-bars show the standard deviation from sample mean and the solid lines the best fit that will be discussed in more detail in Section 4.3. The \tilde{C}_M profile of our large mass clusters is almost flat and shows only a very weak radial dependence. In contrast, the \tilde{C} profile of our small clusters has a rather steep and long transition region and is increasing towards the center. The difference in normalization, transition width, and transition radius between low mass and large mass clusters indeed suggests that \tilde{C}_M scales with the cluster mass in a way that we anticipated. We quantify the mass scaling of these shape parameters by a power-law fit to the small and large clusters in the three lower panels of Fig. 8: the value of \tilde{C}_M in the asymptotically flat regime in the cluster periphery, C_{vir} (top); the transition radius, R_{trans} (middle); and the steepness of the transition, β (bottom). As expected, we find that all three quantities increase slowly with mass. We additionally show the values of \tilde{C}_M at R_{vir} for each cluster (black crosses). Within the scatter, these values are consistent with the mass scaling found by the profile fits in our two cluster mass bins. We have shown that there exists an *almost universal spatial CR profile* after taking into account the weak trends of the \tilde{C} profile with cluster mass. Note that the particle-by-particle variance of the spatial CR profile within a cluster (that we address in Section A3 in the appendix) additionally supports the conclusion of a universal spatial CR profile.

⁹ Note that we exclude the intermediate mass cluster g1d, since it had a very recent merger which resulted in a double-cored system with a non-spherical CR profile.

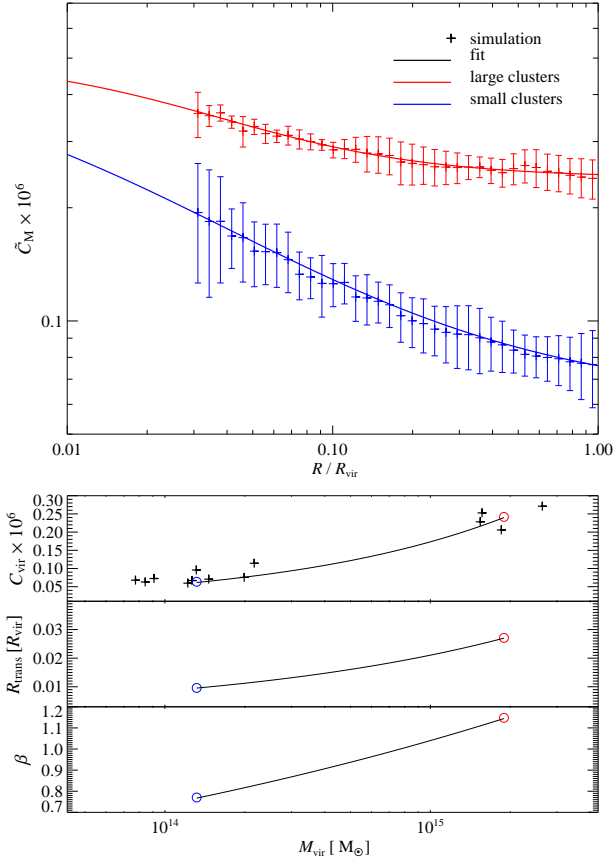


Figure 8. The top panel shows the profile of the dimensionless normalization of the CR spectrum, \tilde{C}_M . We show the mean \tilde{C}_M and the standard deviation across our cluster sample which has been subdivided into two different mass intervals: large- (red), and low-mass clusters (blue) representing the mass range $1 \times 10^{15} < M_{\text{vir}}/M_{\odot} < 3 \times 10^{15}$, and $7 \times 10^{13} < M_{\text{vir}}/M_{\odot} < 4 \times 10^{14}$. The solid lines show the best fit to equation (22). The lower three panels show the mass dependence of the quantities which parametrize \tilde{C}_M for low mass clusters (blue circles) and large mass clusters (red circles). The top small panel shows the asymptotic \tilde{C}_M for large radii (C_{vir}), where each cross shows \tilde{C}_M at R_{vir} for each cluster. The middle panel shows the transition radius R_{trans} , and the bottom panel shows the inverse transition width denoted by β .

4.3 A semi-analytic model for the spatial and spectral CR distribution

In our simulations we use a CR spectral description which follows five different CR proton populations; each being represented by a single power-law. The CR populations are chosen such that we accurately can capture the total CR spectrum in the entire momentum space (a convergence study on the number of CR populations is presented in the appendix A2). We want to model this spectrum analytically with as few CR populations as possible, but at the same time preserve the functional form of a power-law of each population. In that way we can easily obtain the total CR spectrum by superposition and apply a simple analytic formula to estimate the induced radiative processes.

In detail, we use a total CR proton spectrum $f_v(p, R)$ that is obtained by summing over the individual CR populations f_i (equation 2); each being a power-law in particle momentum with the total

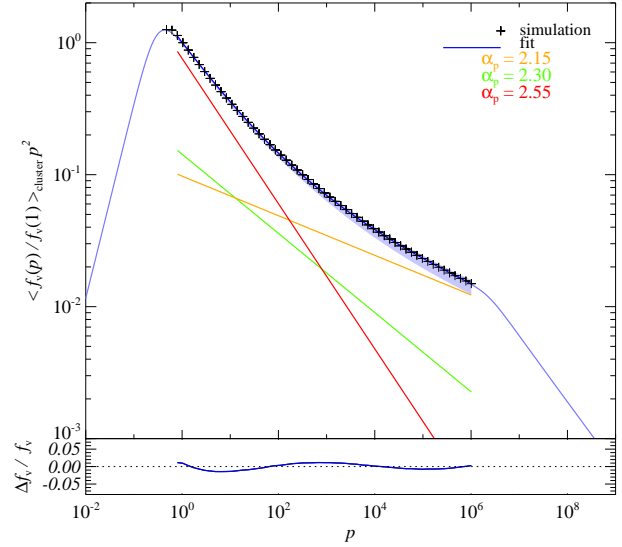


Figure 9. Cosmic ray proton spectrum as a function of dimensionless CR momentum $p = P_p/m_p c$ for our sample of 14 galaxy clusters (Table 1). The main panel shows median of the cosmic ray spectrum $f_v(p)p^2$ across our cluster sample. The spectrum of each cluster has been normalized at $p = 1$ (black crosses). The blue solid line shows the best fit triple power-law to the simulation data. The light blue area shows the 68 percentile of the data points across our cluster sample. The bottom panel shows the difference between the relative fit and the simulation data (blue solid line) which amounts to less than 2 percent.

CR amplitude $C_v(R)$,

$$f_v(p, R) = C_v(R) g(\zeta_{p,\text{max}}) D_p(p, p_{\text{break}}, q) \sum_i \Delta_i p^{-\alpha_i}, \quad (23)$$

where we assume universal spectral shape throughout the cluster. The normalization of f_v depends on maximum shock acceleration efficiency $\zeta_{p,\text{max}}$, where $g(0.5) = 1$ and $g(\zeta_{p,\text{max}} < 0.5) < 1$ (functional will be studied in Pfrommer in prep.). Denoting the amplitude of each CR population by $c_i(R)$, where the number of spectral bins might be different from the five chosen in the simulations, we construct the relative normalization for each CR population

$$\Delta_i \simeq \frac{c_i(R)}{C_v(R)}. \quad (24)$$

Here we have assumed that $c_i(R)/C_v(R)$ is only a weak function of radius. This is explicitly shown in Fig. 7, where the functional form is almost independent of the radius. The two energy breaks in the CR spectrum are represented by

$$D_p(p, p_{\text{break}}, q) = \left[\frac{1 + q^\beta}{1 + \left(\frac{p}{q}\right)^{-\beta}} \right]^{\frac{2}{\beta}} \left[\frac{1 + p_{\text{break}}^{-\beta}}{1 + \left(\frac{p}{p_{\text{break}}}\right)^{-\beta}} \right]^{\frac{\delta}{\beta}}. \quad (25)$$

The first term in equation (25) ensures the low-momentum slope $\sim p^2$ as appropriate from the phase space volume that is populated by CRs (Enblin et al. 2007) and the last term accounts for diffusive losses of CRs that steepen the spectrum by $\delta = 1/3$ assuming Kolmogorov turbulence. The shape parameter β determines the size of the transition in momentum space. Our choice of $\beta = 3$ ensures a fast transition from one regime to the other. The low-momentum break q is determined to $q \simeq 0.3$ from Fig. 9, and the high-momentum break p_{break} is derived from equation (3).

To capture the spectral universality of our cluster sample, we fit in Fig. 9 the median of our cluster sample of the CR spec-

trum with a triple power-law function. Because we normalize the spectrum at $p = 1$, this ensures that the normalized spectrum $f_s(p, R)/f_s(1, R) = \sum_i \Delta_i p^{-\alpha_i}$ becomes independent of radius (cf. equation 23). The triple power-law fit represented by the blue line in the upper panel of Fig. 9 resulted in

$$\Lambda = (0.767, 0.143, 0.0975), \text{ and } \alpha = (2.55, 2.3, 2.15). \quad (26)$$

The data from the simulation is denoted by black crosses, together with the 68 percentiles spread shown by the light blue area. In the lower panel, we show the relative difference between the simulation and the fit which indicates a difference of less than two percent from the GeV to PeV energy regime.

The spatial part of the CR spectrum is derived from the fit to the mean \tilde{C}_M in the top panel of Fig. 8. The solid lines show the best fit to \tilde{C}_M using equation (22). We find that the central value $C_{\text{center}} = 5 \times 10^{-7}$ is the most conservative value that still provides a good fit for both mass intervals. Note that there is a large uncertainty in this value due to insufficient data in the center¹⁰, implying that it should be treated as a lower limit. However, the gamma-ray flux depends only weakly on the exact value of C_{center} since most of the flux reside from the region outside the transition region. The mass dependence of \tilde{C}_M is quantified in the three lower panels of Fig. 8, where we fit a power-law in mass for the normalization C_{vir} (top), the transition radius R_{trans} (middle), and the steepness of the transition region β (bottom). We obtain the following relations,

$$C_{\text{vir}} = 1.7 \times 10^{-7} \times (M_{\text{vir}}/10^{15} M_{\odot})^{0.51}, \quad (27)$$

$$R_{\text{trans}} = 0.021 R_{\text{vir}} \times (M_{\text{vir}}/10^{15} M_{\odot})^{0.39}, \quad (28)$$

$$\beta = 1.04 \times (M_{\text{vir}}/10^{15} M_{\odot})^{0.15}. \quad (29)$$

5 SEMI-ANALYTIC MODEL FOR THE γ -RAY EMISSION

In this section we derive a semi-analytic formula for the integrated γ -ray source function that is based on our semi-analytic CR distribution. Using the gas density profile of the cluster along with its virial radius and mass, this formula enables us to predict the dominating π^0 -decay induced γ -ray emission from that cluster. The density profiles can either be inferred from simulations or from X-ray data. To test the semi-analytic source function, we use density profiles from our cluster simulations. We also make γ -ray flux predictions for the Coma and Perseus cluster using their true density profiles as inferred from X-ray observations.

5.1 Schematic overview and semi-analytic formulae

In Fig. 10 we show a schematic overview of the simulated CR spectrum and the integrated source function together with the mapping to our semi-analytic model. From the cluster simulations we derive the CR spectrum $f(p, \mathbf{R})$ describing the phase space density of CRs. When taking the spherical (volume weighted) average of $f(p, \mathbf{R})$, we obtain $f_s(p, R)$. We fit the spectral and spatial part of this function separately. The semi-analytic model for the CR distribution in clusters that we provide in equation (23) can now be used to predict the secondary radio synchrotron emission and the hadronically

¹⁰ We cut the \tilde{C}_M profiles at $R \approx 0.03R_{\text{vir}}$ due to the bias with the overcooled center. The increased scatter in the center for the small clusters is caused by the low statistics of the fewer number of clusters that can contribute on these small scales. With both of these considerations in mind, we conclude that there is a large scatter in C_{center} .

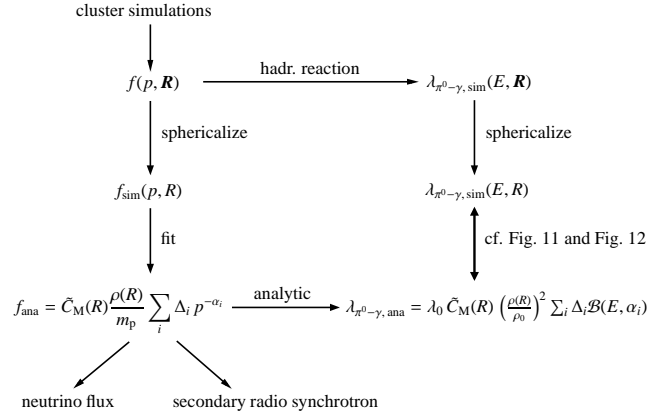


Figure 10. Schematic overview of how our semi-analytic framework relates to the simulated CR and γ -ray quantities. From the cluster simulations we derive the CR spectrum for each SPH particle, $f(p, \mathbf{R})$. Going clockwise, the integrated γ -ray production rate for each SPH particle $\lambda_{\pi^0-\gamma,\text{sim}}(E, \mathbf{R})$ is derived within the framework of Pfrommer et al. (2008). The radial profile of the integrated γ -ray production rate, $\lambda_{\pi^0-\gamma,\text{sim}}(E, R)$, is obtained by volume weighting this quantity of individual SPH particles. Returning to $f(p, \mathbf{R})$ and going counter-clockwise instead, we can directly perform a volume-weighting of the CR spectrum in each radial bin, yielding $f_{\text{sim}}(p, R)$. Fitting both the spatial and spectral part provides us with a semi-analytic model for the spectrum, f_{ana} . The semi-analytic model for the integrated γ -ray production rate, $\lambda_{\pi^0-\gamma,\text{ana}}$, is derived within the framework of Pfrommer et al. (2008). The explicit form of $\lambda_{\pi^0-\gamma,\text{ana}}$ can be found in equations (30)-(34), while λ_0 and $\mathcal{B}(E, \alpha_i)$ are implicitly given by equation (32). Comparing the flux from the simulations and our semi-analytic model shows good agreement for our cluster sample.

induced neutrino and γ -ray emission from galaxy clusters. Following the formalism in Pfrommer et al. (2008), we obtain the volume weighted and energy integrated and omnidirectional (i.e. integrated over the 4π solid angle) γ -ray source function due to pion decay¹¹,

$$\lambda_{\pi^0-\gamma}(R, E) = A_\lambda(R) \tilde{\lambda}_{\pi^0-\gamma}(E), \quad (30)$$

$$A_\lambda(R) = \tilde{C}_M(R) \frac{\rho(R)^2}{\rho_0^2}, \quad (31)$$

$$\begin{aligned} \tilde{\lambda}_{\pi^0-\gamma}(E) &= g(\zeta_{\text{p,max}}) D_\gamma(E_\gamma, E_{\gamma,\text{break}}) \frac{4m_{\pi^0}c}{3m_p^3} \rho_0^2 \\ &\times \sum_{i=1}^3 \frac{\sigma_{\text{pp},i}}{\alpha_i \delta_i} \left(\frac{m_p}{2m_{\pi^0}} \right)^{\alpha_i} \Delta_i \left[\mathcal{B}_x \left(\frac{\alpha_i + 1}{2\delta_i}, \frac{\alpha_i - 1}{2\delta_i} \right) \right]_{x_1}^{x_2}, \\ \text{and } x_j &= \left[1 + \left(\frac{m_{\pi^0}c^2}{2E_{\gamma,j}} \right)^{2\delta_i} \right]^{-1}, \end{aligned} \quad (32)$$

where the sum extends over our three CR populations, $\tilde{C}_M(R)$ is given by equations (22), (27) - (29), while Λ and α are provided by equation (26) and we introduced an auxiliary variable ρ_0 for dimensional reasons to ensure that A_λ is dimensionless. In equation (32) we have also introduced the abbreviation

$$[\mathcal{B}_x(a, b)]_{x_1}^{x_2} = \mathcal{B}_{x_2}(a, b) - \mathcal{B}_{x_1}(a, b), \quad (33)$$

where $\mathcal{B}_x(a, b)$ denotes the incomplete Beta-function, we have used that the number density of target nucleons is the sum of hydrogen n_{H} and helium n_{He} number densities, $n_{\text{N}} = n_{\text{H}} + 4n_{\text{He}} = \rho/m_p$. The shape parameter $\delta_i \approx 0.14 \alpha_i^{-1.6} + 0.44$ allows us to accurately

¹¹ From here on we always imply the volume weighted and energy integrated source function when talking about λ if nothing else is stated.

predict the emission close to the pion bump in combination with the effective inelastic cross-section for proton-proton interactions, $\sigma_{pp,i} \simeq 32 (0.96 + e^{4.42-2.4\alpha_i})$ mbarn. In addition we have a term, similar to equation (25) that describes the diffusive CR losses due to escaping protons from the cluster at the equivalent photon energy for the break, $E_{\gamma, \text{break}}$. It is derived from $E_{p, \text{break}}$ of equation (3),

$$D_{\gamma}(E_{\gamma}, E_{\gamma, \text{break}}) = \left[1 + \left(\frac{E_{\gamma}}{E_{\gamma, \text{break}}} \right)^{\beta-1/(3\beta)} \right], \quad (34)$$

where $\beta = 3$. Finally we note that the semi-analytic γ -ray model is derived within R_{vir} . Applying the model to the region outside R_{vir} , but within $3R_{\text{vir}}$, would increase the γ -ray flux by less than 10% for small mass clusters and less than 30% for large mass clusters (cf. Table 5).

For convenience and completeness, we provide here the differential γ -ray source function for pion decay (for further details see Pfrommer & Enßlin 2004),

$$s_{\pi^0-\gamma}(R, E) = A_s(R) \tilde{s}_{\pi^0-\gamma}(E), \quad (35)$$

$$\begin{aligned} \tilde{s}_{\pi^0-\gamma}(E) &= g(\zeta_{p, \text{max}}) D_{\gamma}(E_{\gamma}, E_{\gamma, \text{break}}) \frac{16}{3m_p^3 c} \rho_0^2 \\ &\times \sum_{i=1}^3 \frac{\sigma_{pp,i}}{\alpha_i} \left(\frac{m_p}{2m_{\pi^0}} \right)^{\alpha_i} \Delta_i \left[\left(\frac{2E_{\gamma}}{m_{\pi^0} c^2} \right)^{\delta_i} + \left(\frac{2E_{\gamma}}{m_{\pi^0} c^2} \right)^{-\delta_i} \right]^{\frac{\alpha_i}{\delta_i}} \end{aligned} \quad (36)$$

where $A_s(R) = A_i(R)$ (see equation 31). The exact shape of $D_{\gamma}(E_{\gamma}, E_{\gamma, \text{break}})$ depends on the detailed physics of CR diffusion and the characteristics of turbulence and is subject to future studies. We note, however, that the break does not interfere with the energy range of current γ -ray observatories.

5.2 Comparing our semi-analytic model to simulations

To test our semi-analytic γ -ray model we contrast it with numerically calculated radial profiles and spectra. In the upper panel of Fig. 11, we compare the radial profile of our semi-analytic γ -ray source function (equation 30) at 100 MeV to a numerical emission profile for two representative clusters, a large post-merging cluster g72a, and a small CC cluster g914. The numerical profile has been obtained by means of calculating the γ -ray source function $\lambda_{\pi^0-\gamma}$ of every SPH particle and volume weighting the resulting radial profile. The overall shape of the radial profiles of $\lambda_{\pi^0-\gamma}$ for different clusters are quite similar. This is because the main spatial dependence originates from the gas density, that enters with a square in $\lambda_{\pi^0-\gamma}$ and has a small scatter across the cluster sample. The different behavior in the cluster centers stems from the steeper profile of $\tilde{C}_M(R)$ for low mass clusters. We show the difference between the integrated source functions from our simulations and the semi-analytic model in more detail in the lower panel of Fig. 11. In both clusters, we see an excellent agreement with differences amounting to less than 20-30 percent at any radius. These differences are representative for our cluster sample, which is indicated by the median difference across our cluster sample together with the 68 percentiles that show a spread similar to the difference in these two clusters. Since these are fluctuating differences, they average partly away when we perform the volume integral. Hence we obtain an agreement of the total flux within the virial radius – obtained directly from the simulations and in our semi-analytic model – that is better than 5 per cent for the two representative clusters that are shown. This indicates that our semi-analytic description manages to capture the CR physics, that is important for γ -ray emission from clusters, surprisingly well.

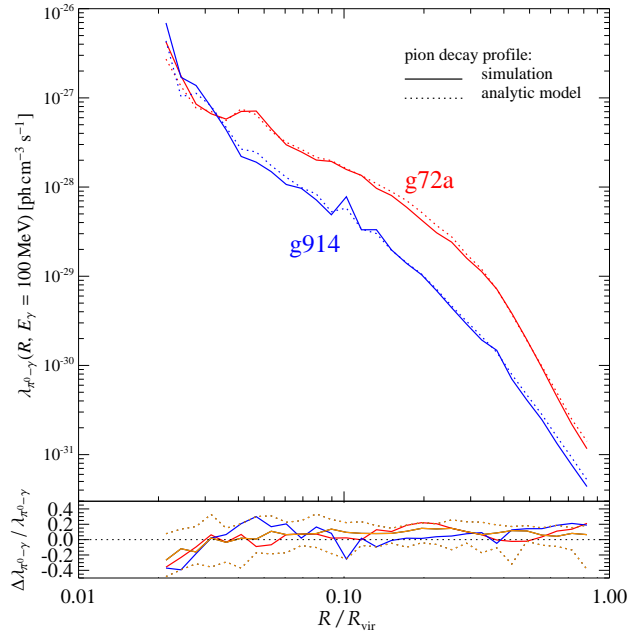


Figure 11. Comparison of the spatial profile of the γ -ray source function in our simulations and our semi-analytic framework. The main panel shows the profile of the γ -ray source function $\lambda_{\pi^0-\gamma}$ that results from pion decay emission. We compare $\lambda_{\pi^0-\gamma}$ at 100 MeV for two clusters, the large merging g72a (red) cluster and the small CC g914 (blue) cluster, both as a function of R/R_{vir} . The solid lines show the simulated integrated source function and the dotted lines the semi-analytic model. The lower panel shows the difference between the semi-analytic and the simulated source functions normalized by the simulated source function. The orange lines show the median (solid) difference between the semi-analytic and the simulated source functions across our cluster sample together with the 68 percentiles (dotted).

We show the γ -ray spectrum of the π^0 -decay emission weighted by energy for g72a and g914 in the upper panel of Fig. 12. Both clusters have very similar spectra with the exception of the diffusive steepening that is inherited from the proton spectrum. Since the break of the proton spectrum scales as $E_{p, \text{break}} \propto M_{\text{vir}}^2$ with the virial mass of the cluster (equation 3), the break in the pion decay spectrum is reduced by a factor of 10^3 for the smaller cluster g914. The solid and dotted lines contrast the simulated spectrum to that obtained from our semi-analytic model. The difference between these two approaches amounts to less than 20 percent for both clusters in the GeV and TeV band (shown in the lower panel). The flux differences between our semi-analytic model and the simulations for individual clusters are about a factor two smaller compared to the scatter in the mass-luminosity scaling relations for a given cluster (see e.g. Fig. 15). The reason for the more accurate predictions within our semi-analytic formalism is a direct consequence of the essential additional spatial information of the gas and CR density that we account for.

5.3 Predicting the γ -ray emission from Perseus and Coma

Here we demonstrate how our semi-analytic formalism can be applied to predict the γ -ray flux and surface brightness from real clusters using their electron density profile as inferred from X-ray measurements. The predicted flux and surface brightness are then compared to current upper limits and previous work.

The two clusters that we investigate are two of the

Table 3. Properties of the Coma and Perseus galaxy cluster.

cluster	$z^{(1)}$	$D_{\text{lum}}^{(1)}$ [Mpc]	$R_{\text{vir}}^{(1)}$ [Mpc]	$M_{\text{vir}}^{(1)}$ [$10^{14} M_{\odot}$]	$L_{X,0.1-2.4}^{(1)}$ [$10^{44} \text{ erg s}^{-1}$]	$n_e^{(1)}$ [$10^{-3} \text{ electrons cm}^{-3}$]
Coma	0.0232	101	2.3	13.8	4.0	$3.4 \times [1 + (R/294 \text{ kpc})^2]^{-1.125}$
Perseus	0.0183	77.7	1.9	7.71	8.3	$46 \times [1 + (R/57 \text{ kpc})^2]^{-1.8} + 4.79 \times [1 + (R/200 \text{ kpc})^2]^{-0.87}$

Notes:

(1) Data for redshift (z), luminosity distance (D_{lum}), R_{vir} , M_{vir} , and X-ray 0.1-2.4 keV luminosity ($L_{X,0.1-2.4}$) are taken from Reiprich & Böhringer (2002) and rescaled to our assumed cosmology (Section 2.1). The electron number density, n_e , for Coma and Perseus are inferred from X-ray observations by Briel et al. (1992) and Churazov et al. (2003), respectively.

Table 4. γ -ray flux comparison of the Coma and Perseus galaxy cluster.

		E_{γ} [GeV]	Experiment	θ [deg]	$\mathcal{F}_{\gamma, \text{UL}}(> E_{\gamma})$ [$\text{ph cm}^{-2} \text{ s}^{-1}$]	$\mathcal{F}_{\pi^0-\gamma}(> E_{\gamma}, \zeta_{\text{p,max}}^{(5)})$ [$\text{ph cm}^{-2} \text{ s}^{-1}$]	$\frac{\mathcal{F}_{\gamma, \text{UL}}(> E_{\gamma})}{\mathcal{F}_{\pi^0-\gamma}(> E_{\gamma}, \zeta_{\text{p,max}})}$
GeV-regime	Coma	100 MeV	EGRET ⁽¹⁾	5.8 ⁽⁴⁾	3.81×10^{-8}	4.20×10^{-9}	9.1
	Perseus	100 MeV	EGRET ⁽¹⁾	5.8 ⁽⁴⁾	3.7×10^{-8}	1.46×10^{-8}	2.5
TeV-regime	Coma	1 TeV	HESS ⁽²⁾	0.2	1.1×10^{-12}	4.86×10^{-14}	23.0
	Perseus	1 TeV	MAGIC ⁽³⁾	0.15	4.7×10^{-13}	1.75×10^{-13}	2.7
	Perseus	100 GeV	MAGIC ⁽³⁾	0.15	6.55×10^{-12}	3.2×10^{-12}	2.0

Notes:

(1) Reimer et al. (2003), (2) Aharonian et al. (2009), (3) Aleksić et al. (2010), (4) Since the flux is dominated by the region inside R_{vir} we use $R_{\theta} = R_{\text{vir}}$. (5) γ -ray fluxes are obtained within our semi-analytic model that is based on our conservative model. The γ -ray flux level depends on the maximum shock acceleration efficiency of CRs, $\zeta_{\text{p,max}}$, for which we assume an optimistic value of 0.5. Smaller efficiencies imply smaller fluxes.

brightest X-ray clusters in the extended HIFLUGCS catalogue (Reiprich & Böhringer 2002) – a sample of the brightest X-ray clusters observed by ROSAT – namely Coma and Perseus. Both Coma and Perseus are well studied clusters, where Coma is a large post-merging cluster while Perseus is a somewhat smaller cluster that hosts a massive cooling flow and is the brightest X-ray cluster known (Edge et al. 1992). In Table 3 we show the data for respective cluster. Using the electron number density profile, we can calculate the gas density profile of the cluster through $\rho = m_p n_e / (X_H X_e)$. Here denote $X_H = 0.76$ the primordial hydrogen (H) mass fraction, and the ratio of electron and hydrogen number densities in the fully ionized ICM is given by $X_e = 1.157$. For sufficiently small angular scales, the γ -ray flux within the radius $R_{\theta} = \theta D_{\text{lum}}$ of a disk of angular radius θ (measured in radians and centered at $R = 0$) is calculated by

$$\mathcal{F}_{\pi^0-\gamma}(> E_{\gamma}) = \frac{1}{D_{\text{lum}}^2} \int_0^{R_{\theta}} 2\pi dR_{\perp} R_{\perp} S_{\pi^0-\gamma}(R_{\perp}, E_{\gamma}), \quad (37)$$

$$S_{\pi^0-\gamma}(R_{\perp}, E_{\gamma}) = 2 \frac{\tilde{\lambda}_{\pi^0-\gamma}(E_{\gamma})}{4\pi} \int_{R_{\perp}}^{\infty} dR \frac{\rho^2(R)}{\rho_0^2} \frac{\tilde{C}_M(R) R}{\sqrt{R^2 - R_{\perp}^2}}, \quad (38)$$

where $\tilde{\lambda}_{\pi^0-\gamma}(E_{\gamma})$ is given by equation (32) and we introduced the definition for the γ -ray surface brightness $S_{\pi^0-\gamma}$ in the last step. As a consistency check, we compare the flux ratios from X-rays $\mathcal{F}_{X\text{-ray,Perseus}}/\mathcal{F}_{X\text{-ray,Coma}} \approx 3.51$ to that of γ -rays as predicted by our semi-analytic model, $\mathcal{F}_{\pi^0-\gamma, \text{Perseus}}(> 100 \text{ MeV})/\mathcal{F}_{\pi^0-\gamma, \text{Coma}}(> 100 \text{ MeV}) \approx 3.47$ and find excellent agreement within one percent.

5.3.1 Comparison to upper limits in the GeV/TeV regime

We calculate the γ -ray fluxes for Coma and Perseus above 100 MeV and 100 GeV that is emitted within $R_{\theta} = R_{\text{vir}}$ (see Table 4). Comparing the 100 MeV-flux in our model to the EGRET upper limit on the Coma (Perseus) cluster (Reimer et al. 2003), we find that it falls short of our semi-analytic prediction by a factor of about 9 (2.5). With the two-year data by Fermi, this upper limit on Coma will improve considerably and is expected to become competitive with our predictions. With this at hand, we will be able to put important constraints on the adopted CR physics in our simulations. In particular, we can test our assumptions about the maximum shock acceleration efficiency at structure formation shocks. Since Fermi detected γ -rays from the central cD galaxy in Perseus, NGC1275, at a level that is about five times higher than the EGRET upper limits, this indicates that the source is variable on time scales of years to decades (Abdo et al. 2009). Hence it restricts and complicates the detectability of the extended pion-decay emission that might be buried underneath.

In the TeV regime, we integrate our model prediction within a solid angle that is comparable to the point-spread function of IACTs. The best current upper limit for Coma (Aharonian et al. 2009) falls short of our semi-analytic prediction by a factor 20. The best current upper flux limit for Perseus (using a spectral index of -2.2, Aleksić et al. 2010) is only a factor of two larger than our flux prediction and clearly within reach of future deeper TeV observations. This demonstrates the huge potential of nearby CC clusters to detect non-thermal γ -ray emission as suggested by Pfrommer & Enßlin (2004).

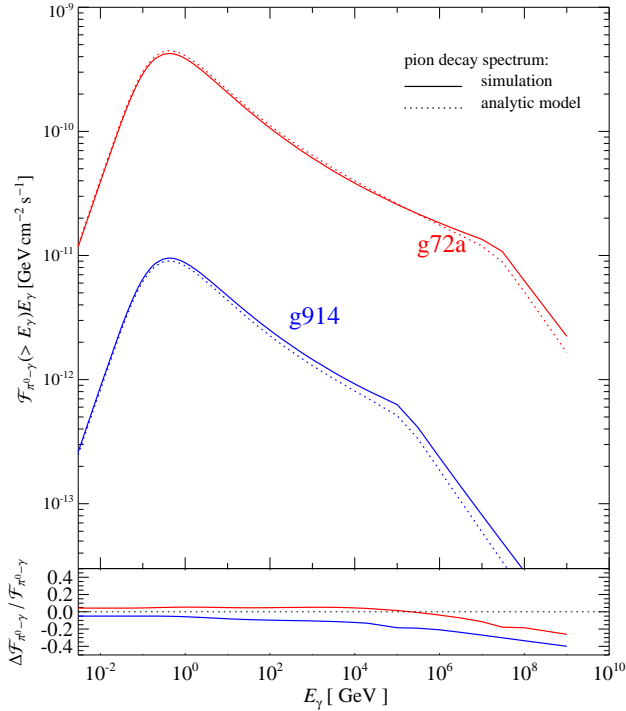


Figure 12. Comparison of the γ -ray spectrum in our simulations and our semi-analytic framework. The main panel shows the γ -ray number flux from pion decay weighted by the photon energy. We compare two clusters, the large merging g72a (red) cluster and the small CC g914 (blue) cluster, both as a function of photon energy. The solid lines show the simulated flux and the dotted lines show the semi-analytic model. The lower panel shows the difference between the semi-analytic and the simulated flux normalized by the simulated flux.

5.3.2 Surface brightness profile

To explain the large difference in flux between Coma and Perseus we show the surface brightness as a function of the viewing angle θ in Fig. 13. The dense cooling core region of Perseus provides ample target material for two-body interactions such as bremsstrahlung or hadronic CR interactions which boosts the luminosities likewise. This results in a large increase in flux compared to the average cluster of similar mass that are characterized by mass-luminosity scaling relations (see e.g. Table 5). Assigning a flux to a cluster that is consistent with the scaling relations should be a very conservative approach for CC clusters. The half flux radius for Perseus (Coma) is $\theta_{\text{HF}} = 0.11$ deg (0.18 deg). It is shown with dotted lines in Fig. 13. Since these θ_{HF} values are comparable to the angular scale of the point spread functions of IACTs (0.1-0.2 degrees) both clusters are suitable candidate sources. The dashed and dotted-dashed lines are obtained by using the semi-analytic formalism from Kushnir & Waxman (2009) to predict the surface brightness from the Coma cluster above the energy 100 MeV and 100 GeV, respectively. See Section 8.1 for a detailed comparison to their result.

5.4 CR-to-thermal pressure and temperature profile in Perseus and Coma

A quantity that is of great theoretical interest is the CR pressure relative to the thermal pressure, $X_{\text{CR}} = P_{\text{CR}}/P_{\text{th}}$ as it directly assesses the CR bias of hydrostatic cluster masses where the CR pressure en-

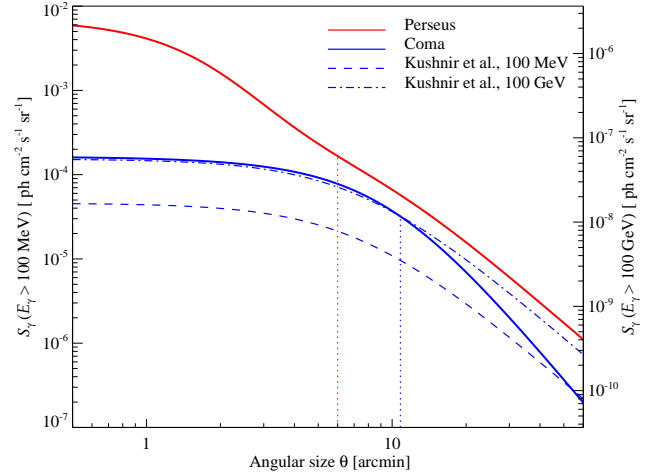


Figure 13. The γ -ray brightness profiles derived with our semi-analytic formalism (solid line) as a function of the angular size on the sky θ . The left axis indicates the emission for $E_\gamma > 100$ MeV, and the right axis shows the emission for $E_\gamma > 100$ GeV. We compare the emission from the Perseus galaxy cluster (red solid line) to the Coma galaxy cluster (blue solid line) while employing the X-ray density profile for each cluster, respectively. The high surface brightness in the cool core cluster Perseus is a result of the high central gas densities in this cluster. The dotted line shows the radius from within half the flux originates. It is clearly smaller for Perseus due to the steep central density profile and the larger transition region in \tilde{C}_M for smaller clusters. The dashed and dash-dotted lines show the Coma surface brightness as predicted from Kushnir & Waxman (2009) using their assumed parameters above the energy 100 MeV and 100 GeV, respectively.

ters in the equation of motion. Since $X_{\text{CR}} \propto n_{\text{th}}/P_{\text{th}} = 1/kT$ in the external cluster regions, we have to accurately model the temperature profile of our clusters. Note, however, that this relation should only hold for regions with long thermal cooling times compared to the dynamical time scale. In particular it breaks down towards the center of a cooling flow cluster where the thermal gas cools on a shorter time scale such that the forming cooling flow causes adiabatic contraction of the CR population. We model the central regions of Coma and Perseus according to X-ray observations by Briel et al. (1992) and Churazov et al. (2003), respectively. These observations are not sensitive to the outer temperature profile due to the high particle background for XMM-Newton and Chandra.¹² X-ray observations of somewhat more distant cluster sample show a universal declining temperature profile outside the cooling core region up to R_{500} (Vikhlinin et al. 2005). We model this behavior of the temperature profiles towards the cluster periphery according to cosmological cluster simulations by Pfrommer et al. (2007) and obtain a function $\mathcal{T}_{\text{ext}}(R)$ that accounts for the decreasing temperature profile outside the core region. It is unity in the center and then smoothly decreases until the virial radius beyond which we expect the spherical approximation to break down and where the cluster accretion shocks should introduce breaks in the temperature profile.¹³ This function can be multiplied to existing central

¹² We note that Suzaku has an approximately ten times lower background due to its low-Earth orbit that could enable such observations in the X-rays. Alternatively, combining the X-ray surface brightness with future Sunyaev-Zel'dovich measurements of these nearby clusters should in principle allow the derivation of the temperature profile of the entire cluster.

¹³ The mean temperature profile of the radiative simulations by Pfrommer et al. (2007) increases towards smaller radii until $R \sim 0.1R_{\text{vir}}$

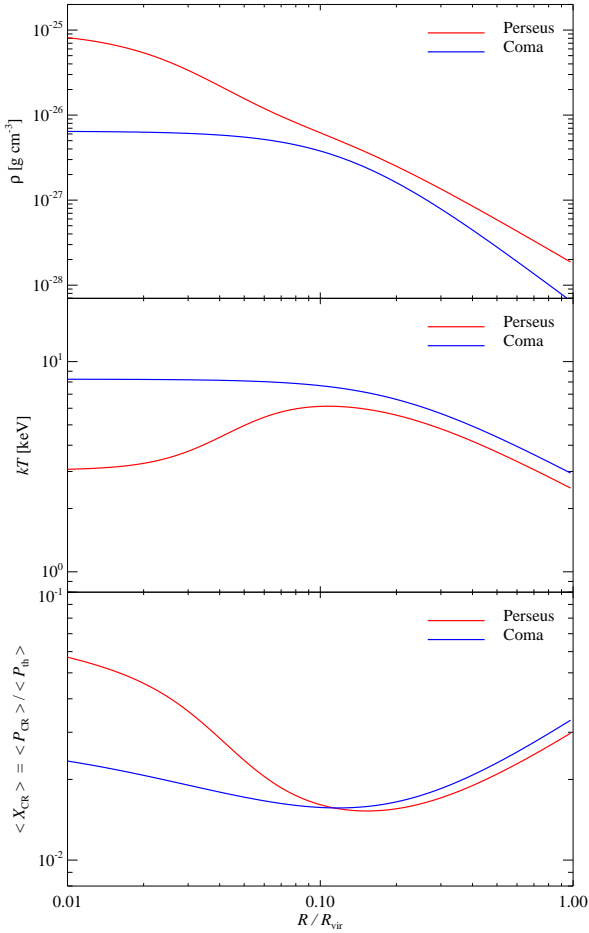


Figure 14. Radial profiles of the gas density ρ , the temperature kT , and the CR-to-thermal pressure $\langle X_{\text{CR}} \rangle = \langle P_{\text{CR}} \rangle / \langle P_{\text{th}} \rangle$. We compare the cool core cluster Perseus (red) to the non-cool core cluster Coma (blue). The density and temperature profiles are taken from the X-ray data (Churazov et al. 2003; Briel et al. 1992) while we remodel the external temperature profile to bring it into agreement with cosmological cluster simulations as well as higher redshift X-ray observations. We obtain the CR-to-thermal pressure profile from our semi-analytic modeling in combinations with the presented gas profiles.

temperature profiles to yield the temperature profiles for Coma and Perseus,

$$kT_{\text{Perseus}}(R) = 7 \text{ keV} \times \frac{1 + (R/71 \text{ kpc})^3}{2.3 + (R/71 \text{ kpc})^3} \mathcal{T}_{\text{ext}}(R), \quad (39)$$

$$kT_{\text{Coma}}(R) = 8.25 \text{ keV} \times \mathcal{T}_{\text{ext}}(R), \quad (40)$$

$$\mathcal{T}_{\text{ext}}(R) = \left[1 + \left(\frac{R}{0.2 R_{\text{vir}}} \right)^2 \right]^{-0.32}, \quad (41)$$

due to adiabatic compression of the gas and starts to drop sharply towards smaller radii where radiative cooling causes the temperature to decline. This behavior qualitatively matches the results of low mass clusters from a Chandra sample of nearby relaxed galaxy clusters (Vikhlinin et al. 2006) whereas the temperature maximum for more massive clusters seems to shift to somewhat larger radii around $R \sim 0.2 R_{\text{vir}}$. Hence we adopted this larger value as the transition radius for Perseus and Coma. We note that the resulting profiles are consistent with the observed central temperature profiles (Briel et al. 2001; Churazov et al. 2003) as well as the mosaiced entire temperature profile of Perseus beyond R_{200} (S. Allen, private communication).

where R_{vir} can be obtained from Table 3. The density and temperature profiles for Coma and Perseus are shown in the first two panels of Fig. 14.

In the previous sections, we have seen that the γ -ray surface brightness is a radially declining function and so is the CR pressure. In contrast, outside the central cooling core regions, the CR-to-thermal pressure X_{CR} increases with radius as can be seen in the bottom panel of Fig. 14. This increase is entirely driven by the decreasing temperature profile. The two X_{CR} -profiles for Coma and Perseus show our expectations for a typical non-CC and CC cluster. The X_{CR} -profile in a CC cluster shows an additional enhancement towards the cluster center which results from the centrally enhanced CR number density due to adiabatic contraction during the formation of the cooling flow. During this process, the thermal gas cools on a short time scale compared to that of the CRs which causes an increase in density and hence adiabatic compression of the CRs. We note that the overall normalization of X_{CR} depends on the normalization of the CR distribution that itself is set by the maximum shock acceleration efficiency. The overall shape of X_{CR} , however, should remain invariant since CRs are adiabatically transported into the cluster (Pfrommer et al. 2007, Pfrommer in prep.).

While the overall characteristics of X_{CR} in our semi-analytical model is similar to that obtained in cosmological simulations (Pfrommer et al. 2007), there are some noticeable differences particularly in the central cooling core region around the cD galaxy of these clusters. Again this can be traced back to known shortcomings of modeling the physics in the central regions correctly in current simulations such as to include AGN feedback and anisotropic conduction in combination with magneto-hydrodynamics. This also leads to different simulated temperature profiles in the center compared to those inferred from X-ray observations and explains the discrepancy in the X_{CR} -profiles. The volume average of the CR-to-thermal pressure for Coma and Perseus is $\langle X_{\text{CR}} \rangle = \langle P_{\text{CR}} \rangle / \langle P_{\text{th}} \rangle = 0.02$, dominated by the region around the virial radius. These values assume an optimistic saturation value of the shock acceleration efficiency of $\zeta_{\text{max}} = 0.5$ and decrease accordingly if this value is not realized at the relevant structure formation shocks responsible for the CRs in clusters.

6 HIGH-ENERGY SCALING RELATIONS

We now discuss the scaling relations of the numerical γ -ray emission from clusters and analyze their dependence on dynamical state, emission region and address the bias of galaxies to the total luminosity. The cluster scaling relations are derived by integrating the surface brightness map of each cluster. By fitting the total γ -ray emission of the 14 clusters in our cluster sample with a power-law, we determine the mass-to-luminosity scaling.

In the preceding sections we have shown that the pion decay emission dominates the total γ -ray emission but we have not addressed the question, which radii contribute most to the luminosity? To answer this, we have to consider the γ -ray luminosity resulting from pion decay within a radius R ,

$$\mathcal{L}_{\pi^0-\gamma}(R) \propto \int_0^R dR' R'^2 \tilde{C}_M(R') \rho(R')^2 \sim \int_0^R dR' R'^2 \rho(R')^2. \quad (42)$$

For the purpose of this simple argument, we neglected the very weak spatial dependence of the CR distribution which is described by $\tilde{C}_M(R)$. The γ -ray luminosity $\mathcal{L}_{\pi^0-\gamma}$ is dominated by the region around the scale radius R_s which can be seen by considering the contribution to $\mathcal{L}_{\pi^0-\gamma}$ per logarithmic radius,

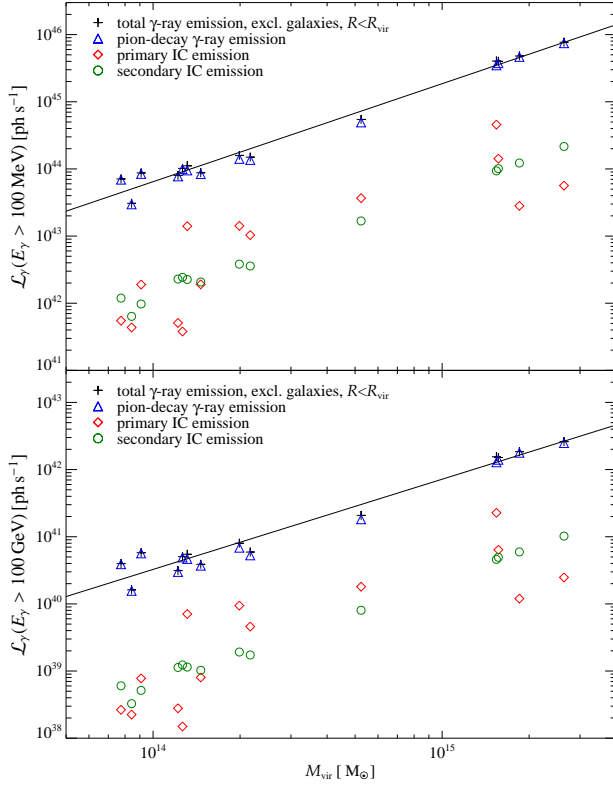


Figure 15. Cluster scaling relations of the γ -ray luminosity for the energy regimes corresponding to the *Fermi* γ -ray space telescope and imaging air Čerenkov telescopes. Show is the contribution from individual γ -ray emission components within one virial radius (pIC - red squares, sIC - green circles, π^0 decay - blue triangles) to the total cluster luminosities (black crosses) and mass to luminosity scaling (black solid line) at the energies $E_\gamma > 100$ MeV (upper panel) and $E_\gamma > 100$ GeV (lower panel).

$$\frac{d\mathcal{L}_{\pi^0-\gamma}}{d \log R} \propto R^3 \rho(R)^2 \propto \begin{cases} R^3 & R < R_s, \\ R^{-3} & R \gg R_s. \end{cases} \quad (43)$$

Here we assumed a central plateau of the density profile which steepens beyond the scale radius R_s and approaches the asymptotic slope of R^{-3} of the dark matter profile that shapes the gas distribution at large radii (Komatsu & Seljak 2001, and references therein). This radial behavior makes the simulated γ -ray luminosity only weakly dependent on uncertainties from the incomplete physical modelling of feedback processes in the cluster cores.

6.1 Contribution of different γ -ray emission processes

Figure 15 shows the scaling relations of the IC and pion decay emission for two different energy scales of interest to the *Fermi* γ -ray space telescope and imaging air Čerenkov telescopes. We compare the total emission and the contribution from the individual emission components of each cluster. The very similar slopes of the mass-to-luminosity scaling relation at both energies (Table 5) is a consequence of the small variance in the proton spectrum (Fig 6) among different galaxy clusters. The individual emission processes also show similar slopes, with small scatter for the pion decay emission and sIC component. Contrary, the pIC emission has a larger scatter than the secondary emission components due to the different dynamical states: the presence of strong merger or accretion shocks is critical for the generation of primary CR electrons and the associated radiative emission.

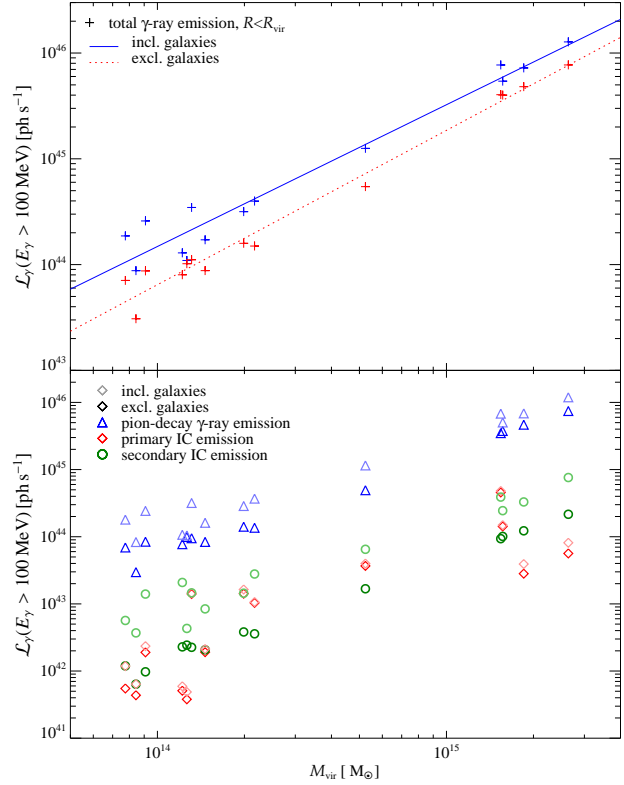


Figure 16. Studying the galaxy bias to cluster γ -ray scaling relations for energies $E_\gamma > 100$ MeV and $R < R_{\text{vir}}$. In the upper panel, the blue crosses show the cluster emission with galaxies and the red crosses show the cluster emission without galaxies, the solid lines show the mass to luminosity scaling (Table 5). The lower panel shows the contribution from individual components (primary IC – red squares, secondary IC – green circles, π^0 decay – blue triangles) for emission including galaxies (light color) and excluding galaxies (dark color).

The ratio of the pion decay to the pIC emission in the 100 MeV and 100 GeV regime is very similar. This is partly a coincidence and owed to our particular choice of the two energy bands: the effective spectral index of the pion decay between these two energies is flattened due to the pion bump. It happens to be similar to the power-law index of the pIC component which itself is unaffected by the energy cutoff of the electron spectrum at these energies. If we chose a smaller (larger) value than 100 MeV for the lower energy band, we would obtain a lower (higher) pion-to-pIC ratio due to the steeper intrinsic spectrum of the CR protons at lower energies (cf. Fig. 1).

6.2 γ -ray emission from individual galaxies

We investigate the bias of galaxies to the scaling relation of the γ -ray luminosity above 100 MeV in Fig. 16. The top panel shows the total γ -ray emission, where the presence of galaxies biases smaller mass clusters slightly more compared to their larger analogues, with an average bias of about a factor two across our cluster sample. Masking galaxies reduces the overall scatter in the scaling relations, particularly at low masses. In the lower panel, we show the contribution from individual emission components. The largest bias originates from the pion decay (blue triangles) and the sIC emission (green circles), while the pIC component (red diamonds)

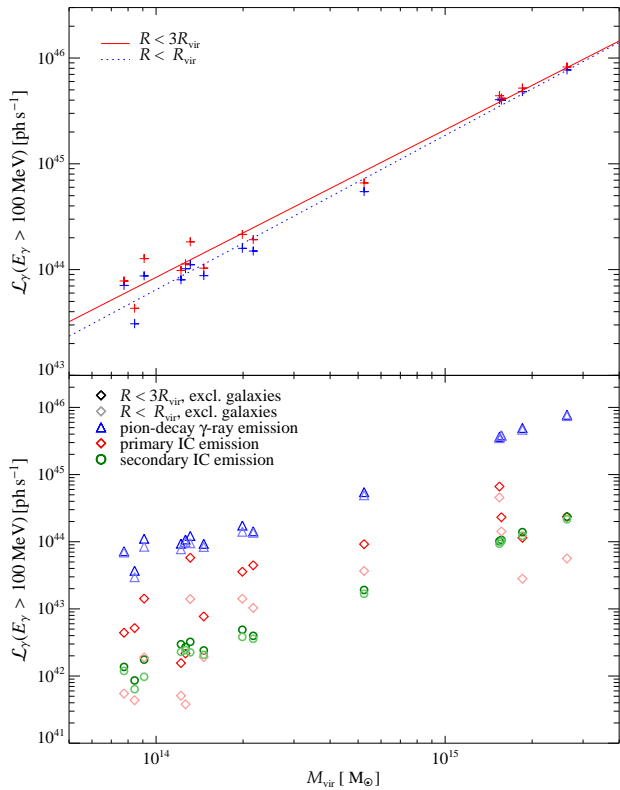


Figure 17. Influence of the emission from the accretion region around clusters on the mass to luminosity cluster scaling relations for $E_\gamma > 100$ MeV. In the upper panel, we show the luminosity integrated out to $3R_{\text{vir}}$ (red crosses) as well as the luminosity integrated out to R_{vir} (blue crosses). The solid lines indicate the mass to luminosity scaling relation found in Table 5. The lower panel shows the contribution from individual components (primary - red squares, secondary - green circles, π^0 decay - blue triangles) for luminosity integrated out to R_{vir} (light color) and luminosity integrated out to $3R_{\text{vir}}$ (dark color).

is barely affected by this masking procedure since it does not scale with density.

6.3 γ -ray emission from the cluster periphery and WHIM

In this section we study the dependence of the accretion region around clusters on γ -ray scaling relations. Specifically, we compare the total γ -ray emission within R_{vir} to the emission within $3R_{\text{vir}}$ which hosts the WHIM and individual satellite galaxies (and groups) that have not yet accreted onto the cluster.

From Fig. 17 it is clear that the total luminosity is dominated from the region inside R_{vir} . For small clusters, the flux-correction from the WHIM is of the order of 30 percent which the correction is smaller for massive systems – below 10 percent. This stems from the fact that the emission of low mass systems with smaller potential wells is easier to perturb – through accreting clumps of matter or nearby satellite systems. The pIC component contributes a factor 2 – 10 more in the WHIM than within R_{vir} . The reason being that especially for merging systems, the pIC profile is rather flat (see Fig. 4). Hence it contributes substantially to WHIM luminosity, whereas the density dependent secondary components in the WHIM are negligible due to the low gas densities. Only satellite systems within the WHIM contribute at a low level to the secondary components. This effect is especially pronounced when galaxies are

excluded and implies that the pIC component becomes comparable to the pion decay emission for a few low mass clusters. Note that in the TeV regime, the pIC is considerably suppressed due to the limited maximum energy of the primary CR electrons which reduces that effect in the WHIM.

7 PREDICTION OF THE γ -RAY EMISSION FROM NEARBY GALAXY CLUSTERS

We use the mass-to-luminosity scaling relations as derived in Section 6 in combinations with the virial masses of galaxy clusters of the extended HIFLUGCS catalogue (Reiprich & Böhringer 2002) – the “Highest X-ray FLUX Galaxy Cluster Sample” from the ROSAT all-sky survey – to predict their γ -ray emission.¹⁴ In Fig. 18, we show the γ -ray flux for radii $R < R_{\text{vir}}$ and energies above 100 MeV and 100 GeV, as a function of the identifier (ID) in the extended HIFLUGCS catalogue. We specifically name those clusters that have a flux (in our optimistic model) which is larger than the sensitivity of the Fermi all-sky survey after two years of data taking. We find that the *brightest clusters in γ -rays are Virgo, Ophiuchus, Coma, Perseus and Fornax*. This result agrees well with previous γ -ray studies using galaxy clusters from the HIFLUGCS sample (Pfrommer 2008; Jeltema et al. 2009).

Figure 18 should serve as a starting point to identify promising sources for the γ -ray experiment in question. In a realistic setting, we would have to include the instrumental response and the point-spread function to obtain the predicted detection significance for the model in question. We note that this procedure of using scaling relations does not take into account deviations of individual systems from the mean γ -ray flux at a given cluster mass. One would rather have to model each system separately along the lines presented in Section 5.

To address the effect of source extension on the detection significance of Fermi, we compute the γ -ray flux of each cluster within the Fermi equivalent angular resolution at 100 MeV in Fig. 19. To this end, we interpolate the scaling relations in Table 5 to the radius corresponding to the angular resolution of 3.5 deg. We limit the size of each source to $3R_{\text{vir}}$ since there is negligible additional flux beyond this radius. For most clusters the flux is very similar to what we found in Fig. 18 because of the similar mass to luminosity scaling relations for R_{vir} and $3R_{\text{vir}}$.

8 DISCUSSION AND COMPARISON TO PREVIOUS WORK

8.1 Comparison to previous work on γ -ray emission from clusters

In support of the new instrumental capabilities in γ -ray astronomy, several pioneering papers have appeared that simulate the high-energy γ -ray emission from clusters. Here we make a comparison to some of those papers.

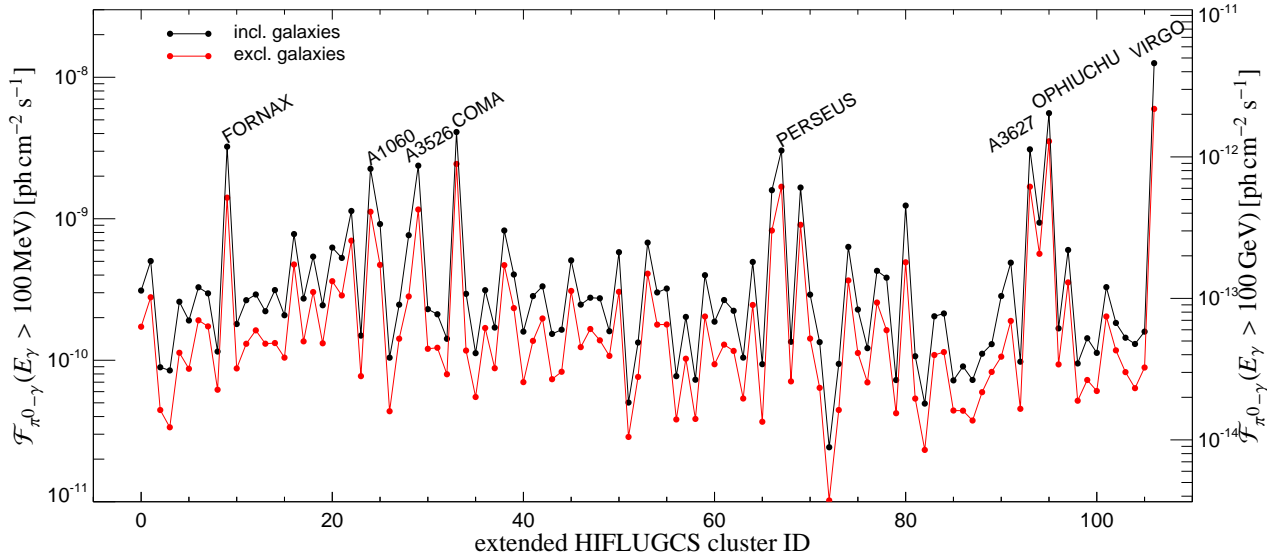
Comparison to Pfrommer et al. – In the series of papers Pfrommer et al. (2007, 2008) and Pfrommer (2008) simulate the same cluster sample as we do. In fact, our work represents an extension of these earlier works. Overall, our results are in continuity with their results. The differences emerge from the details of the

¹⁴ We have also added the Virgo cluster to the sample that we nevertheless refer to as extended HIFLUGCS catalogue in the following.

Table 5. Cluster γ -ray scaling relations⁽¹⁾.

model ⁽²⁾	γ -rays ($E_\gamma > 100$ MeV):		γ -rays ($E_\gamma > 1$ GeV):		γ -rays ($E_\gamma > 100$ GeV):	
	$\mathcal{L}_{\gamma,0}^{(3)}$	β_γ	$\mathcal{L}_{\gamma,0}^{(4)}$	β_γ	$\mathcal{L}_{\gamma,0}^{(5)}$	β_γ
Including galaxies, $1 R_{\text{vir}}$	5.24 ± 0.99	1.34 ± 0.09	7.83 ± 1.70	1.35 ± 0.10	2.78 ± 0.71	1.33 ± 0.13
Including galaxies, $2 R_{\text{vir}}$	5.73 ± 0.97	1.24 ± 0.09	8.48 ± 1.64	1.24 ± 0.10	3.00 ± 0.71	1.23 ± 0.12
Including galaxies, $3 R_{\text{vir}}$	6.53 ± 1.20	1.14 ± 0.08	9.63 ± 1.87	1.15 ± 0.09	3.47 ± 0.76	1.14 ± 0.11
Excluding galaxies, $1 R_{\text{vir}}$	3.13 ± 0.37	1.46 ± 0.06	4.02 ± 0.42	1.43 ± 0.07	1.16 ± 0.11	1.34 ± 0.08
Excluding galaxies, $2 R_{\text{vir}}$	3.32 ± 0.54	1.41 ± 0.08	4.22 ± 0.53	1.39 ± 0.06	1.24 ± 0.19	1.31 ± 0.08
Excluding galaxies, $3 R_{\text{vir}}$	3.44 ± 0.43	1.39 ± 0.06	4.37 ± 0.57	1.37 ± 0.07	1.30 ± 0.20	1.29 ± 0.08

Notes:

(1) The cluster γ -ray scaling relations are defined by $A = A_0 M_{15}^\beta$, where $M_{15} = M_{\text{vir}}/(10^{15} M_\odot)$.(2) The γ -ray luminosity from respective cluster is obtained by integrating over the region within an integer times R_{vir} . For scaling relations that include galaxies, we apply a central core cut-out and exclude a spherical region with radius $r < 0.025 R_{\text{vir}}$ that is centered on the brightest central γ -ray point-source.(3) The normalization of the γ -ray scaling relations ($E_\gamma > 100$ MeV) is given in units of 10^{45} ph s^{-1} .(4) The normalization of the γ -ray scaling relations ($E_\gamma > 1$ GeV) is given in units of 10^{44} ph s^{-1} .(5) The normalization of the γ -ray scaling relations ($E_\gamma > 100$ GeV) is given in units of 10^{42} ph s^{-1} .**Figure 18.** Predicted γ -ray flux in clusters and groups in the extended HIFLUGCS catalog to which we also add the Virgo cluster. For each cluster and group, we account for the flux from the region within one virial radius. The left axis shows the flux above 100 MeV while the right axis accounts for the flux above 100 GeV. The black line refers to our optimistic model where we include the flux contribution from galaxies and the red line shows the flux without galaxies (cf. Table 5). We name the clusters and groups with $\mathcal{F}_{\pi^0-\gamma}(E_\gamma > 100 \text{ MeV}) > 2 \times 10^{-9}$ ph $\text{cm}^{-2} \text{s}^{-1}$ in our optimistic model which roughly corresponds to the sensitivity of the Fermi all-sky survey after two years of data taking.

CR physics, where they adopted a simplified description using a single CR population with a spectral index of 2.3. Hence they concentrated on the non-thermal radio emission as well as the γ -ray emission at energies $E_\gamma > 100$ MeV that depend only weakly on the particular value or even a running of the CR spectral index (as long as it is close to the true one). For the primary electron populations, a maximum electron injection efficiency of $\zeta_e = 0.05$ was assumed. In addition, the bias from anomalous galaxies was not addressed.

Comparing profiles of the total surface brightness above 100 MeV in our optimistic model with galaxies, shown in grey in Fig. 4, to the brightness profiles in Pfrommer et al. (2008), we find only very small differences. These differences are caused by a combination of different binning and Poisson noise in the galaxies' spatial distribution which have a different realization due to our

slightly modified CR description that changes the hydrodynamics. The largest difference is seen for the pIC component in the periphery of merging clusters and a consequence of the different values for the injection efficiency ζ_e adopted. In addition, we compare the mass to luminosity scaling relation above 100 MeV in our optimistic model (see Table 5) and find that they agree to the percent level with what was found in Pfrommer (2008).

Comparison to Miniati et al. – There have been a series of pioneering papers simulating the non-thermal emission from clusters by numerically modelling discretized CR proton and electron spectra on top of Eulerian grid-based cosmological simulations (Miniati 2001; Miniati et al. 2001a,b; Miniati 2002, 2003). In contrast to our approach, these models neglected the hydrodynamic pressure of the CR component, were quite limited in their adaptive resolution capability, and they neglected dissipative gas physics including radia-

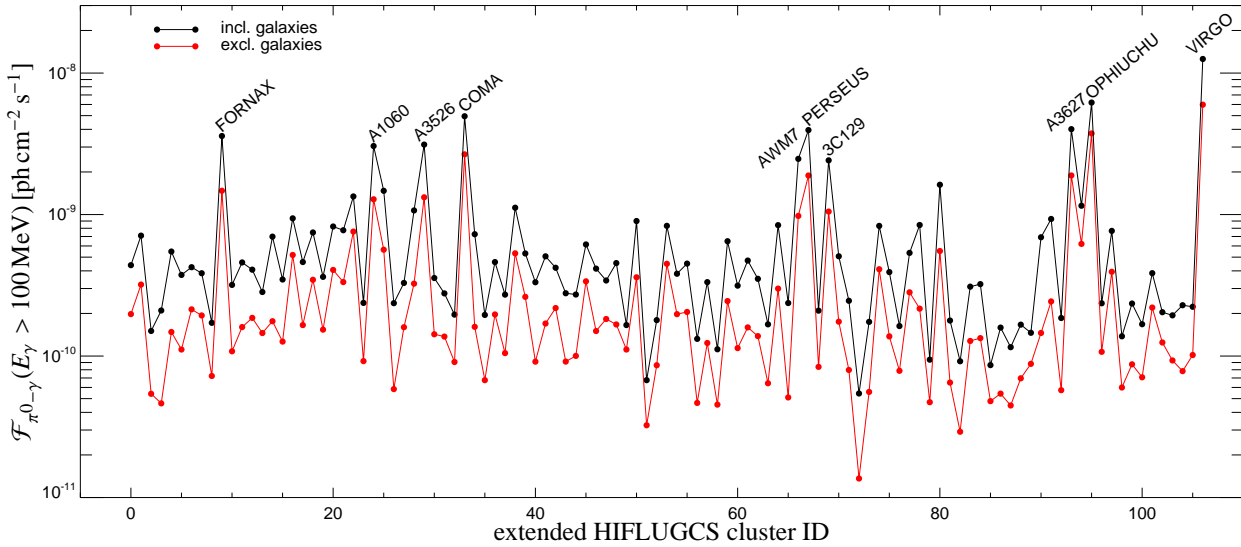


Figure 19. Predicted γ -ray flux above 100 MeV in clusters and groups in the extended HIFLUGCS catalog to which we also add the Virgo cluster. The flux comes from the region within the Fermi angular resolution at 100 MeV, i.e. a circular region of radius 3.5 degree that contains 68 per cent of the PSF, but with the limit at $3 R_{\text{vir}}$ for each cluster and group. The black line refers to our optimistic model where we include the flux contribution from galaxies and the red line shows the flux without galaxies (cf. Table 5). We name the clusters and groups with $\mathcal{F}_{\pi^0-\gamma}(E_\gamma > 100 \text{ MeV}) > 2 \times 10^{-9} \text{ ph cm}^{-2} \text{ s}^{-1}$ in our optimistic model which roughly corresponds to the sensitivity of the Fermi all-sky survey after two years of data taking.

tive cooling, star formation, and supernova feedback. Comparing the γ -ray emission characteristics of the IC emission from primary CR electrons and hadronically generated secondary CR electrons as well as the pion decay γ -rays, we confirm the qualitative picture of the emission characteristics of the different γ -ray components put forward by these authors. However, we find important differences on smaller scales especially in cluster cores, the emission strength of the individual components and their spectra.

We confirm that the high-energy γ -ray emission ($E_\gamma > 100 \text{ MeV}$) from cluster cores is dominated by pion decays while at lower energies, the IC emission of secondary CR electrons takes over (Miniati 2003). We reproduce their finding that the γ -ray emission in the virial regions of clusters and beyond in super-cluster regions is very inhomogeneous and stems in part from the IC emission of primary shock accelerated electrons. Contrarily to these authors, we find that the surface brightness of this emission component remains sub-dominant in projection compared to the hadronically induced emission components in the cluster core and that the pion decay completely dominates the high-energy γ -ray emission of clusters above a few MeV (cf. Fig. 1). In addition we predict a pIC spectrum that is somewhat steeper with a photon index of $\Gamma \simeq 1.15$ which resembles a steeper primary electron spectrum in our simulations compared to theirs. This points to on average weaker shocks that are responsible for the acceleration of primary CR electrons that dominate the pIC emission. This discrepancy of the pIC spectral index causes the discrepancy of the pIC flux at high γ -ray energies.

In the WHIM we find that the pIC emission dominates the total γ -ray spectrum below about 100 MeV, and a comparable flux level of π^0 -decay and pIC between 100 MeV and 1 TeV, where the π^0 -decay takes over. This is in stark contrast to the finding of Miniati (2003), where the pIC is dominating the pion decay emission by a factor of about 10 or more over the entire γ -ray energy band. We note that our γ -ray fluxes for clusters are typically a factor of two

smaller than the estimates given in Miniati et al. (2001a) which has important implications for the detectability of clusters by Fermi.

There are several factors contributing to the mentioned discrepancies. (1) Our simulations are Lagrangian in nature and hence adaptively resolve denser structures with a peak resolution of $5 h^{-1} \text{ kpc}$. In contrast, the cosmological simulations of Miniati (2003) have a fixed spatial resolution of $\sim 100 h^{-1} \text{ kpc}$ which is too coarse to resolve the observationally accessible, dense central regions of clusters in this grid-based approach and underestimates CR cooling processes such as Coulomb and hadronic losses. It also cannot resolve the adiabatic compression of CRs into the core. (2) Miniati et al. (2000) identified shocks with Mach numbers in the range $4 \lesssim \mathcal{M} \lesssim 5$ as the most important in thermalizing the plasma. In contrast, Ryu et al. (2003), Pfrommer et al. (2006), and Skillman et al. (2008) found that the Mach number distribution peaks in the range $1 \lesssim \mathcal{M} \lesssim 3$. This finding seems to be robust as different computational methods have been used which range from fixed and adaptive Eulerian grid codes to Lagrangian Tree-SPH codes. Since diffusive shock acceleration of CRs depends sensitively on the Mach number, this implies a more efficient CR injection in the simulations by Miniati et al. (2001a). It also results in a flatter CR electron and CR ion spectrum compared to ours shown in Fig. 1. Hence, the pIC emission of Miniati (2003) has a flatter photon index and a boosted flux. (3) For the CR ion spectrum, Miniati (2003) uses only four momentum bins which is not enough to resolve the pion bump accurately. The large pion decay plateau which he found indicates a constant CR ion spectral index in this energy range. This is in contradiction to the concavely shaped CR spectrum that our cluster simulations show, where the shape is a consequence of the Mach number statistics and the adiabatic transport. The difference in the CR spectral shape is especially important for CR energies above 1 GeV, since those CRs give rise to the π^0 -decay emission at energies above the pion bump.

Comparison to Kushnir et al. – Kushnir & Waxman (2009) use a simple analytic model to follow the evolution of ICM CRs,

accelerated in strong accretion shocks. Interestingly, their approach predicts similar characteristics for the pion decay emission, in particular its flux agrees with our prediction within a factor two. In contrast, their model predicts a high-energy γ -ray flux of the pIC component that is approximately a factor of 600 larger than ours due to a different spectral description where they adopted a spectral index of 2. This, however, is in conflict with our simulated average spectral index of 2.3 that is a consequence of cluster assembly history (compare our Fig. 4 with Fig. 3 in Kushnir & Waxman 2009). This finding, together with different adopted values for the electron injection efficiency and CR-to-thermal ratio, led them to the contradicting conclusion that the expected overall γ -ray emission would be much more extended. We believe that their model would over-predict the amount of observed radio relic emission in clusters, in particular when considering magnetic field amplification at accretion shocks on a level that is only a fraction of what is observed in supernova remnant shocks (Uchiyama et al. 2007). It can be easily seen that the different power-law indices are indeed the reason for the flux discrepancies by comparing the energy flux of electrons at 170 GeV which are responsible for IC photons at 100 MeV (assuming the up-scattering of CMB photons). Adopting our effective spectral injection index of primary electrons of $\alpha_{e,inj} \simeq 2.3$ and assuming a post-shock temperature at a typical accretion shock of $kT \simeq 0.1$ keV, we find a flux ratio between their model and ours of $(0.1 \text{ keV}/170 \text{ GeV})^{-0.3} \simeq 600$.

We would like to compare their model predictions for the pion decay emission in more detail. To this end, we use a proton injection efficiency in their model of $\eta_p \simeq 0.2$ for the comparison. In our simulations we use a maximum proton injection efficiency of $\eta_{\text{max},p} = 0.5$. The proton injection efficiency in our simulations is dynamical, and depends on the strength of the shocks. Since the cluster evolves with time and the majority of CRs are injected at higher redshift during the formation of clusters, the final CR pressure depends on the interesting interplay of the actual value of the shock injection efficiency and the successive CR transport. Using results from (EnBlin et al. 2007), we estimate an effective injection efficiency of approximately $\eta_p \simeq 0.2$. We note, however, that their baseline model assumes $\eta_p = 0.02$, which will suppress the flux by a factor 10 in their model. We now contrast the γ -ray flux predictions of the Coma and Perseus cluster of our semi-analytic model to the one worked out in Kushnir & Waxman (2009). First we study the γ -ray flux from Coma within $R_\theta = R_{\text{vir}}$ above 100 MeV where we find with their model a flux $\mathcal{F}_{\pi^0-\gamma,k\&w}(> 100 \text{ MeV}) = (0.70 - 1.7) \times 10^{-9} \text{ ph cm}^{-2} \text{ s}^{-1}$. This flux is only a factor two lower than what we predict for the pion decay emission from Coma. Turning to pIC, which play a much more important role for the total γ -ray flux than the π^0 -decay emission in their model, results in the flux $\mathcal{F}_{\text{pIC},k\&w}(> 100 \text{ MeV}) \simeq 1.5 \times 10^{-8} \text{ ph cm}^{-2} \text{ s}^{-1}$. This is only a factor two below the EGRET upper limit and can be readily tested with the one-year data from Fermi.

Studying fluxes in the TeV γ -ray regime is also of great importance since it compares the spectral representation of the models. Using the analytic model of Kushnir & Waxman (2009), results in the flux $\mathcal{F}_{\pi^0-\gamma,coma}(> 1 \text{ TeV}) = 9.3 \times 10^{-14} \text{ ph cm}^{-2} \text{ s}^{-1}$ within $\theta = 0.2$ deg that is about a factor 10 below the upper limit for Coma set by HESS and only a factor two larger than the flux we predict for Coma. However, their result is most probably flawed by their too simplistic assumption for the CR spectral index of $\alpha = 2$. If we use our universal concave shaped spectrum instead of their flat CR spectrum, we can show that their flux would decrease by a factor $\sim (1 \text{ TeV}/100 \text{ MeV})^{(\Gamma_{100 \text{ MeV}}^{1 \text{ TeV}} - 1)} \sim 10^{4 \times 0.24} \sim 9$.

Finally we study the surface brightness profiles from Coma

and Perseus predicted by our semi-analytic model and compare it to theirs. The dashed and dotted-dashed lines in Fig. 13 show their predictions for the Coma cluster above the energy 100 MeV and 100 GeV, respectively. Using their formalism we find a surface brightness above 100 MeV that is about a factor two smaller than what we predict. However, above 100 GeV our predictions are in better agreement.

8.2 Limitations and future work

The ideal CR formalism would trace the spectral energy evolution, as well as the spatial evolution of CRs, and at the same time keep track of the dynamical non-linear coupling with magneto-hydrodynamics. In order to make cosmological simulations less expensive in computational power, we are forced to make compromises. The simplifying assumptions chosen, enable us to run cosmological simulations of the formation of galaxy clusters with the necessary resolution to resolve their cores. At the same time, these assumptions enable us to follow the CR physics self-consistently on top of the radiative gas physics. Here we outline our most severe limitations for computing the γ -ray emission from clusters.

(i) In our simulations we neglect the effect of microscopic CR diffusion and CR streaming. The collisionless plasma forces CRs to stay predominantly on a given field line and to diffuse along it. The random walk of field lines cause initially closely confined CRs to be transported to larger scales which can be described as a diffusion process. In our model we assume the magnetic field to be tangled on scales smaller than those we are interested in, $\lambda \sim 10$ kpc in the center and even larger scales outside. Hence, CRs are magnetically coupled to the thermal gas and advected alongside it. The diffusivity can be rewritten into a macroscopic advection term that we fully resolve in our Lagrangian SPH simulations by construction and a microscopic diffusivity. The advection term dominates over microscopic term, as the following estimate for the diffusivities shows: $\kappa_{\text{adv}} \simeq 100 \text{ kpc} \times 1000 \text{ km/s} \simeq 10^{31.5} \text{ cm}^2/\text{s} \gg \kappa_{\text{diff}} \simeq 10^{29} \text{ cm}^2/\text{s}$. Further work is needed to study microscopic anisotropic diffusion, in combination with self-consistent modelling of the magnetic fields.

(ii) We also did not account for the injection of CRs by AGN or supernova remnants where the additional CRs would diffuse out of AGN-inflated bubbles or drive starburst winds that enrich the IGM. In addition we do not account for the feedback processes by AGN despite their importance for understanding the nature of the very X-ray luminous cool cores found in many clusters of galaxies. For further details we refer the reader to Sijacki et al. (2008).

(iii) We postpone the study of the potential contribution of a population of re-accelerated electrons to the IC γ -ray emission throughout this work: strong merger shocks and shear motions at the cluster periphery might inject hydrodynamic turbulence that cascades to smaller scales, feeds the MHD turbulence and eventually might be able to re-accelerate an aged CR electron population. Due to non-locality and intermittency of turbulence, this could partly smooth the very inhomogeneous primary emission component predominantly in the virial regions of clusters where simulations indicate a higher energy density in random motions. However, to study these effects, high-resolution AMR simulations are required that refine not only on the mass but also on some tracer for turbulence such as the dimensionless vorticity parameter (Iapichino et al. 2008; Iapichino & Niemeyer 2008; Maier et al. 2009).

(iv) Our model for the diffusive shock acceleration assumes a

featureless power-law for both, the proton and the electron acceleration, that is injected from the thermal distribution. The complete theoretical understanding of this mechanism is currently an active research topic that includes non-linear effects and magnetic field amplification (Vladimirov et al. 2006). Phenomenologically, we believe that there are strong indications for the diffusive shock acceleration mechanism to be at work which come from observations of supernova remnants over a wide range of wavelengths from the radio, X-rays into the TeV γ -rays (e.g., Ellison 2000; Hughes et al. 2000; Ellison & et al. 2005; Warren et al. 2005; Aharonian et al. 2004, 2006) as well as the bow shock of the Earth (Ellison et al. 1990; Shimada et al. 1999). Theoretical work suggests that the spectrum of CRs which is injected at strong shocks shows an intrinsic concave curvature: the feedback of the freshly accelerated and dynamically important CR pressure to the shock structure results in a weaker sub-shock that is preceded by a smooth CR precursor extending into the upstream. Hence low-energy protons are only shock-compressed at the weaker sub-shock and experience a smaller density jump which results in a steeper low-energy spectrum (compared to the canonical value $\alpha = 2$ from linear theory). In contrast, the Larmor radii of high-energy protons also sample the CR precursor and experience a much larger density contrast that results in a flatter high-energy spectrum with $\alpha < 2$ (Ellison & Eichler 1984; Amato et al. 2008; Caprioli et al. 2009). The low-energy part of the CR spectrum in clusters (as found in this work) should be unaffected since a softer population of CRs dominate there with $\alpha \sim 2.5$ and non-linear effects are presumably negligible in this regime. However the high-energy part of the CR spectrum in clusters could become harder compared to what we found due to these non-linear effects. Future work will be dedicated to improve our model and to incorporate more elaborate plasma physical models and to study the uncertainty of our results with respect to the saturated value of our CR acceleration efficiency (e.g., Kang & Jones 2007; Edmon et al. 2007).

(v) An artificial surface tension effect limits the ability of SPH (in its standard conservative form) to follow the growth of boundary instabilities such as the Kelvin-Helmholtz instability at the interface of a dense and under-dense phase accurately, i.e. on the predicted linear growth time (Agertz et al. 2007). In the context of galaxy cluster simulations, this only occurs at the interface of the ISM of individual galaxies and the ICM. This causes an unphysically long survival time of dense gaseous point sources after they got ram pressure/tidally stripped from their galactic halo – for simplicity, we call them "galaxies" and describe the physics in detail in Section 2.5. In our paper, we decided to show our result for an optimistic model that includes all galaxies and one conservative model that cuts all galaxies. This is meant to bracket the realistic case. Also, the main result is based on our conservative model where we cut out the galaxies. In this way we circumvent these issues.

8.3 Impact of these limitations on our results

Generally, we acknowledge that the CR spatial distribution is more uncertain than the spectrum due to the details outlined in Section 8.2. Below, we detail our considerations why we believe that the spectrum that we found is robust even when considering uncertainties such as additional CRs injected from AGN, re-acceleration of CRs at MHD turbulence, CR diffusion, and non-linear shock acceleration. We outline here the reasons in detail:

Additional CRs injected from AGN. It is very uncertain whether AGN jets are powered hadronically or through Poynting flux (e.g., Celotti et al. 1998; Hirotani & Okamoto 1998;

Sikora & Madejski 2000). Irrespectively, the energetics of AGN are insufficient to account for a majority of CRs in clusters – in particular for the most massive systems (Thompson & Pfrommer in prep.).

CR re-acceleration through MHD turbulence. The involved physics is currently very uncertain such as the level and nature of turbulence in the ICM, how CRs exactly interact with plasma waves, how efficient this accelerates CRs, and whether a power-law extrapolation between the gyro radius of a CR, $R \sim 10^{-5} \text{ pc } (B/\mu\text{G})^{-1} (E/10 \text{ GeV})$, and the scales accessible to current simulations with peak resolution of a few kpc is justified. Hence it appears that it is impossible to constrain the impact of turbulent re-acceleration on the CR spectrum in clusters self-consistently from first principles. However, in our Milky Way, we are able to understand the observed CR spectrum on Earth with $f_{\text{CR}} \sim p^{-2.7}$ fairly well in terms of injection and transport. CRs with an injected spectrum of $p^{-(2.3-2.4)}$ experience momentum dependent diffusion so that the more energetic particles can leave the system in a so-called 'leaky-box model'; an effect that accounts for the observed steepening (Schlickeiser 2002). This leaves little room for spectral modifications through turbulent re-acceleration. Hypothesizing that the fundamental interactions of plasma waves with particles should not be very different in the ISM and ICM, we believe that we are safe to neglect this process to first order. Note, however, that this argument neglects possible important CR transport processes that might become important in the cluster environment due to the much longer CR life time compared to the ISM in our Galaxy.

Spatial diffusion of CRs. If spatial CR diffusion is momentum dependent it will introduce a radial dependence in the shape of the CR spectrum since high energy CRs can diffuse out of the central regions faster. This, in turn, will affect the observed morphology and spectrum of all relevant non-thermal emission components, including gamma-rays from pion decay, IC from secondaries, and synchrotron emission.

Non-linear shock acceleration. Since the CR spectrum at GeV-to-TeV energies is sufficiently steep, intermediate Mach number shocks are responsible for the acceleration of these CRs – with efficiencies there are modest (not in the saturated regime) so that the non-linear back-reaction is expected to be small or even negligible.

Over-cooling problem. Due to the over-cooling problem, the modeling of cluster cores with radiative cooling but without any significant feedback process produces an unphysically high stellar mass fraction. This is not expected to impact the CR spectrum significantly. However, the effect on the CR morphology might be substantial and might depend on the details of the required feedback process. This can potentially impact the non-thermal cluster observables. Future work is needed to solve this problem.

9 CONCLUSIONS

In this paper we have simulated 14 galaxy clusters spanning two orders of magnitude in mass and a broad range of dynamical stages. The simulations follow self-consistent CR physics on top of the dissipative gas physics including radiative cooling and star formation. We have simulated high-energy γ -ray emission maps, profiles and spectra of various emission components. These include the inverse Compton emission from primary, shock-accelerated electrons (pIC) and secondary electrons that result from hadronic interactions of CR protons with ambient gas protons (sIC), as well as γ -rays from neutral pion decay that are also generated in these hadronic reactions.

We would like to emphasize that we focus on the intrinsic

spectrum emitted at the cluster position without taking into account photon propagation effects to highlight the various physical processes that shape the emission spectra. Depending on the cluster redshift, these spectra attain a high-energy cutoff due to e^+e^- -pair production on IR and optical photons which can be easily derived from the photon-photon opacity (e.g., Franceschini et al. 2008). We also caution the reader that we assume an optimistic value for the maximum shock injection efficiency (based on data from supernova remnant studies by Helder et al. 2009); smaller values would reduce the resulting γ -ray emission accordingly. To date it is not clear whether these high efficiencies apply in an average sense to strong collisionless shocks or whether they are realized for structure formation shocks at higher redshifts. Hence the goal of this work is to establish a thorough framework and to predict the level of γ -ray emission that we expect for this efficiency. We note that one cannot lower the acceleration efficiency infinitely if one wants to explain radio (mini-)halos in the hadronic model of CR interactions. For clusters that host such a large, unpolarized, and centrally peaked radio halo emission that resembles the thermal X-ray surface brightness, one can derive a minimum γ -ray flux. The idea is based on the fact that a steady state distribution of CR electrons loses all its energy to synchrotron radiation for strong magnetic fields ($B \gg B_{\text{CMB}} \approx 3.2\mu\text{G} \times (1+z)^2$) so that the ratio of γ -ray to synchrotron flux becomes independent of the spatial distribution of CRs and thermal gas. Lowering the magnetic field would require an increase in the energy density of CR electrons to reproduce the observed synchrotron luminosity and thus increase the associated γ -ray flux (for applications to Coma and Perseus, see Pfrommer 2008; Aleksić et al. 2010, respectively).

According to our simulations, clusters have very similar morphology in the 100 MeV - 100 GeV Fermi band, and in the 100 GeV - 10 TeV Čerenkov band. This is due to the power-law spectra of the dominating pion decay emission (which show a slowly running spectral index) and ultimately inherited by the parent CR proton distribution. The emission from the central parts of clusters are dominated by γ -rays from pion decay, while the periphery of the ICM and the WHIM have a considerable contribution from pIC, which is especially pronounced in merging clusters. The energy dependent photon index for 100 MeV to 1 GeV has a median value of $\Gamma = 0.9$ due to pion decay induced emission in the central parts of the clusters, while that in the periphery shows a slightly higher value of $\Gamma = 1.1$ which is due to the substantial contribution from pIC. In the energy range from 100 GeV to 1 TeV, the photon index steepens to $\Gamma = 1.25$ in the central regions. This spectral steepening in the cluster center is due to the convex curvature of the pion bump around 100 MeV causing a steepening in the asymptotic γ -ray spectrum at higher energies. The small concave curvature at higher energies is not able to compensate for this effect. At energies $E_\gamma \gtrsim 1$ TeV, the photon index in the cluster outskirts attain a much higher value due to a super-exponential cutoff of the primary IC spectrum. This emission component contributes substantially to the total γ -ray emission there. At these energies, the electron cooling time is smaller than the time scale for diffusive shock acceleration which causes this cutoff in the electron spectrum. We used a semi-analytic formula for the injected electrons from which we derive the cooled electron distribution with the characteristic super-exponential cutoff. The shape of this spectrum is passed on to the pIC spectrum and we capture this shape with a fit that is valid both in the low-energy Thomson regime as well as in the high-energy Klein-Nishina regime.

The simulated CR proton spectra show an approximate power-law in momentum with a few additional features; a cutoff at $p =$

$P_p/m_p c^2 \approx 0.1$, a concave shape between $p \approx 1 - 10^6$, and a steepening by $p^{1/3}$ between $p \approx 10^6 - 10^8$. The overall shape of the spectrum shows only little variance between the clusters, indicating a universal CR spectrum of galaxy clusters. The radial dependence of the spectrum within the virial radius is negligible to first order. This allowed us to construct a semi-analytic model of the median CR proton spectrum across our cluster sample. Using the semi-analytic CR spectrum we derive a semi-analytic formula for the γ -ray flux from the pion decay induced emission that dominates the total γ -ray spectrum above 100 MeV. We apply this formalism to the Perseus and Coma clusters, using their density profiles as inferred from X-ray measurements and predict that the flux from Perseus is close to the recent upper limits obtained by the MAGIC collaboration (Aleksić et al. 2010).

The mass-to-luminosity scaling for the 100 MeV, 1 GeV, and 100 GeV regimes show very similar slopes for both the total γ -ray luminosity and all the components, which is due to the small variance in the CR spectrum. Masking galaxies decreases the total γ -ray emission by a factor of 2-3. The cut has a larger effect on smaller mass clusters since the emission of low mass systems with smaller potential wells are easier to perturb – through accreting clumps of matter or nearby satellite systems. We also found that the presence of galaxies considerably increases the scatter in the γ -ray scaling relation. The region outside R_{vir} only contributes marginally (of order ten per cent) to the total γ -ray emission for massive clusters while it contributes significantly to the total γ -ray luminosity of low mass clusters with a factor $\lesssim 1.5$. This is again mostly due to the pion decay emission from satellite systems that have not yet accreted on the cluster. The flux of the pIC component is increased by a factor of 2 – 10 when the WHIM is included. This can be explained by the rather flat spatial profiles of the pIC emission.

Combining our γ -ray scaling relations with the virial masses of galaxy clusters of the extended HIFLUGCS catalogue, we predict a detection of a few galaxy clusters above 100 MeV with *Fermi* after two years, where Virgo, Ophiuchus, Coma, Perseus and Fornax are expected to be the brightest clusters in γ -rays (barring uncertainties in the injection efficiency). Since *Fermi* already discovered the central AGN in Virgo/M87 and Perseus/NGC1275 the detection of the somewhat more extended and dimmer pion decay component will be very challenging in these clusters and requires careful variability studies to subtract the AGN component. For energies above 100 GeV, the flux of these clusters as determined by our scaling relation is more than 5×10^3 times lower. This provides a challenge for current Čerenkov telescopes as it is almost an order magnitude lower than the 50 h sensitivities. However, future upgrades of IACTs or the CTA telescope might considerably change the expectations. We note however that these estimates are too conservative for cool core clusters, which are known to show enhanced X-ray fluxes by a factor of up to ten relative to clusters on the X-ray luminosity scaling relation. Since we expect the X-ray luminosity to tightly correlate with the γ -ray luminosity, this sub-class of clusters should provide very rewarding targets due to the ample target matter for inelastic collisions of relativistic protons leading to γ -rays. Applying our semi-analytic model for the γ -ray emission, we identify Perseus among the best suited clusters to target for the current IACT experiments.

ACKNOWLEDGMENTS

We thank our referee for a constructive report. We gratefully acknowledge the great atmosphere at the Kavli Institute for Theoretical Physics program on Particle Acceleration in Astrophysical Plasmas, in Santa Barbara (2009, July 26-October 3) where this paper was finished. That program was supported in part by the National Science Foundation under Grant No. PHY05-51164. A.P. is grateful the Swedish National Allocations Committee (SNAC) for the resources granted at HPC2N. C.P. gratefully acknowledges the financial support of the National Science and Engineering Research Council of Canada. Some computations were also performed on CITAs McKenzie and Sunnyvale clusters which are funded by the Canada Foundation for Innovation, the Ontario Innovation Trust, and the Ontario Research Fund.

REFERENCES

- Abdo A. A., Ackermann M., Ajello M., Asano K., Baldini L., Ballet J., Barbiellini G., Bastieri D., Baughman B. M., Bechtol K., Bellazzini R., Blandford R. D., et al. 2009, *ApJ*, 699, 31
- Abramowitz M., Stegun I. A., 1965, *Handbook of mathematical functions*. New York: Dover
- Acciari V. A., Aliu E., Arlen T., Aune T., Bautista M., Beilicke M., Benbow W., Boltuch D., Bradbury S. M., Buckley J. H., Bugaev V., Byrum K., et al. 2009, *Nature*, 462, 770
- Agertz O., Moore B., Stadel J., Potter D., Miniati F., Read J., Mayer L., Gawryszczak A., Kravtsov A., Nordlund Å., Pearce F., Quilis V., Rudd D., Springel V., Stone J., Tasker E., Teyssier R., Wadsley J., Walder R., 2007, *MNRAS*, 380, 963
- Aharonian F., Akhperjanian A. G., Anton G., Barres de Almeida U., Bazer-Bachi A. R., Becherini Y., Behera B., Bernlöhr K., Boisson C., Bochow A., et al. 2009, *A&A*, 502, 437
- Aharonian F., Akhperjanian A. G., Bazer-Bachi A. R., Beilicke M., Benbow W., Berge D., Bernlöhr K., Boisson C., Bolz O., Borrel V., Braun I., Breitling F., et al. 2006, *Nature*, 439, 695
- Aharonian F. A., Akhperjanian A. G., Aye K.-M., Bazer-Bachi A. R., Beilicke M., Benbow W., Berge D., Berghaus P., Bernlöhr K., Bolz O., Boisson C., Borgmeier C., et al. 2004, *Nature*, 432, 75
- Aleksić J., Antonelli L. A., Antoranz P., Backes M., Baixeras C., Balestra S., Barrio J. A., Bastieri D., Becerra González J., Bednarek W., Berdyugin A., Berger K., et al. 2010, *ApJ*, 710, 634
- Amato E., Blasi P., Gabici S., 2008, *MNRAS*, 385, 1946
- Berezinsky V. S., Blasi P., Ptuskin V. S., 1997, *ApJ*, 487, 529
- Blandford R., Eichler D., 1987, *Phys. Rep.*, 154, 1
- Blasi P., Colafrancesco S., 1999, *Astroparticle Physics*, 12, 169
- Blumenthal G. R., Gould R. J., 1970, *Reviews of Modern Physics*, 42, 237
- Briel U. G., Henry J. P., Boehringer H., 1992, *A&A*, 259, L31
- Briel U. G., Henry J. P., Lumb D. H., Arnaud M., Neumann D., Aghanim N., Gastaud R., Mittaz J. P. D., Sasseen T. P., Vestrand W. T., 2001, *A&A*, 365, L60
- Caprioli D., Amato E., Blasi P., 2009, *ArXiv e-prints*
- Celotti A., Kuncic Z., Rees M. J., Wardle J. F. C., 1998, *MNRAS*, 293, 288
- Churazov E., Forman W., Jones C., Böhringer H., 2003, *ApJ*, 590, 225
- Davé R., Cen R., Ostriker J. P., Bryan G. L., Hernquist L., Katz N., Weinberg D. H., Norman M. L., O’Shea B., 2001, *ApJ*, 552, 473
- Dennison B., 1980, *ApJL*, 239, L93
- Dolag K., Bartelmann M., Lesch H., 1999, *A&A*, 348, 351
- Dolag K., Borgani S., Murante G., Springel V., 2009, *MNRAS*, 399, 497
- Dolag K., Enßlin T. A., 2000, *A&A*, 362, 151
- Drury L. O., 1983, *Reports of Progress in Physics*, 46, 973
- Dubois Y., Teyssier R., 2008
- Dursi L. J., Pfrommer C., 2008, *ApJ*, 677, 993
- Edge A. C., Stewart G. C., Fabian A. C., 1992, *MNRAS*, 258, 177
- Edmon P. P., Jones T. W., Kang H., 2007, *ArXiv:0706.0587*
- Ellison D. C., 2000, in Mewaldt R. A., Jokipii J. R., Lee M. A., Möbius E., Zurbuchen T. H., eds, *Acceleration and Transport of Energetic Particles Observed in the Heliosphere Vol. 528 of American Institute of Physics Conference Series, The Cosmic Ray-X-ray Connection: Effects of Nonlinear Shock Acceleration on Photon Production in SNRs*. p. 383
- Ellison D. C., Eichler D., 1984, *ApJ*, 286, 691
- Ellison D. C., et al. 2005, in *International Cosmic Ray Conference Vol. 3 of International Cosmic Ray Conference, Thermal Particle Injection in Nonlinear Diffusive Shock Acceleration*. p. 261
- Ellison D. C., Jones F. C., Eichler D., 1981, *Journal of Geophysics Zeitschrift Geophysik*, 50, 110
- Ellison D. C., Moebius E., Paschmann G., 1990, *ApJ*, 352, 376
- Enßlin T. A., 2003, *A&A*, 399, 409
- Enßlin T. A., Biermann P. L., Klein U., Kohle S., 1998, *A&A*, 332, 395
- Enßlin T. A., Biermann P. L., Kronberg P. P., Wu X.-P., 1997, *ApJ*, 477, 560
- Enßlin T. A., Pfrommer C., Springel V., Jubelgas M., 2007, *A&A*, 473, 41
- Feretti L., 2003, in Bowyer S., Hwang C.-Y., eds, *Astronomical Society of the Pacific Conference Series Vol. 301 of Astronomical Society of the Pacific Conference Series, Radio Observations of Clusters of Galaxies*. pp 143–+
- Ferrari C., Govoni F., Schindler S., Bykov A. M., Rephaeli Y., 2008, *Space Science Reviews*, 134, 93
- Franceschini A., Rodighiero G., Vaccari M., 2008, *A&A*, 487, 837
- Freedman W. L., Madore B. F., Gibson B. K., Ferrarese L., Kelson D. D., Sakai S., Mould J. R., Kennicutt Jr. R. C., Ford H. C., Graham J. A., Huchra J. P., Hughes S. M. G., Illingworth G. D., Macri L. M., Stetson P. B., 2001, *ApJ*, 553, 47
- Gould R. J., 1972, *Physica*, 58, 379
- Hayashi E., White S. D. M., 2008, *MNRAS*, 388, 2
- Helder E. A., Vink J., Bassa C. G., Bamba A., Bleeker J. A. M., Funk S., Ghavamian P., van der Heyden K. J., Verbunt F., Yamazaki R., 2009, *Science*, 325, 719
- Hirovani K., Okamoto I., 1998, *ApJ*, 497, 563
- Hughes J. P., Rakowski C. E., Decourchelle A., 2000, *ApJL*, 543, L61
- Iapichino L., Adamek J., Schmidt W., Niemeyer J. C., 2008, *MNRAS*, 388, 1079
- Iapichino L., Niemeyer J. C., 2008, *MNRAS*, 388, 1089
- Inoue S., Nagashima M., 2005, in Aharonian F. A., Völk H. J., Horns D., eds, *High Energy Gamma-Ray Astronomy Vol. 745 of American Institute of Physics Conference Series, Gamma-Rays from Large Scale Structure Formation and the Warm-Hot Intergalactic Medium: Cosmic Baryometry with Gamma-Rays*. pp 567–572
- Jeltema T. E., Kehayias J., Profumo S., 2009, *Phys. Rev. D*, 80, 023005
- Jubelgas M., Springel V., Enßlin T., Pfrommer C., 2008, *A&A*, 481, 33

- Kang H., Jones T. W., 2005, *ApJ*, 620, 44
- Kang H., Jones T. W., 2007, *Astroparticle Physics*, 28, 232
- Katz N., Weinberg D. H., Hernquist L., 1996, *ApJS*, 105, 19
- Katz N., White S. D. M., 1993, *ApJ*, 412, 455
- Keshet U., Waxman E., Loeb A., Springel V., Hernquist L., 2003, *ApJ*, 585, 128
- Komatsu E., Seljak U., 2001, *MNRAS*, 327, 1353
- Kushnir D., Katz B., Waxman E., 2009, *Journal of Cosmology and Astro-Particle Physics*, 9, 24
- Kushnir D., Waxman E., 2009, *JCAP*, 0908, 002
- Loeb A., Waxman E., 2000, *Nature*, 405, 156
- Lu Y., Mo H. J., Katz N., Weinberg M. D., 2006, *MNRAS*, 368, 1931
- Maier A., Iapichino L., Schmidt W., Niemeyer J. C., 2009, *ApJ*, 707, 40
- Malkov M. A., O’C Drury L., 2001, *Reports of Progress in Physics*, 64, 429
- Markevitch M., Vikhlinin A., 2007, *Phys. Rep.*, 443, 1
- Miniati F., 2001, *Computer Physics Communications*, 141, 17
- Miniati F., 2002, *MNRAS*, 337, 199
- Miniati F., 2003, *MNRAS*, 342, 1009
- Miniati F., Jones T. W., Kang H., Ryu D., 2001b, *ApJ*, 562, 233
- Miniati F., Ryu D., Kang H., Jones T. W., 2001a, *ApJ*, 559, 59
- Miniati F., Ryu D., Kang H., Jones T. W., Cen R., Ostriker J. P., 2000, *ApJ*, 542, 608
- Molnar S. M., et al., 2009, *Astrophys. J.*, 696, 1640
- Percival W. J., Reid B. A., Eisenstein D. J., Bahcall N. A., Budavari T., Fukugita M., Gunn J. E., Ivezić Z., Knapp G. R., Kron R. G., Loveday J., Lupton R. H., McKay T. A., Meiksin A., Nichol R. C., Pope A. C., Schlegel D. J., Schneider D. P., et al. 2009, *arXiv:0907.1660*
- Pfrommer C., 2008, *MNRAS*, 385, 1242
- Pfrommer C., Dursi L. J., 2009, *arXiv:0911.2476*
- Pfrommer C., Enßlin T. A., 2003, *A&A*, 407, L73
- Pfrommer C., Enßlin T. A., 2004, *A&A*, 413, 17
- Pfrommer C., Enßlin T. A., Springel V., 2008, *MNRAS*, 385, 1211
- Pfrommer C., Enßlin T. A., Springel V., Jubelgas M., Dolag K., 2007, *MNRAS*, 378, 385
- Pfrommer C., Springel V., Enßlin T. A., Jubelgas M., 2006, *MNRAS*, 367, 113
- Quilis V., Ibanez J. M. A., Saez D., 1998, *ApJ*, 502, 518
- Reimer O., Pohl M., Sreekumar P., Mattox J. R., 2003, *ApJ*, 588, 155
- Reiprich T. H., Böhringer H., 2002, *ApJ*, 567, 716
- Rosati P., Borgani S., Norman C., 2002, *ARA&A*, 40, 539
- Rybicki G. B., Lightman A. P., 1979, *Radiative processes in astrophysics*. New York, Wiley-Interscience
- Ryu D., Kang H., Hallman E., Jones T. W., 2003, *ApJ*, 593, 599
- Sarazin C. L., 1999, *ApJ*, 520, 529
- Schlickeiser R., 2002, *Cosmic ray astrophysics*. Springer
- Shimada N., Terasawa T., Hoshino M., Naito T., Matsui H., Koi T., Maezawa K., 1999, *Ap&SS*, 264, 481
- Sijacki D., Pfrommer C., Springel V., Enßlin T. A., 2008, *MNRAS*, 387, 1403
- Sikora M., Madejski G., 2000, *ApJ*, 534, 109
- Skillman S. W., O’Shea B. W., Hallman E. J., Burns J. O., Norman M. L., 2008, *ApJ*, 689, 1063
- Slane P., Gaensler B. M., Dame T. M., Hughes J. P., Plucinsky P. P., Green A., 1999, *ApJ*, 525, 357
- Springel V., 2005, *MNRAS*, 364, 1105
- Springel V., Hernquist L., 2002, *MNRAS*, 333, 649
- Springel V., Yoshida N., White S. D. M., 2001, *New Astronomy*, 6, 79
- Totani T., Kitayama T., 2000, *ApJ*, 545, 572
- Uchiyama Y., Aharonian F. A., Tanaka T., Takahashi T., Maeda Y., 2007, *Nature*, 449, 576
- Vestrand W. T., 1982, *AJ*, 87, 1266
- Vikhlinin A., Kravtsov A., Forman W., Jones C., Markevitch M., Murray S. S., Van Speybroeck L., 2006, *ApJ*, 640, 691
- Vikhlinin A., Markevitch M., Murray S. S., Jones C., Forman W., Van Speybroeck L., 2005, *ApJ*, 628, 655
- Vink J., Bleeker J., van der Heyden K., Bykov A., Bamba A., Yamazaki R., 2006, *ApJL*, 648, L33
- Vladimirov A., Ellison D. C., Bykov A., 2006, *ApJ*, 652, 1246
- Vogt C., Enßlin T. A., 2005, *A&A*, 434, 67
- Voit G. M., 2005, *Reviews of Modern Physics*, 77, 207
- Völk H. J., Aharonian F. A., Breitschwerdt D., 1996, *Space Science Reviews*, 75, 279
- Warren J. S., Hughes J. P., Badenes C., Ghavamian P., McKee C. F., Moffett D., Plucinsky P. P., Rakowski C., Reynoso E., Slane P., 2005, *ApJ*, 634, 376
- Webb G.M. Drury L.O’C. B. P., 1984, *A&A*, 137, 185
- Yoshida N., Sheth R. K., Diaferio A., 2001, *MNRAS*, 328, 669
- Zhao D. H., Jing Y. P., Mo H. J., Börner G., 2009, *ApJ*, 707, 354
- Zirakashvili V. N., Aharonian F., 2007, *A&A*, 465, 695
- Zirakashvili V. N., Aharonian F. A., 2010, *ApJ*, 708, 965

APPENDIX A: SUPPORTING MATERIAL FOR OUR SEMI-ANALYTIC MODEL: SPECTRUM AND SPATIAL DISTRIBUTION

Here we present additional details on the spectral and spatial distribution of cosmic rays (CRs) that are important for the consistency of our semi-analytic model.

A1 Formalism for the semi-analytic modelling

The CR spectrum for each SPH particle at the dimensionless proton momentum $p = P_p/m_p c = 1$ is given by $f(p = 1, \mathbf{R}) = C(\mathbf{R})$, where we assume that the low-momentum cutoff $q < 1$. The CR normalization is denoted by $C = \tilde{C}\rho/m_p$, where C has units of inverse volume. At each radial bin, we use the the volume weighted C to calculate the normalized spectrum through

$$\begin{aligned} \langle f \rangle_v(p = 1, R) &\equiv f_{v,\text{sim}}(p = 1, R) = \frac{1}{V} \sum_{\text{SPH},i} \frac{M_i}{\rho_i} C_i \\ &= \frac{1}{V} \sum_{\text{SPH},i} \tilde{C}_i \frac{M_i}{m_p}, \end{aligned} \quad (\text{A1})$$

where the sum extends over SPH particles labeled by i . In our semi-analytic formalism, we provide a fit to the mass weighted \tilde{C} , denoted by \tilde{C}_M , and use the gas density profile (which in fact is the volume weighted density ρ_v , that we simply denoted by ρ throughout the paper). The two methods to calculate f_v are equivalent for all radial bins, since

$$\begin{aligned} f_{v,\text{ana}}(p = 1, R) &= \tilde{C}_M \frac{\rho_v}{m_p} = \frac{\sum_{\text{SPH},i} \tilde{C}_i M_i}{\sum_{\text{SPH},i} M_i} \frac{\sum_{\text{SPH},i} \frac{M_i}{\rho_i} \rho_i}{V m_p} \\ &= \frac{1}{V} \sum_{\text{SPH},i} \tilde{C}_i \frac{M_i}{m_p} = f_{v,\text{sim}}(p = 1, R). \end{aligned} \quad (\text{A2})$$

We use the CR proton spectrum to calculate the integrated γ -ray source density λ by integrating the inverse Compton (IC) and pion decay γ -ray source functions $s_\gamma(E_\gamma)$ given by equation (43) and by equation (19) of Pfrommer & Enßlin (2004), respectively. The luminosity is calculated through the volume integral of λ . In analogue to the CR spectrum, we show here that the pion decay induced luminosity on an SPH basis for any radial bin,

$$\begin{aligned} \mathcal{L}_{\text{sim}} &= \int dV \lambda_{\pi^0-\gamma}(E, R) \simeq \tilde{\lambda}_{\pi^0-\gamma}(E) \sum_{\text{SPH},i} \tilde{C}_i \frac{\rho_i^2}{\rho_0^2} \frac{M_i}{\rho_i} \\ &= \tilde{\lambda}_{\pi^0-\gamma}(E) \sum_{\text{SPH},i} \tilde{C}_i \frac{\rho_i M_i}{\rho_0^2}, \end{aligned} \quad (\text{A3})$$

is equivalent to our semi-analytic γ -ray luminosity

$$\begin{aligned} \mathcal{L}_{\text{ana}} &= \int dV \lambda_{\pi^0-\gamma}(E, R) = \lambda_v V \simeq \tilde{\lambda}_{\pi^0-\gamma}(E) \tilde{C}_M \frac{\rho_v^2}{\rho_0^2} V \\ &= \tilde{\lambda}_{\pi^0-\gamma}(E) \frac{\sum_{\text{SPH},i} M_i \tilde{C}_i}{\sum_{\text{SPH},i} M_i} \sum_{\text{SPH},i} \frac{\rho_i^2}{\rho_0^2} \frac{M_i}{\rho_i} \\ &\simeq \tilde{\lambda}_{\pi^0-\gamma}(E) \sum_{\text{SPH},i} \tilde{C}_i \frac{\rho_i M_i}{\rho_0^2} = \mathcal{L}_{\text{sim}}. \end{aligned} \quad (\text{A4})$$

In the semi-analytic expression in equation (A4), we have used that the spectral part is separable from the spatial part in the first approximation, and that \tilde{C} is only a weak function of radius in the second approximation. Both these assumptions are validated by the universal CR spectrum and approximate spatial universal profile that we found across our cluster sample where the details are shown in Section 4.

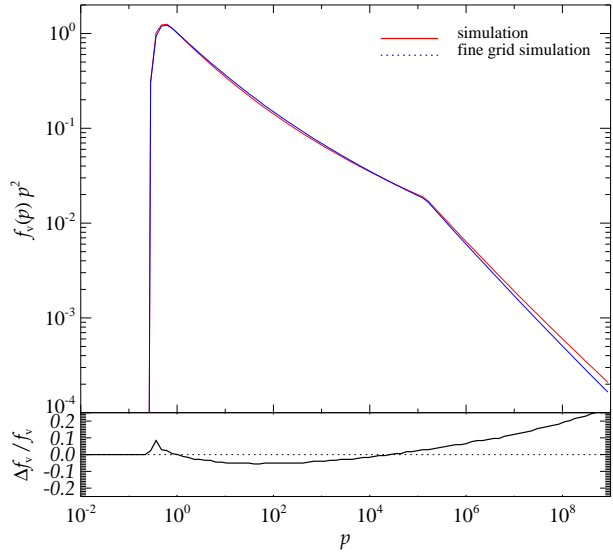


Figure A1. Convergence test for the CR spectrum: the main panel shows the volume weighted CR spectrum as a function of dimensionless CR momentum $p = P_p/m_p c$ for the small CC cluster g676. The red line represents our standard spectral resolution using $\alpha = (2.1, 2.3, 2.5, 2.7, 2.9)$, and the blue line shows the finer spectral resolution given by $\alpha = (2.1, 2.2, 2.3, 2.4, 2.5, 2.7)$. The bottom panel shows the difference between the two simulations normalized with the finer spectral resolution simulation.

A2 Spectral convergence test

Here we test the convergence of our updated CR model that we use in our simulations, where we account for both the spatial and spectral information of the CRs. In particular we allow for multiple CR populations, where each population is characterized by a fixed spectral index. For the test we run simulations with a finer spacing between the spectral indices, $\alpha = (2.1, 2.2, 2.3, 2.4, 2.5, 2.7)$, where we omitted the last bin $\alpha = 2.9$ that was found to have negligible contribution to the spectrum. In Fig. A1 we show the result of the convergence test of the CR spectrum for the small CC cluster g676. The red line shows g676 with our standard spectral resolution and the blue line shows the g676 simulation with a finer spectral resolution. The difference between the two simulations normalized with the spectrum from the better spectral resolution simulation is shown in the lower panel. In the GeV and TeV region the difference is less than 10 percent, showing that we are accurately able to capture the CR spectrum with our choice of α that has a wider spacing between the spectral indices.

A3 Variance of the spatial CR distribution

In this section we discuss the details of our spatial semi-analytic modelling and address the particle-by-particle variance of the spatial CR profile within a cluster. To this end, we plot the correlation space density of the dimensionless CR normalization \tilde{C} versus the overdensity of gas $\delta_{\text{gas}} = \rho/(\Omega_b \rho_{\text{cr}}) - 1$ for individual clusters. We over-plot the mean together with the 1-sigma standard deviation \tilde{C}_M as a function of overdensity. The scatter of 0.3 dex is roughly constant with density. This variance is most probably caused by the variance in shock strength and associated CR acceleration efficiency among different fluid elements in the past history of a cluster. If CRs are adiabatically transported into a cluster, we expect a weak radial dependence of the dimensionless normalization of

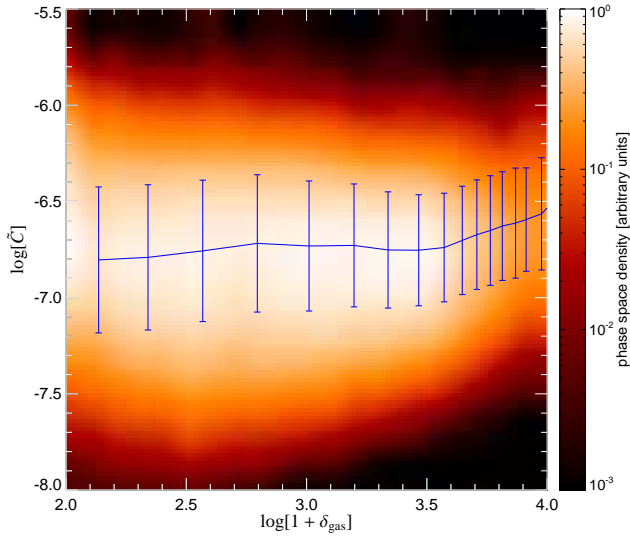


Figure A2. Correlation space density between the dimensionless normalization of the CR spectrum, \tilde{C} , and the overdensity $\delta_{\text{gas}} = \rho/(\Omega_b \rho_{\text{cr}}) - 1$, both in logarithmic representation. Shown is our simulated post-merging g72a cluster. The solid line shows the mean \tilde{C}_M as a function of the overdensity and the error bars the 1-sigma standard deviation.

the CR spectrum, $\tilde{C} \sim \rho^{(\alpha-1)/3}$ (Enßlin et al. 2007). However, we stress that the scale dependence of DM halos and which seems to be inherited by the gas and CR distribution could have an important effect in shaping \tilde{C} . Similarly, non-adiabatic CR transport effects could have another important impact on \tilde{C} . The outer cluster regions (particularly of mergers) typically host weak to intermediate strength shocks that increase \tilde{C} in that region. In contrast, in the very central cluster regions, the hadronic losses dominate and cause a suppression of \tilde{C} .

APPENDIX B: PRIMARY, SECONDARY ELECTRONS, AND INVERSE COMPTON EMISSION

In Section B1 we introduce the steady state cosmic ray electron (CRE) population for secondary electrons. These electrons are created through CR proton-proton interactions via charged pions decaying. The primary electrons in our simulations are accelerated through *diffusive shock acceleration* using the thermal leakage model originally proposed by Ellison et al. (1981). In Section B2 we start by deriving the primary steady state CRE population under the assumption that the diffusive time scale can be neglected. Then we continue the discussion for primary electrons where we additionally account for an energy dependent diffusion that in combination with the losses leads to a cutoff in the electron spectrum. In B3 we use these CRE spectra to calculate the integrated secondary and primary IC source functions. This description follows the approach of Enßlin et al. (2007), but we refer the reader to the appendix of Pfrommer et al. (2008) for a detailed discussion about electron acceleration, cooling, and IC emission within the framework of the SPH formalism.

B1 Secondary electrons

Here we provide the equilibrium distribution of secondary CR electrons above a GeV. It is shaped by the high-energy part of the CR

proton population that interacts with ambient gas and creates electrons through hadronic reactions. These electrons cool through IC and synchrotron radiative losses. The CRE equilibrium spectrum (Pfrommer et al. 2008) is derived through the balance of injection and losses, and is steeper by one compared to the CR proton spectrum ($\alpha_{e,i} = \alpha_i + 1$). The volume weighted spectrum is given by

$$f_e(p_e) dp_e = \sum_{i=1}^3 C_{e,i} p_e^{-\alpha_{e,i}} dp_e \quad (\text{B1})$$

$$C_{e,i} = \rho_v^2(R) \tilde{C}_M(R) \frac{16^{2-\alpha_{e,i}} \sigma_{pp,i} \Delta_i c^2}{(\alpha_{e,i} - 2) \sigma_T m_p (\varepsilon_B + \varepsilon_{\text{ph}})} \left(\frac{m_p}{m_e}\right)^{\alpha_{e,i}-3} \quad (\text{B2})$$

where $\tilde{C}_M(R)$ is the mass weighted CR proton normalization (equation 22), Δ_i the relative normalization for each CR population (equation 26), and $\sigma_{pp,i}$ denote the effective inelastic cross-section for proton-proton interactions and is defined in Section 5.1. In addition, σ_T represents the Thompson cross-section, ε_B is the magnetic energy density, and ε_{ph} denotes the photon energy density, taken to be that of CMB photons.

B2 Spectrum of shock-accelerated electrons

In clusters of galaxies, the dynamical and diffusive time scales of electrons are much longer compared to the shock injection and IC/synchrotron time scales. The radio synchrotron emitting electron population cools on such a short time scale $\tau_{\text{sync}} < 10^8$ yrs (compared to the very long dynamical time scale $\tau_{\text{dyn}} \sim 1$ Gyr) that we can describe this by instantaneous cooling at each timestep – in contrast to the CR protons. In combination with the fact that the CREs have a negligible pressure contribution, this enables us to account for the CREs in the post-processing. In this instantaneous cooling approximation, there is no steady-state electron population and we would have to convert the energy from the electrons to inverse Compton and synchrotron radiation. Instead, we introduce a virtual electron population that lives in the SPH-broadened shock volume only, defined to be the volume of energy dissipation. Within this volume, which is co-moving with the shock, we can use the steady-state solution for the distribution function of CR electrons and we assume no CR electrons in the post-shock volume, where no energy dissipation occurs. Thus, the CR electron equilibrium spectrum can be derived from balancing the shock injection with the IC/synchrotron cooling: above a GeV and below 30 TeV, it is given by

$$f_e(p_e) dp_e = C_e p_e^{-\alpha_e} dp_e, \quad (\text{B3})$$

$$C_e = \frac{3 C_{\text{inj}} m_e c}{4 (\alpha_e - 2) \sigma_T \tau_{\text{inj}} (\varepsilon_B + \varepsilon_{\text{ph}})}. \quad (\text{B4})$$

Here, we introduced the unit-less electron momentum $p_e = P_e/(m_e c)$, where P_e is the electron momentum. The spectral index of the equilibrium electron spectrum is denoted by $\alpha_e = \alpha_{\text{inj}} + 1$, where α_{inj} is the spectral index of the injected electron population in one-dimensional momentum space given by equation (1). The CR electron normalization scales linearly with the gas density $C_e \propto \rho$ which we evolve dynamically in our simulations and depends indirectly on α_{inj} and the dissipated energy rate per electron, \dot{E}_{diss} , through the normalization of the injected CREs, C_{inj} (for further details see Pfrommer et al. 2008). τ_{inj} represent the electron injection time scale, which depends on the time it takes for an electron to pass through the broadened shock.

The shape of the steady-state electron power-law spectrum in

equation (B3) changes when the energy of the accelerated electrons reach a maximum electron energy that is determined by the competition between the diffusive acceleration, and radiative synchrotron and IC losses. In the cutoff region, the spectrum is proportional to the product of two terms – a power-law term ($p_e^{4.5-\alpha_{\text{inj}}}$ which includes the phase space volume) and a super-exponential term, $\exp(-p_e^2/p_{\text{max}}^2)$. The first term reflects a pile-up of electrons as their cooling time becomes comparable to the acceleration time. The exponential term, however, effectively cancels this pile-up feature which results in a prolonged power-law up to the electron cutoff momentum $p_e \sim p_{\text{max}}$, where a steeper super-exponential cutoff takes over (Zirakashvili & Aharonian 2007). Applying the theory of plane-parallel shock acceleration that is justified because of the large curvature radius of the shock, the equilibrium electron distribution function at each position in the shock is given by

$$f_e(x, p_e) = C_e p_e^{-\alpha_{\text{inj}}} [1 + j(x, p_e)]^{\delta_e} \exp\left[\frac{-p_e^2}{p_{\text{max}}^2(x)}\right]. \quad (\text{B5})$$

Here, x is a spatial coordinate along the shock normal, measured from the shock position and the electron cutoff momentum is

$$p_{\text{max}}(x) \equiv (F + |x|G)^{-1}, \quad \text{where} \quad (\text{B6})$$

$$G \equiv \frac{u}{4p_0 a \kappa}, \quad \text{and} \quad (\text{B7})$$

$$F \equiv \frac{\alpha_{\text{inj}} + 2}{4p_0 a_1} + \frac{\alpha_{\text{inj}} - 1}{4p_0 a_2}. \quad (\text{B8})$$

The shape of the pile-up region of electrons in equation (B5) is given by $\delta_e = 9/5$ and the power-law function

$$j(x, p_e) = 0.66 \left(\frac{p_e}{p_{\text{max}}(x)}\right)^{\frac{5}{2}}. \quad (\text{B9})$$

The upstream quantities have the index 1 and the downstream quantities the index 2. The flow velocity in the inertial frame of the shock is denoted by u ($u_1 = v_s$, $u_2 = u_1/r_c$ where $r_c = \rho_2/\rho_1$ is the density compression factor at the shock), and p_0 represents the injection momentum normalized with $m_e c$. Note that the electron cutoff momentum p_{max} is independent of p_0 , as expected. The ratio between the cooling and diffusive acceleration time scales given by

$$a = \frac{u^2 \tau_{\text{loss}}}{4\kappa}. \quad (\text{B10})$$

Here, the inverse energy loss time scale of an electron dominated by synchrotron and inverse-Compton losses is given by

$$\tau_{\text{loss}}^{-1} = \frac{\dot{E}}{E} = \frac{4\sigma_T p_0}{3m_e c} (\epsilon_B + \epsilon_{\text{ph}}). \quad (\text{B11})$$

The CRe acceleration depends on the type of diffusion which we assume to be parallel to the magnetic field and to be in the Bohm-limit (as motivated by young supernova remnants observations, see also Section 2.4.1). The energy dependent diffusion constant is given by

$$\kappa = \eta \frac{c r_g}{3} = \eta \frac{p_e m_e c^3}{3Z e B}, \quad (\text{B12})$$

which we assume to be the same across the shock, i.e. $\kappa \approx \kappa_1 \approx \kappa_2$. We also use that the magnetic field fluctuations δB are of the same amplitude as the magnetic field $\eta = (B/\delta B)^2 \sim 1$.

Bohm diffusion becomes more effective at higher energies, which causes the cooling induced cutoff in the electron spectrum to move to lower energies as the electrons are transported advectively with the flow downstream. Integration over the post-shock volume causes the cutoffs to add up to the power-law that is steeper by unity compared to the injection power-law. Thus the steady-state

spectrum that balance losses through IC/synchrotron cooling with gains through electron shock acceleration, is derived through the integral over the IC radiating volume $\text{Vol} = SD$ (where S is the surface area, and D the thickness). It is given by

$$\begin{aligned} f_e(p_e) &= S \int_0^D dx f(x, p_e) \\ &\simeq \frac{S C_e}{\tilde{G}_2} \frac{\sqrt{\pi}}{2} p_e^{-(\alpha_{\text{inj}}+1)} [1 + J(p_e)]^{\delta_{e,\text{cool}}} \\ &\quad \times \left[\text{erf}(p_e D \tilde{G}_2 + p_e F) - \text{erf}(p_e F) \right], \end{aligned} \quad (\text{B13})$$

where erf is the standard Gaussian error function (Abramowitz & Stegun 1965). We do not expect the main characteristics of the pile-up region to change much when it is integrated over the post-shock regime (Zirakashvili & Aharonian 2007); to obtain a consistent semi-analytic formula of the spectrum, we determine the specific values of $J(p_e)$, \tilde{G}_2 , and $\delta_{e,\text{cool}}$ through fits to numerically integrated spectra (see below). The distribution function in equation (B13) has a break in the spectrum at the electron momentum $p_e = p_{e,\text{break}} = 1/D\tilde{G}_2$ and a cutoff at $p_e = p_{e,\text{cut}} = 1/F$. The electron momentum cutoff is determined from the strength of the magnetic field and the properties of electron diffusion in the shock (Webb G.M. 1984), and are given by

$$p_{e,\text{cut}} = \frac{1}{F} = \frac{1}{\frac{\alpha_{\text{inj}}+2}{4p_0 a_1} + \frac{\alpha_{\text{inj}}-1}{4p_0 a_2}} = \frac{3e B \tau_{\text{loss}} p_0}{p_e m_e c^3} \frac{1}{\frac{\alpha_{\text{inj}}+2}{u_1^2} + \frac{\alpha_{\text{inj}}-1}{u_2^2}}. \quad (\text{B14})$$

The equivalent electron energy cutoff in the relativistic regime is given by

$$E_{\text{max}} = p_{e,\text{cut}} m_e c^2 = u \left[\frac{6\pi e}{\sigma_T} \frac{B}{B^2 + B_{\text{CMB}}^2} \frac{r_c - 1}{r_c (r_c + 1)} \right]^{0.5}. \quad (\text{B15})$$

In Fig. B1 we show a comparison between our electron distribution given by equation (B13) compared to the electron spectrum in Enßlin et al. (1998) where an energy independent diffusion has been assumed. To plot the spectrum, we used typical values for the temperature, Mach number and density in the virial region. These values are found in Table 2. In addition we assumed a magnetic field amplification in the shock of a factor ten, resulting in a magnetic field of about $6\mu\text{G}$. The spectral comparison show that the spectral shapes are similar up to the cutoff region where the energy dependent Bohm diffusion in our model induces a steeper cutoff. Furthermore, the offset in the normalization of the two spectra between the break and cutoff regime is caused by the integrated pile-up regime (equation B9) that effectively increases the energy of the break from $1/DG_2$ to $1/D\tilde{G}_2$.

In Fig. B2 we show both the cooled electron spectra that we derive by numerically integrating $f_e(x, p_e)$ over the shock as well as the fitted spectra. For $f_e(p_e)$ we use typical values for both the strength of the shocks ($\alpha_e = 3.1$) and the break in the electron spectrum which we fix at a constant momentum ($p_{e,\text{break}} = 300 \text{ MeV}/m_e c^2$). In our fit, we allow for three independent fit variables, A_1 , A_2 , and A_3 . We find that,

$$\begin{aligned} A_1 &= 0.4, \quad A_2 = 1.45, \quad A_3 = 1.95, \quad \text{where,} \\ J(p_e) &= A_1 \left(\frac{p_e}{p_{e,\text{cut}}}\right)^{A_2}, \\ \delta_{e,\text{cool}} &= 4.5 - A_2, \quad \text{and} \\ \tilde{G}_2 &= \frac{G_2}{A_3}. \end{aligned} \quad (\text{B16})$$

We note that the factor 4.5 in $\delta_{e,\text{cool}}$ follows from

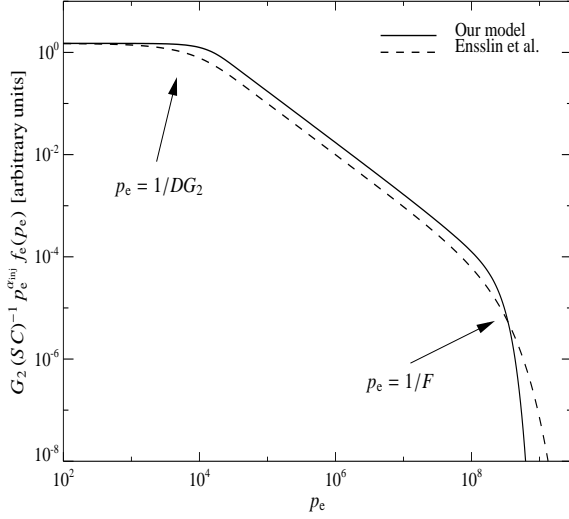


Figure B1. Comparison of the spectrum of primary electrons. We compare the electron spectrum in our model (equation B13) using results from Zirakashvili & Aharonian (2007) of the high-energy cutoff region to a spectrum from Enßlin et al. (1998) where an energy independent diffusion has been assumed. There is a break in the spectrum at $p_e = 1/DG_2$ and a cutoff at $p_e = 1/F$. The comparison shows similar spectral shape up to the cutoff region where the energy dependent Bohm diffusion in our model induces a much steeper cutoff. The offset of the two spectra between the break and cutoff regimes is caused by the integrated pile-up regime indicated by $J(p_e)$ (equation B9) that effectively shifts the break by a factor of two to higher energies.

Zirakashvili & Aharonian (2007) and represents the spectral flattening of the power-law in the low-energy regime up to the regime where the exponential cutoff dominates.

B3 Inverse Compton radiation

Inverse Compton scattering of CMB photons off ultra-relativistic electrons with Lorentz factors of $\gamma_e > 10^4$ redistributes these photons into the hard X-ray/ γ -ray regime according to equation (6). The integrated IC source density λ_{IC} for an isotropic power-law distribution of CR electrons, as described by equation (B3), is obtained by integrating the IC source function $s_\gamma(E_\gamma)$ in equation (43) of Pfrommer & Enßlin (2004) (in the case of Thomson scattering) over an energy interval between observed photon energies E_1 and E_2 yielding

$$\lambda_{IC}(E_1, E_2) = \int_{E_1}^{E_2} dE_{IC} s_{IC}(E_{IC}) \quad (\text{B17})$$

$$= \tilde{\lambda}_0 f_{IC}(\alpha_e) \left[\left(\frac{E_{IC}}{kT_{CMB}} \right)^{-\alpha_e} \right]_{E_2}^{E_1}, \quad (\text{B18})$$

$$f_{IC}(\alpha_e) = \frac{2\alpha_e^3 (\alpha_e^2 + 4\alpha_e + 11)}{(\alpha_e + 3)^2 (\alpha_e + 5) (\alpha_e + 1)} \times \Gamma\left(\frac{\alpha_e + 5}{2}\right) \zeta\left(\frac{\alpha_e + 5}{2}\right), \quad (\text{B19})$$

$$\text{and } \tilde{\lambda}_0 = \frac{16\pi^2 r_e^2 C_e (kT_{CMB})^3}{(\alpha_e - 1) h^3 c^2}, \quad (\text{B20})$$

where $\alpha_\gamma = (\alpha_e - 1)/2$ denotes the photon spectral index, $r_e = e^2/(m_e c^2)$ the classical electron radius, and $\zeta(a)$ the Riemann ζ -

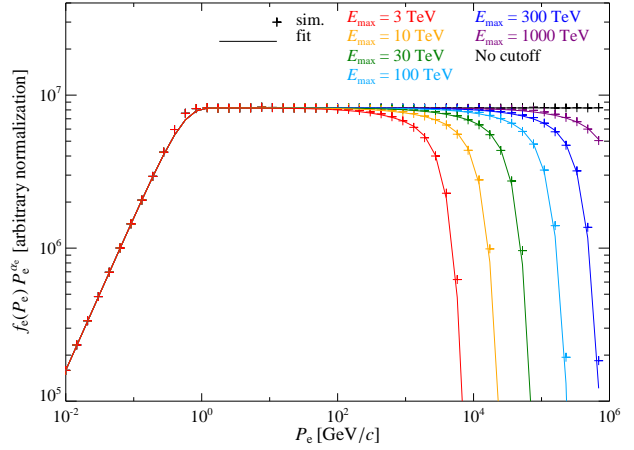


Figure B2. Cooled electron distribution of primary electrons for different cutoff energies. We show the electron distribution for a fixed spectral index $\alpha_e = 3.1$ and varying electron cutoff energies E_{\max} in raising order; 3 TeV (red), 10 TeV (yellow), 30 TeV (green), 100 TeV (light blue), 300 TeV (blue), 1000 TeV (purple), and no cutoff (black). The data (crosses) is generated by numerically integrating equation (B13) for different cutoff energies. The fit (solid lines) are derived using three free parameters, where the fitted variables are shown in equation (B16).

function (Abramowitz & Stegun 1965). The CRE normalization C_e is given by equation (B2) and (B4) for the secondary and primary electrons, respectively.

In the following, we provide a simple analytic formula that captures the primary inverse-Compton emission from galaxy clusters for strong shocks and intermediate strength shocks (i.e. $\alpha_{inj} \approx 2 - 2.7$) with an accuracy of five percent or better. In addition, we want the analytic formula to be valid in the full energy range of pIC emission, i.e. not limited by the Klein-Nishina (KN) suppression where the center of mass energy of photons becomes comparable to the electron mass and the less efficient energy transfer from electron to photon causes a break in the photon spectrum.

Using the exact spectra in the asymptotic low- and high-energy regime, together with the result of numerical calculations at intermediate energies, we parametrize the integrated source function for pIC emission by,

$$\lambda_{pIC} = \tilde{\lambda}_0(\zeta_{e,\max}, C_e) f_{IC}(\alpha_e) f_{KN}(E_{IC}, \alpha_e) \left(\frac{E_{IC}}{kT_{CMB}} \right)^{-\frac{\alpha_e-1}{2}} \times \left(1 + 0.84 \sqrt{\frac{E_{IC}}{E_{IC,cut}}} \right)^{\delta_{IC}(E_{IC}, \alpha_e)} \exp\left(-\sqrt{\frac{4.07 E_{IC}}{E_{IC,cut}}}\right), \quad (\text{B21})$$

where Bohm diffusion has been assumed. The normalization constants $\tilde{\lambda}_0(\zeta_{e,\max}, C_e)$ and $f_{IC}(\alpha_e)$ are derived in equations (B20) and (B19), respectively. The shape of the IC spectrum without an exponential cutoff scales as $E_{IC}^{-\alpha_e}$ in the Thomson regime, and steepens to $E_{IC}^{-\alpha_e} \log(E_{IC})$ in the KN suppressed high-energy regime (Blumenthal & Gould 1970). In Fig. B3 we fit the numerically calculated intermediate energy regime using the following parametrization,

$$f_{KN}(E_{IC}, \alpha_e) = \left\{ 1 + \left\{ \frac{E_{IC}}{E_{KN,1}} \left[A_{KN} \log\left(\frac{E_{IC}}{E_{KN,2}}\right) + 1 \right]^{\frac{1}{\alpha_{KN}}} \right\}^{\beta_{KN}} \right\}^{\frac{\alpha_{KN}}{\beta_{KN}}}$$

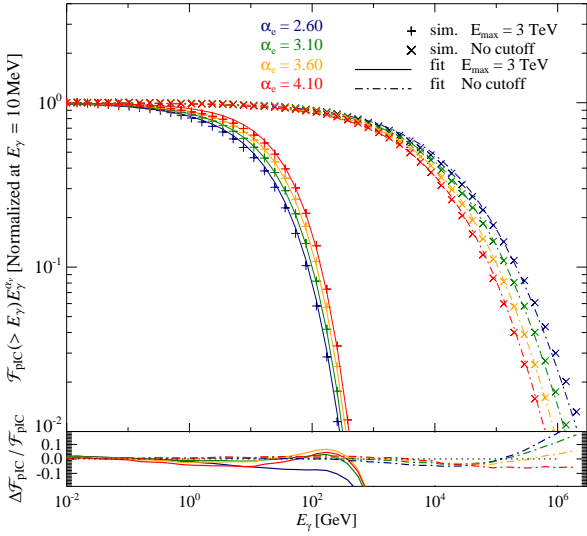


Figure B3. The primary inverse Compton γ -ray number flux weighted by photon energy for different electron spectral indices and electron cutoff energies. *Main panel:* The data is numerically calculated using a cutoff energy $E_{\text{max}} = 3$ TeV (crosses) and without a cutoff (X) for different electron spectral indices; $\alpha_e = 2.6$ (blue), $\alpha_e = 3.1$ (green), $\alpha_e = 3.6$ (yellow), and $\alpha_e = 4.1$ (red). The fits to the data using $E_{\text{max}} = 3$ TeV (no cutoff) are represented by the solid (dash-dotted) lines. *Bottom panel:* The difference between the data and the fits. The flux from the fits using the dominating electron spectral indices $\alpha_e = 3.1$ and $\alpha_e = 3.6$, agree within a few percent with the data in the dominating flux regime. The flux from the fits using electron spectral indices of $\alpha_e = 2.6$ and $\alpha_e = 4.1$ have slightly lower precision, and agree within 10 percent with the data in the dominating flux regime.

(B22)

which respects this asymptotic behavior of the IC spectrum. We use three free independent fit variables, $E_{\text{KN},1}$, β_{KN} , and A_{KN} and find that

$$\begin{aligned}
 E_{\text{KN},1} &= 2 \times 10^5 \text{ GeV}, \\
 E_{\text{KN},2} &= \frac{\text{GeV}^2}{E_{\text{KN},1}} = 5 \times 10^{-6} \text{ GeV}, \\
 A_{\text{KN}} &= 0.1 \alpha_v = 0.025 \alpha_e - 0.025, \\
 \alpha_{\text{KN}} &= -\alpha_e + \alpha_v = -\frac{\alpha_e + 1}{2}, \\
 \beta_{\text{KN}} &= 0.452.
 \end{aligned}
 \tag{B23}$$

The resulting spectra accurately describe the pIC emission without an exponential cutoff for $\alpha_e \sim 2.5 - 4.5$. In addition, we capture the shape of the integrated source function for pIC in equation (B21), where we include the super-exponential cutoff. We find that the shape of the transition region is well approximated by

$$\delta_{\text{IC}}(E_{\text{IC}}, \alpha_e) = 0.529 \alpha_e - 0.134 \log_{10} \left(\frac{E_{\text{IC,cut}}}{30 \text{ GeV}} \right),
 \tag{B24}$$

which depends on both the photon energy and the electron spectral index. In the process of finding a good fit, we allowed for multiple free parameters in equation (B21). In the end, however, we only allowed δ_{IC} to vary and fixed all the other free parameters at typical values to keep the formula as simple as possible.

In Fig. B4 we test our analytic formula for pIC emission, given by equations (B19), (B20) and (B21-B24), to the numerically calculated pIC for different electron cutoff energies. We find that the

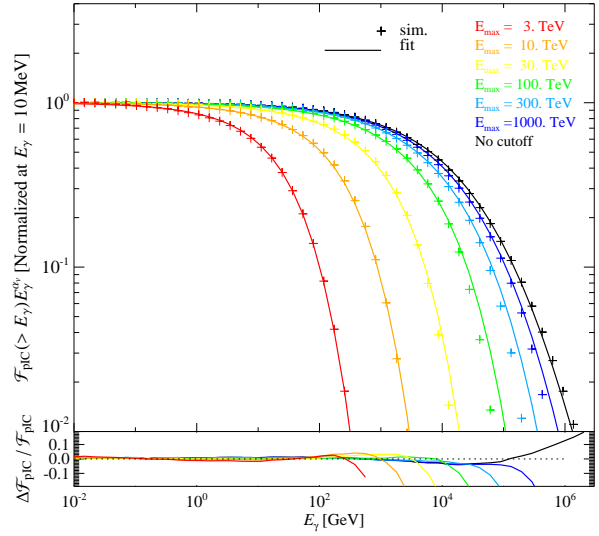


Figure B4. The primary inverse Compton γ -ray number flux weighted by photon energy for different electron cutoff energies. *Main panel:* The pIC emission are shown for a fixed electron spectral index ($\alpha_e = 3.1$) and varying electron cutoff energies (E_{max}) in raising order; 3 TeV (red), 10 TeV (orange), 30 TeV (yellow), 100 TeV (green), 300 TeV (light blue), 1000 TeV (blue), and no cutoff (black). The numerically calculated data is represented by crosses and the fits are shown with solid lines. *Bottom panel:* The difference between the data and the fits. The flux from the fits agree within a few percent with the data in the dominating flux regime.

fits agree within a few percent with the numerically calculated IC emission in the dominating flux regime where the flux is larger than 10 percent of the maximum pIC flux (that have been normalized with $E_\gamma^{\alpha_e}$).

This paper has been typeset from a \TeX file prepared by the author.